行政院國家科學委員會補助專題研究計畫成果報告

※※※※※※※※※※※※※※※※※※※※※※※※※
※ 利用電子密度拓樸學以及X光吸收光譜探討化學鍵 ※
※ 之特性 ※
※※※※※※※※※※※※※※※※※※※※※※※※※

計畫類別：☑個別型計畫　□整合型計畫

計畫編號：NSC 87－2613－M－002－002－
NSC 88－2113－M－002－033－
NSC 89－2113－M－002－031－

執行期間：86 年 8 月 1 日至 89 年 7 月 31 日

計畫主持人：王　瑜　教授

本成果報告包括以下應繳交之附件：

□赴國外出差或研習心得報告一份
□赴大陸地區出差或研習心得報告一份
□出席國際學術會議心得報告及發表之論文各一份
□國際合作研究計畫國外研究報告書一份

執行單位：國立台灣大學化學系

中 華 民 國 九十年 二月 二十六日

這是三年特約計畫的成果報告

對總電子密度作拓蹼分析來研究化學鍵的特性，在我們所附的幾篇期刊論文描述得很清楚：

（1）(J. Phy. Chem. A101, 8887-8901, 1997)的論文中，針對四種鉻-費雪碳烯化合物, $Cr(CO)_5(XR')R$,之鉻-碳及碳-氧，碳-氮鍵均以實驗和理論詳細的探討

（2）(J. Phy. Chem. A102, 3726-3731, 1998)的論文中對一鎳錯合物 $Ni(C_4N_4H_2)_2$ 的電子密度以拓樸分析來詳細探討，其中包括拓蹼分析，電子密度場梯度，原子區間，費米洞分佈及分子靜電位勢等。

（3）(J. Phy. Chem. A103, 156-165, 1999)的論文中對一系列 3d 過渡金屬方形酸錯合物,$[M^{II}(C_4O_4)(H_2O)_4]$, (M=Fe, Co, Ni, Zn), 來研究，配位子內以及和過渡金屬的鍵結皆清楚的描述，區別。而 3d 過渡金屬電子密度分佈的趨勢也可見到。

（4）(J. Chin. Chem. Soc. 46, 487-493, 1999)的論文中對一鉻錯合物 Cr(IV)(O)(TMP)來研究，各個化學鍵結可由變形電子密度和自然鍵節軌域分析來清楚的描述。其中鉻氧鍵結由分析中可得知為一三鍵鍵結，乃是由一個 σ 鍵兩個 π 鍵所構成。

（5）(J. Am. Chem. Soc. 122, 5742-5747, 2000)的論文中對自旋交叉錯合物 $Fe(phen)_2(NCS)_2$ ，以新竹 SRRC 同步輻射 X 光吸收光譜來研究其光激發自旋激態滯留狀態，由此研究中可知 K-edge，L-edge X 光吸收光譜對研究瞭解此種自旋交叉錯合物的激發態及緩解現象非常有用。

事實上，(2)，(3) 的論文中的一些圖已被引用到一些書及回顧文章中。

Abstract

This is the report of a three-year project. Bond characterization based on the topological analysis on total electron density is illustrated fully on the attached papers:

(1) (J. Phy. Chem. A101, 8887-8901, 1997) where four Cr-Fischer carbene complexes, $Cr(CO)_5(XR')R$, are studied. Metal-carbene carbon bond and the carbene carbon-X (X=O or N) bond are investigated in detail both by experiment and by theory.

(2) (J. Phy. Chem. A102, 3726-3731, 1998) where a complete topological analysis of electron density of $Ni(C_4N_4H_2)_2$ is investigated. Bond characterization is made in terms of Laplacian, field gradient, atom domain, Fermi hole distribution, as well as the molecular electrostatic potential.

(3) (J. Phy. Chem. A103, 156-165, 1999) where a series of metal squarate complexes is studied, $[M^{II}(C_4O_4)(H_2O)_4]$, (M=Fe, Co, Ni, Zn). The characterization of intra-ligand and the region around the 3d-transition metal nucleus are clearly described. The trend in these 3d-series is specified.

(4) (J. Chin. Chem. Soc. 46, 487-493, 1999) where the Cr(IV)(O)(TMP) complex is studied. The deformation density and the NBO analysis of all the chemical bonds are described. The Cr-Ooxo bond is identified as a triple bond with one σ and two π bonds.

(5) (J. Am. Chem. Soc. 122, 5742-5747, 2000) where the light induced excited spin state trapping of $Fe(phen)_2(NCS)_2$ is investigated by X-ray absorption spectroscopy using

synchrotron radiation source at SRRC. This work proves that the K- and L-edge absorption are very useful tool to understand the excitation and relaxation of the spin transition.

As a matter of fact, some figures in (2) and (3) are quoted in the book and review articles.

Key words: Bond characterization, topological analysis, X-ray absorption spectroscopy, spin transition.

Bond Characterization of Chromium–Fischer Carbene Complexes: A Combined Study of Experiment and Theory

Chih-Chieh Wang, Yu Wang, Hui-Jean Liu, Kuan-Jiuh Lin, Liang-Kuei Chou, and Kin-Shing Chan

Department of Chemistry, National Taiwan University, Taipei, Taiwan, ROC

The Journal of Physical Chemistry A®

Reprinted from
Volume 101, Number 47, Pages 8887–8901

Bond Characterization of Chromium−Fischer Carbene Complexes: A Combined Study of Experiment and Theory

Chih-Chieh Wang, Yu Wang,* Hui-Jean Liu, Kuan-Jiuh Lin, Liang-Kuei Chou, and Kin-Shing Chan†

Department of Chemistry, National Taiwan University, Taipei, Taiwan, ROC

Received: June 5, 1997; In Final Form: September 3, 1997®

Four pentacarbonyl chromium−carbene complexes, $(CO)_5CrC(XR')R$, have been studied via X-ray diffraction and molecular orbital calculations. One of the carbene complexes ($XR' = OCH_3$, R = −(C≡CPh)) has been investigated extensively at 110 K by X-ray diffraction using Mo Kα radiation. The electron density distribution of this compound as well as the asphericity in electron density around the Cr atom is clearly demonstrated by deformation density and the Laplacian of electron density. The comparison between experiment and theory is made in terms of deformation density, topological properties, and d orbital populations of Cr. Further chemical bond characterization is based on quantum mechanical molecular orbital calculation and properties associated with bond critical points. The π bond character of a metal carbene can be best represented by a Cr−C−X three-centered four-electron bond with the π electron density mainly located at either the d_{yz} orbital of Cr or the p_z orbital of X in the carbene ligand. This makes the carbene carbon an electrophilic site in the p_π direction. The resemblances and differences between amino−(X=N) and alkoxy−(X=O) carbene complexes are of special interest. Because the energy of π^*_{C-N} orbital is fairly close to that of the $\pi^*_{C=O}$ (carbonyl on Cr), the π bond character is delocalized toward the $M-C_{carbonyl}$ at the trans position i.e., O=C=M−C=N in the amino carbene case; this is in accord with the shortening of bond lengths of the trans $M-C_{carbonyl}$ for many amino−carbene complexes. The π bond-delocalization is also illustrated by the Fermi hole distribution. The bond dissociation energies of these carbene complexes are calculated at the CASSCF level and with the density functional method (DFT). The relative orbital energies are also compared with photoelectron spectroscopy (PES) data. The values based on DFT using the transition-state approximation give the best agreement with the experimental results.

Introduction

Transition metal carbene complexes have been extensively studied primarily due to their importance in catalysis and their use in organic synthesis[1−4]. Generally, metal carbene complexes are typically divided into two types: the Fischer[3] and the Schrock[4]-type complexes. The Fischer carbene complex is electrophilic at the carbene carbon, and the Schrock type complex is nucleophilic at the carbene carbon. It is well-known that the metal ion is normally in its low oxidation state in Fischer-type carbene complexes, and such a carbene is often stabilized by a heteroatom X, where X = N, O, and S. On the contrary, the metal ion is often in its high oxidation state in Schrock-type carbenes. For Fischer-type carbenes, the nature of the metal−carbene bond and of the C−X bond in the carbene fragment of the ligand, :C(XR')R, are of special interest. Because of the lone-pair electrons at the heteroatom X, the possible π bond delocalization between $M-C_{carbene}$ and $X-C_{carbene}$ could be formulated as a hybrid of resonance structures shown in **a**−**c**.

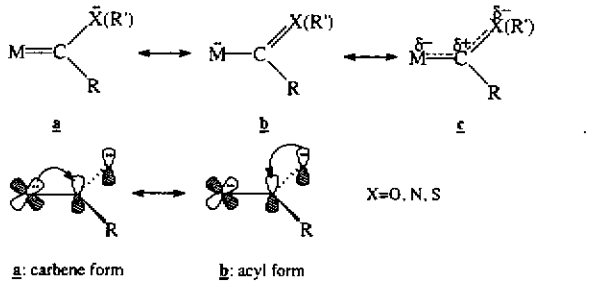

Earlier empirical MO calculations were reported[5] on several pentacarbonyl chromium−carbene complexes $(CO)_5Cr{=}CXR'R$ ($XR' = OMe$, NH_2, NMe_2, and SMe) in comparison with the photoelectron spectroscopy (PES) studies.[5] These studies[5] indicated that amino−carbenes are poorer π acceptors than alkoxy- or alkyl-thio carbenes, and all these carbene ligands are poorer π acceptors than carbonyl ligands. However, the same study gave a different view on the generally accepted idea of the carbene carbon being an electron deficient center. The first nonempirical calculation on a model transition metal carbene complex was introduced by Schaefer and co-workers;[6] the system chosen was $(CO)_3NiCH_2$. The result indicated that the barrier on the rotation about the $Ni-C_{methylene}$ axis is very small. Nakatsuji and co-workers[7] later did ab initio calculations

* To whom all correspondence should be addressed.
†Present address: Department of Chemistry, Chinese University of Hong Kong, Shatin, NT, Hong Kong.
® Abstract published in *Advance ACS Abstracts*, November 1, 1997.

S1089-5639(97)01848-3 CCC: $14.00

TABLE 1: Crystal Data for Compounds 1, 2, 3, and 4

	compound 1	
formula	$(CO)_5CrC(OMe)(-C{\equiv}CPh)$	
formular weight	336.22	
crystal system	monoclinic	
T (K)	120	300
space group	$P2_1/n$	
a, Å	11.382(1)	11.632(2)
b, Å	11.506(1)	11.563(6)
c, Å	11.739(1)	11.964(4)
α, deg		
β, deg	108.377(9)	107.91(2)
γ, deg		
Z	4	4
$R_{int}(\Sigma(I_i - \langle I \rangle)/\Sigma I, \%)$	1.9	
R_1, R_{1w}[a]	0.028, 0.039	0.036, 0.037
R_1, R_{1w}[a](sin $\theta/\lambda \geq 0.65$)	0.024, 0.024	
goodness of fit, S[b]	3.73	1.67

	compound		
	2	**3**	**4**
formula	$(CO)_5CrC(NH_2)Me$	$(CO)_5CrC(NH_2)Ph$	$(CO)_5CrC(NMe_2)Ph$
formular weight	235.31	297.18	325.24
crystal system	monoclinic	monoclinic	triclinic
T (K)	300	300	300
space group	$P2/c$	$C2/c$	$P\bar{1}$
a, Å	23.449(5)	29.163(7)	6.714(7)
b, Å	8.796(2)	7.740(5)	14.814(7)
c, Å	12.058(3)	11.502(4)	16.022(9)
α, deg			107.39(4)
β, deg	90.95(2)	94.71(2)	94.32(6)
γ, deg			90.11(6)
Z	10	8	4
$R_{int}(\Sigma(I_i - \langle I \rangle)/\Sigma I, \%)$			
R_1, R_{1w}[a]	0.039, 0.029	0.049, 0.045	0.049, 0.053
goodness of fit, S[b]	1.87	3.71	2.04

[a] $R_1 = [\Sigma|F_o - F_c|/F_o]$; $R_{1w} = [(\Sigma w|F_o - F_c|^2)/(\Sigma w|F_o|^2)]^{1/2}$. [b] $S = [(\Sigma w|F_o - F_c|^2)/(N_{obs.} - N_{var.})]^{1/2}$. $N_{obs.}$: No. of observed reflections. $N_{var.}$: No. of variables.

at the HFSCF level on two Fischer-type carbenes: $(CO)_5Cr{=}CH(OH)$ and $(CO)_4Fe{=}CH(OH)$. The bond energies of $M-C_{carbene}$ were calculated to be 44.4 and 36.8 kcal/mol for Cr and Fe respectively. The rotational barrier around the $M-C_{carbene}$ bond was calculated again to be very small. The electrophilic reactivity of the carbene carbon is interpreted not by the charge-controlled but by the orbital-controlled mechanism[7]. Other MO calculations using extended Hückel[8,9], Fenske–Hall,[10–13] and HFSCF[14–18] all gave similar conclusions about the geometry and the bond description on the metal carbene bond. The first post-HF calculation on such a metal carbene system was reported by Taylor and Hall,[19] where a limited CI expansion (12 configurations) was performed on a Fischer-type $(CO)_5Mo{=}CH(OH)$ and a Schrock-type $CpCl_2Nb{=}CH_2$ metal carbene. The results indicated that the former (Fischer-type) M–C bond is bound datively between two singlet fragments (depicted as **d**), whereas the latter (Schrock-type) is bound covalently between two triplet fragments (depicted as **e**).

M⇀↽C M=C

d e

Since the work of Taylor and Hall,[19] the post-Hartree–Fock calculations,[19–23] such as CASSCF[24–26] (complete active space self-consistent field) and/or FORS[27,28] (full optimized reaction space) methods, were undertaken to understand the bonding character of the metal carbene[21–23] and the metal carbyne[29] complexes. Accurate geometrical parameters, bond dissociation energies, and the rotational barrier of the carbene fragment around the M–C bond were given in these calculations.[20,21] The importance of the electronic correlation was discussed.[21] Recently, density functional calculations (DFT)[30] have been recognized to be a powerful computational tool in predicting the geometries and energies of transition metal complexes.[31] Ziegler and co-workers[32] have investigated extensively the transition metal Fischer-type complexes using the DFT approach. The relative bond energies and especially π bond analysis of chromium–carbene, –silyene, and higher homologues were discussed[32] in detail. Similar comparisons were made on the carbene complexes with transition metals of chromium triad.[32] The nonlocal correction and the relativistic effects were both important for understanding the trend in bond strength, particularly the intrinsic π bond strength.[32]

To characterize the nature of the Fischer-type transition metal–carbene bond, we have undertaken studies of structures, of deformation density, of the topology of the electron densities, and of the electronic structures of four pentacarbonyl chromium–carbene complexes: $(CO)_5CrC(OCH_3)(-C{\equiv}CPh)$, (**1**), $(CO)_5CrC(NH_2)Me$, (**2**), $(CO)_5CrC(NH_2)Ph$, (**3**), $(CO)_5CrC(NMe_2)Ph$, (**4**). The molecular and crystal structures of all four complexes are determined by X-ray diffraction at room temperature. The methoxy–carbene complex (**1**) is further investigated by X-ray diffraction at low temperature (110 K) in order to obtain the detailed electron density distribution experimentally. Parallel electron density distributions can be easily derived from the corresponding molecular orbital calculations. A direct comparison between the experiment and theory may shed some light on the bond characterization of this interesting system. For the

purpose of understanding the role of the heteroatom in this type of complexes, amino carbenes are investigated as well. Unfortunately no suitable crystal of amino carbenes is available for detailed electron density study. The density distribution, bond dissociation energy, and bond characterization were made on compound **2** and simplified compound **1**, $(CO)_5CrC(OH)(-C{\equiv}CH)$. Bond characterization is analyzed through the natural bond orbital (NBO) at the HFSCF and CASSCF levels. The intrinsic π bond will be discussed using the orbital correlation diagram and the Fermi hole distribution. In addition, the "atom in molecules" concept[33] has been proven to be a feasible approach in describing chemical bonds,[34] nonbonded interactions,[35] and molecular[36] and crystal structures.[37] Therefore, bond characterization will also be presented in terms of the topological properties of the total electron density both experimentally and theoretically. Vertical ionization potentials (VIPs) are calculated with both ab initio HFSCF and DFT methods on five chromium carbenes: **2**, **3**, **4**, $(CO)_5CrC(OMe)Ph$ (**5**), and $(CO)_5CrC(NMe_2)(CH_3)$ (**6**). A comparison between the calculated values and the experimental PES data will be made. The theme of this work is to try to make a comparative study both on density distribution and on orbital energies.

Experimental Section

Data Collection and Refinement: Chromium Carbene Complexes. Compounds **1**, **2**, **3**, and **4** were synthesized according to the literature procedures.[38] Dark red **1** and pale yellow crystals **2**, **3** and **4** were obtained by using the sublimation method under vacuum. Intensities of three standard reflections of each compound were monitored every hour throughout the measurement, and no significant variation in intensity was detected in any case. Scattering factors for neutral atoms, corrected for anomalous dispersion, were taken from *International Table for X-ray Crystallography*, Vol. IV.[39] Structures were solved by Patterson and direct methods and subsequently refined by a full matrix least-squares procedure using anisotropic thermal parameters for all non-hydrogen atoms. Relevant crystal data are listed in Table 1; details are in deposit.

Low-temperature (110 K) data were collected on **1** using a liquid N_2 gas-flow device. Intensity data were measured up to a 2θ of 70° for a full Ewald sphere, and 40 additional high-angle reflections with 2θ's of 70−85.6°, which were predicted to be strong, were measured. In addition, intensities of $(\pm h, +k, +l)$ at four ψ angles (−30°, −10°, 10°, 30°) were collected for each reflection up to a 2θ of 70°. This yielded a total of 35 609 measurements, which gave 6463 unique reflections after averaging of all equivalents. An absorption correction was applied (before averaging) according to six measured faces; the correctness of the face measurements was checked against the experimental ψ curves on three reflections. The interset agreement in intensities is 1.9%. The counting statistic weight was applied, and the σ of the averaged intensity was taken as a geometric mean of all the σ's of equivalents. To obtain all the non-H atom parameters of **1** for a promolecular density calculation (see below), additional high-order refinements were carried out with a $\sin\theta/\lambda$ data range from 0.65, 0.70, and 0.75 $Å^{-1}$ with 2441, 1767, and 1008 reflections, respectively. The parameters from the refinement with $\sin\theta/\lambda \geq 0.65$ data were finally chosen for the promolecular density calculation based on the R values and relevant error assessments. The hydrogen positions were displaced along the C−H vector to make a C−H distance of 1.08 Å. A multipole model refinement[40] was

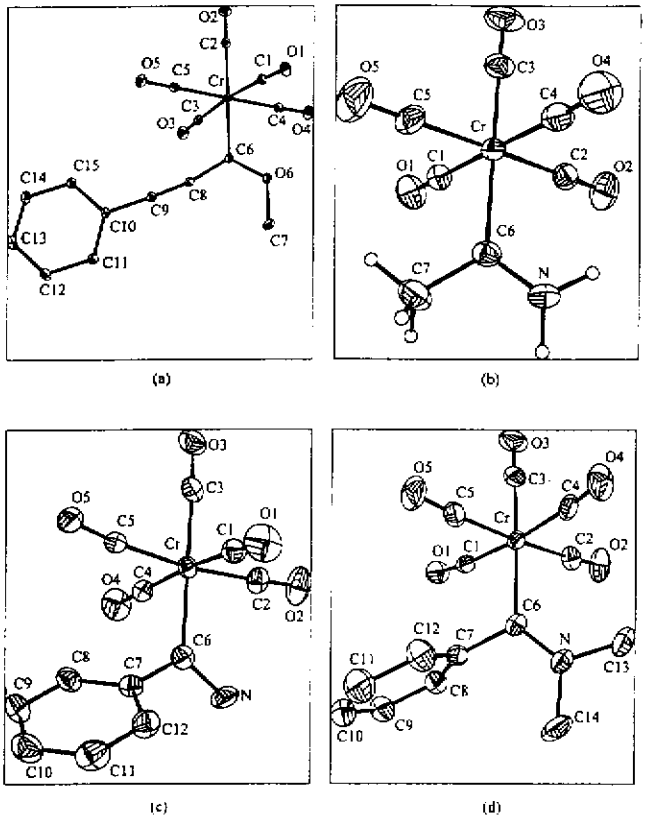

Figure 1. Molecular structure and thermal ellipsoids of compound (a) **1** at 110 K, (b) **2**, (c) **3**, (d) **4** at 300 K.

performed according to the equation.

$$\rho_{\text{atomic}}(r) = \rho_{\text{core}} + P_v\kappa^3\rho_{\text{valence}}(\kappa r) + \sum_{l=0}^{l} R_l(r) \times \sum_{m=0,p=\pm}^{l} P_{lmp} Y_{lmp}$$

where

$$R_l(r) = \frac{\xi_l^{n_l+3}}{(n_l+2)!} r^{n_l} \exp(-\xi_l r)$$

The first two terms of this equation are the spherical part of atomic electron density; the third term is the sum of multipole terms which are expressed as spherical harmonic functions (Y_{lmp}); $R_l(r)$ is the radial function; κ is the expansion−contraction factor of the radial distribution. The K core is considered for the Cr atom; the He core is taken for C, N, and O atoms. The valence configurations of Cr, C, N, and O atoms are d^5, s^2p^2, s^2p^3, s^2p^4, respectively. Multipole expansions of the valence shell up to hexadecapoles for the Cr atom, up to octapoles for C, N, O atoms, and up to dipoles for H atoms are included in the refinement. Multipole coefficients, P_{lmp}, for H atoms at methyl and phenyl groups were constrained to be the same in each group; the multipole coefficients of C and O atoms of the four carbonyl groups on the equatorial plane were also constrained to be the same. The coefficients of the multipole terms together with positional and anisotropic thermal parameters were obtained by a full-matrix least-squares refinement based on F_o. Atomic sacttering factors of both core and valence electrons were taken from *International Tables for X-ray Crystallography*, Vol. IV.[39] Atomic parameters of compounds **1**, **2**, **3**, and **4** are in deposit.

TABLE 2: Agreement Indices of the Multipole Refinements on 1[a]

	variable	R_1	R_{1w}	R_2	R_{2w}	S
conventional	255	0.025	0.042	0.028	0.043	4.81
monopole	323	0.025	0.038	0.025	0.038	4.21
octapole[b]	334	0.021	0.028	0.015	0.027	2.77
hexadecapole	553	0.021	0.027	0.015	0.027	2.71

[a] $R_2 = \sum||F_o^2 - F_c^2||/\sum F_o^2$. $R_{2w} = (\sum w|F_o^2 - F_c^2|^2/w\sum F_o^4)^{1/2}$. [b] Only the Cr atom is up to hexadecapole.

Deformation Density. The deformation density ($\Delta\rho$) is defined as the difference between the molecular density and the promolecular density. The promolecular density is composed of the sum of the densities from the superposition of the free spherical atoms, each centered at its equilibrium position in the molecule. The X−X deformation density ($\Delta\rho_{X-X}$) is calculated as the difference between the observed density, ρ_{obs}, and the superposition of the sum of spherically averaged free atomic densities; that is, the Fourier coefficients were taken to be the difference between kF_o and F_c, where F_c is calculated from the parameters obtained from high-order refinement (sin $\theta/\lambda \geq 0.65$ Å^{-1}) and k is the optimum scale factor. Deformation density maps ($\Delta\rho_{X-X}$) were calculated up to a resolution of sin $\theta/\lambda \geq 0.96$ Å^{-1}. The model deformation density distributions ($\Delta\rho_{M-A}$) were generated by subtracting the spherical atomic electron density from the sum of the atomic electron densities evaluated from a multipole model.[40] The coefficients (P_v, P_{lmp}) of the multipole terms are obtained from a least-squares fit of the X-ray diffraction data using the MOLLY program.[40a,b] The static multipole deformation densities ($\Delta\rho_{M-A,static}$) were calculated in direct space according to the equation given above.[40c] The residual density, $\Delta\rho_{res}$, is defined as the difference between the observed and the multipole model ones.

Topology of Electron Density. The total electron density distribution, $\rho(r)$, is calculated using the multipole model. The gradient vector field, $\nabla\rho(r)$, and Laplacian, $\nabla^2\rho(r)$, are derived according to the logarithms given by Bader.[33] Bond critical points (r_c) are located at each chemical bond, where associated properties,[33] such as the density, $\rho(r_c)$, and the Laplacian, $\nabla^2\rho(r_c)$, values at the bond critical point, bond ellipticity, ϵ, etc., are used to characterize the bond type and bond order. Bond path and atomic domain can also be obtained.

All computations were carried out on Micro VAX and IBM Risc 6000 computers using NRCVAX,[41] MOLLY,[40a,b] SALLY,[40c] and PROP[42] programs. The contours of model deformation density were produced by a locally developed contour-plotting program.[43]

Molecular Orbital Calculations

Geometry and Basis Functions. To compare bonding between the amino- and alkoxy-chromium−Fischer carbenes,

TABLE 3: Comparisons of Selected Bond Lengths of Some Chromium−Fischer Carbene Complexes

$(CO)_5CrC(XR')R$	Cr−$C_{carbene}$	X−$C_{carbene}$	Cr−C_{cis}(av)	Cr−C_{trans}	ϕ	ref
XR′ = OMe (1) R = −(C≡CPh)	1.9990(4)	1.3233(4)	1.894	1.897	31	*a*
XR′ = OEt R = −(C≡CPh)	2.00(2)	1.32(2)				68
XR′ = OMe R = Ph	2.04(3)	1.33(2)	1.89	1.87		69
XR′ = OEt R = Me	2.053(1)	1.314(1)	1.908	1.893	45	70
XR′ = OMe R = CH(Me)(Et)	2.006	1.301	1.873	1.899	10	71
XR′ = OEt R = C(OMe)(CHOMe)	2.061	1.336	1.905	1.883	44	72
XR′ = OH R = Ph	2.052	1.316	1.908	1.866	37	73
anion:BF_4^-, XR′ = OEt R = $CH_2[NC_6H_3(CH_3)]$	2.02	1.306	1.899	1.885	39	74
cation:NMe_4^+, X = O R = C(Me)(CH_2)	2.147(5)	1.232(6)	1.884	1.838	45	75
XR′ = NH_2 (2) R = Me	2.081(4)	1.293(6)	1.884	1.856	37	*a*
XR′ = NMe_2 (3) R = Ph	2.097(7)	1.334(8)	1.889	1.835	42	*a*
XR′ = NH_2 (4) R = Ph	2.057(6)	1.313(8)	1.882	1.853	2	*a*
XR′ = NH(Me) R = Me	2.09	1.33	1.87	1.81		76
XR′ = NEt_2 R = Me	2.16(1)	1.31(1)	1.90	1.85		77
XR′ = N(C_4H_6) R = Me	2.123(2)	1.300(2)	1.89	1.86		78
XR′ = N(Me)(*i*-Pr) R = Me	2.116	1.278	1.888	1.898	43	79
XR′ = NMe(CH_2Ph) R = Me	2.135	1.309	1.892	1.858	38	80
XR′ = NC_5H_{80} R = C_5H_6	2.125	1.317	1.896	1.853	45	81
XR′ = NC(OMe)Ph R = CMe_3	2.148	1.268	1.903	1.876	9	82
XR′ = N(C_6H_{11}) R = C(CH_2)(OMe)	2.15(1)	1.32(2)	1.875	1.88(2)	47	83
Calc Cr−C(sp^2)	2.21	C=O = 1.22 C=N = 1.28				84

[a] This work.

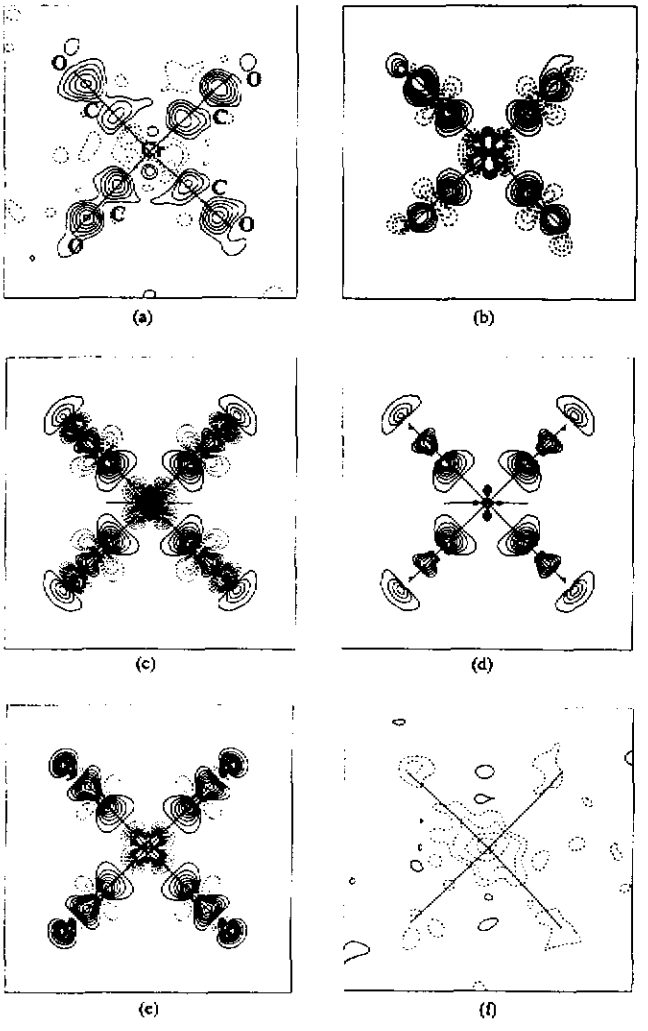

Figure 2. Deformation density distribution on the equatorial $Cr(CO)_4$ plane for compound **1**: solid line positive, dotted line negative, contour interval 0.1 e Å^{-3}, (a) $\Delta\rho_{X-X}$, (b) $\Delta\rho_{M-A}$, (c) $\Delta\rho_{HFSCF}$, (d) same as in c, but with positive contours only, (e) $\Delta\rho_{DFT}$, (f) $\Delta\rho_{residual}$.

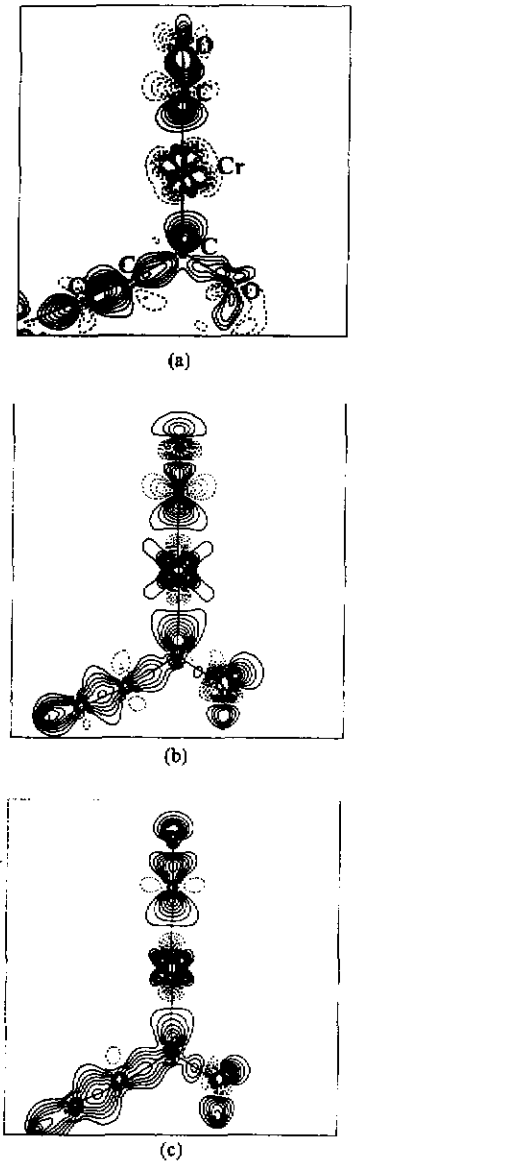

Figure 3. Deformation density distribution on the plane of Cr−C6−O6 for compound **1**: (a) $\Delta\rho_{M-A}$, (b) $\Delta\rho_{HFSCF}$, (c) $\Delta\rho_{DFT}$; contours are as in Figure 2.

compound **2** and simplified compound **1** $(CO)_5CrC(OH)(C{\equiv}CH)$ are chosen for the MO calculations. The molecular geometries are basically taken from the diffraction work and are defined to have C_s symmetry. All the $Cr-C_{carboonyl}$ distances of model compound **1** were considered to be equal, with an average bond length of 1.894 Å. The carbene plane is at the bisection of the C−Cr−C angle to ensure C_s symmetry. For compound **2**, four $Cr-C_{carbonyl,cis}$ were set to be equal at the average bond length of 1.884 Å, and the $Cr-C_{carbonyl,trans}$ bond length was taken at 1.857 Å; again the carbene plane is at the bisection of the C−Cr−C angle. The $Cr(CO)_5$ fragments of both compounds are assumed to be in C_{4v} symmetry. The internal coordinate at the Cr atom is defined in the same way for both carbenes, where the z-axis is along the $Cr-C_{carbene}$ and the xz-plane is at the mirror plane (C_s). The basis set used for the Cr atom is (14,9,6)/[8,4,3] contractions, i.e., (626*1/5112/411),[44,45] where 14s,9p primitive Gaussian functions are taken from Wachter[44] and 6d functions are taken from Goddard.[45] The basis sets used for N, O, C, and H atoms are taken from split valence level double-ζ 6-31G. The basis used in the DFT calculations is a double numerical basis set augmented by polarization functions (DNP).[46a,b] Electron correlation is treated within the local density approximation (LDA) in the parameterization of Vosko et al.[47] The bond dissociation energies are determined by adding Becke's[48] nonlocal exchange corrections as well as Perdew's[49] inhomogeneous gradient corrections for correlation (LDA/NL/BP) as a perturbation.

HFSCF and CASSCF Calculations. The CASSCF (complete active space self-consistent field)[24−26] is a limited type of multiconfiguration self-consistent field (MCSCF) calculation which provides an optimized sets of primary orbitals for configuration interaction (CI) calculations. A Hartree−Fock calculation (HFSCF) is performed on model compounds **1** and **2**, and the molecular orbitals are assigned accordingly (the A′ state configurations between two compounds are similar to $\pi_2^2\sigma^2\, d_{xz}^2\, d_{x^2-y^2}^2\, \pi_1^2$, where π_1 denotes the $Cr-C_{carbene}$ π bond, π_2 denotes the π bond of $C_{carbene}-X$; X = O, N). Six orbitals concerning the π_{C-X}, σ_{Cr-C}, π_{Cr-C}, π^*_{Cr-C}, σ^*_{Cr-C}, π^*_{C-X} orbitals of the $Cr-C_{carbene}$ double bond are chosen to be the active space, i.e., three occupied orbitals (π_1, σ, π_2) and three unoccupied orbitals (π^*_1, σ^*, π^*_2) for Cr=C region. A configuration interaction calculation within the framework of these six orbitals optimized by the CASSCF(6,6) method with 175 spin-adapted configurations is performed on both **1** and **2**. An additional CASSCF(6,6) calculation is applied to both compounds **1** and **2** with the $(CO)_5Cr$ and carbene fragments

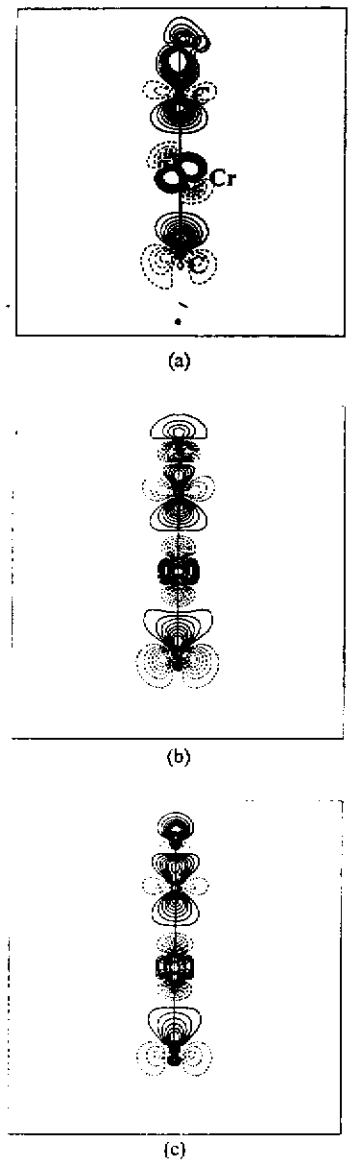

Figure 4. Deformation density distribution on the plane perpendicular to Figure 3 and through the $Cr-C_{carbene}$ bond of compound **1**: (a) $\Delta\rho_{M-A}$, (b) $\Delta\rho_{HFSCF}$, (c) $\Delta\rho_{DFT}$, contours are as in Figure 2.

separated by 6 Å in order to obtain the orbital correlation and bond dissociation energy.

Natural Bond Orbital Analysis. Natural bond orbital analysis[50-54] comprises a sequence of transformations from the given basis sets to various localized sets: natural atomic orbitals (NAOs), natural hybrid orbitals (NHOs)[51] natural bond orbitals[53] (NBOs), and natural localized molecular orbitals (NLMOs).[50,52] The given basis functions are taken from ab initio HF and CASSCF calculations. The results after NBO analysis are generally in good agreement with Lewis structure concepts and the Pauling–Slater–Coulson[55] concept of bond hybridization and polarization. Net atomic charges, orbital populations, and bond orders are thus generated by means of an NBO analysis. The charges and orbital populations obtained this way are designed as the natural orbital population analysis (NPA), which is compared with the Mulliken population analysis (MPA). In DFT calculations, a Hirshfeld partition[46c] is used for obtaining the net atomic charge.

Theoretical Deformation Density. The theoretical deformation density ($\Delta\rho_{theo}$) is defined as the difference between the total molecular density and the promolecular electron density. The total molecular density is calculated from HFSCF molecular wave functions; each occupied molecular orbital is assigned to have two electrons. The promolecular electron density is the sum of superposition of the spherical atomic density with atoms at the same nuclear positions as in the molecular geometry. The spherical atomic density is calculated at the ROHF/GVB level.[56] The total molecular electron density is used for the gradient vector field, $\nabla\rho(r)$, and the Laplacian distribution. Bond critical points are located, and the associated properties are derived. The Fermi hole function[57-59] is a measure of Pauli exculsion and is utilized here for characterizing the electron delocalization.

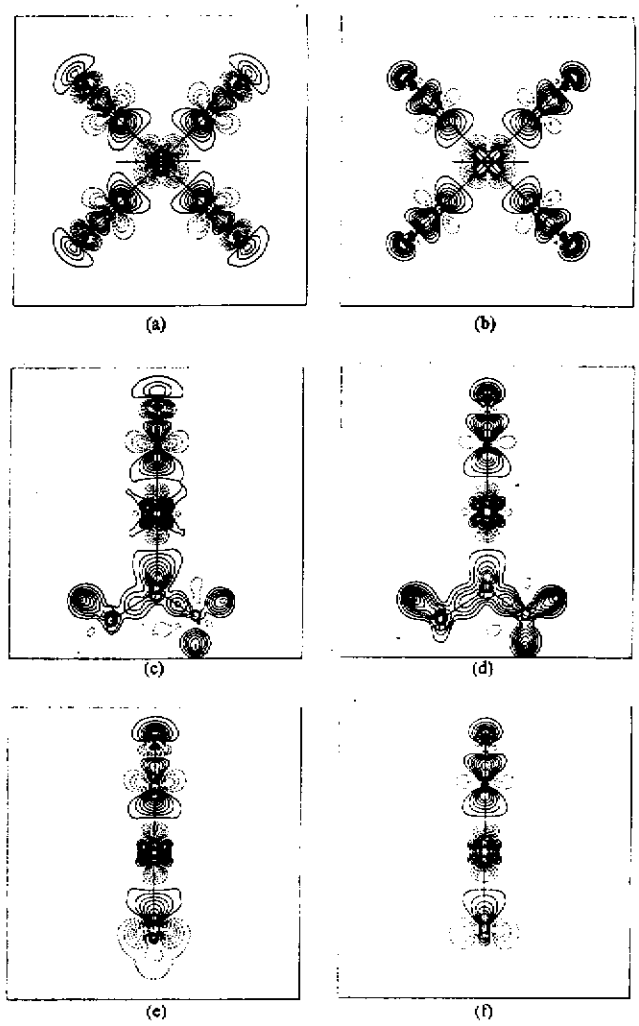

Figure 5. Deformation density distribution of compound **2** on the three planes as defined in Figure 2, Figure 3, and Figure 4 for (a, b), (c, d) and (e, f) respectively. Contours are as in Figure 2; (a, c, and e) from HFSCF calculation; (b, d, and f) from DFT calculation.

Ionization Potentials. Vertical ionization potentials (VIPs) are obtained on the basis of Koopmann's theory[60] using ab initio calculation (HFSCF). IPs from DFT are calculated on the basis of a simple approximation to Slater's transition-state concept[61] originated from Åsbrink et al.,[62] where instead of removing half of an electron from the MO of interest, we remove half of an electron evenly from the top ten valence MOs.[63]

All computations are performed on CONVEX C3840 and Power Challenge computers using the Gaussian94[64] and DMol programs.[65] The MOPLOT[66] program is used for the deformation density calculation. The AIMPAC[67] program is used for topological analysis.

Results and Discussions

Structure. The molecular structures of **1**, **2**, **3**, and **4** are depicted in Figure 1. The agreement indices at various stages

TABLE 4: d Orbital Populations of Cr Atom in (a) 1; (b) 2[a]

	HFSCF		CASSCF(6,6)			
(a)	MPA	NPA	MPA	NPA	DFT MPA	multipole
d_{xy}	0.55(9%)	0.89(13%)	0.55(10%)	0.89(13%)	0.72(13%)	0.56(14%)
d_{z^2}	0.52(9%)	0.87(13%)	0.52(9%)	0.87(13%)	0.79(15%)	0.83(21%)
d_{yz}	1.47(25%)	1.58(23%)	1.45(25%)	1.59(23%)	1.34(25%)	0.95(24%)
d_{xz}	1.72(30%)	1.81(26%)	1.71(30%)	1.80(26%)	1.20(22%)	0.61(15%)
$d_{x^2-y^2}$	1.58(27%)	1.69(25%)	1.52(26%)	1.66(25%)	1.38(25%)	1.03(26%)
total	5.84	6.84	5.75	6.81	5.43	3.98
(b)	MPA	NPA	MPA	NPA	MPA	
d_{xy}	0.55(9%)	0.90(13%)	0.55(9%)	0.88(13%)	0.72(13%)	
d_{z^2}	0.55(9%)	0.88(13%)	0.55(9%)	0.90(13%)	0.78(14%)	
d_{yz}	1.55(26%)	1.67(24%)	1.49(26%)	1.65(24%)	1.37(25%)	
d_{xz}	1.69(30%)	1.77(26%)	1.71(30%)	1.76(26%)	1.31(24%)	
$d_{x^2-y^2}$	1.54(26%)	1.65(24%)	1.52(26%)	1.65(24%)	1.28(24%)	
total	5.88	6.87	5.82	6.84	5.46	

[a] MPA: Mulliken population analysis. NPA: Natural orbital population analysis.

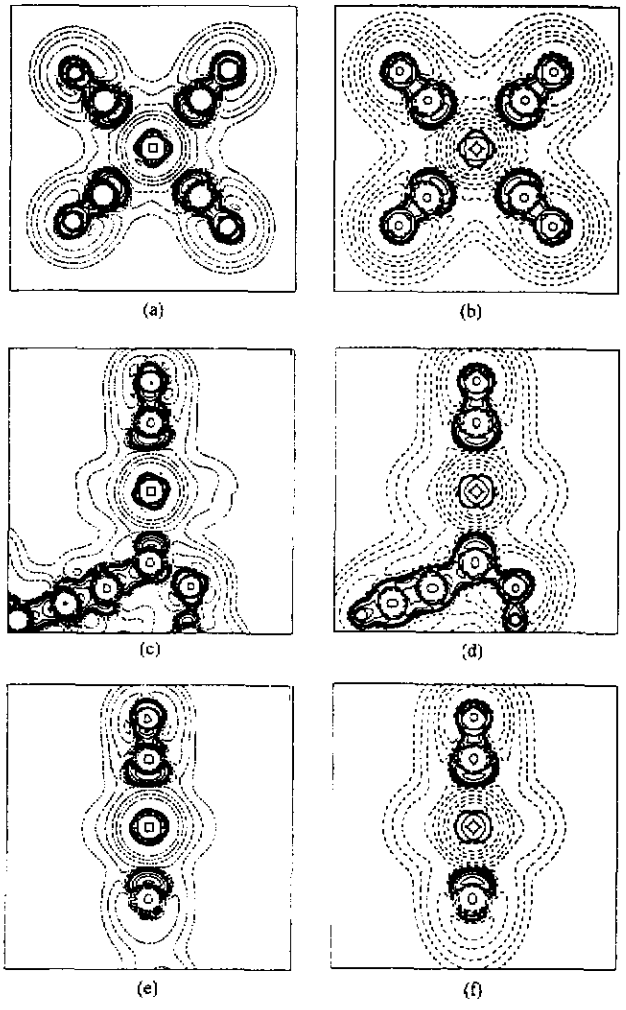

Figure 6. Negative Laplacian of electron density, $-\nabla^2\rho(r)$, of compound **1**. Solid lines are in regions where electronic charge is concentrated, and dashed lines are in regions where charge is depleted; (a, c, and e) obtained from experiment; (b, d, and f) from theory. Plane definitions are given in Figures 2, 3, and 4. Contour intervals, $\pm 2^i \times 10^j$ e Å^{-5}; $i = 1, 2, 3$ and $j = -1, 0, 1$. Box size 8 × 8 Å.

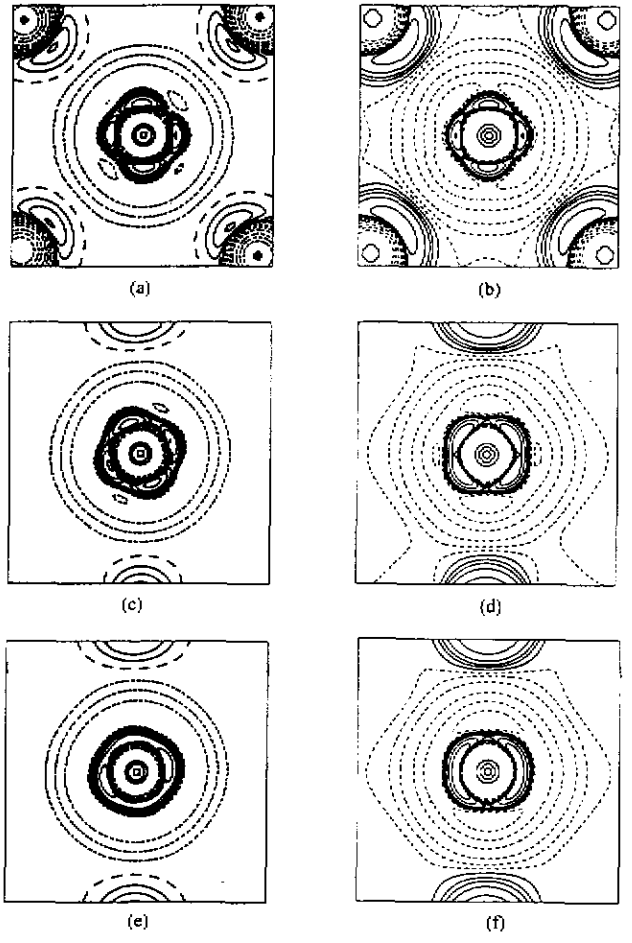

Figure 7. Negative Laplacian around Cr of **1**. Definitions of a−f are as those in Figure 6. Contour intervals, $\pm 2^i \times 10^j$ e Å^{-5}; $i = 1, 2, 3$ and $j = 0, 1, 2, 3$. Box size 3 × 3 Å.

of multipole refinement on **1** are given in Table 2. The apparent improvement is observed by going up to octapole, where only the Cr atom is modeled to hexadecapole; additional hexadecapole terms for other atoms do not improve the model significantly. It is well-known that in Fischer carbene complexes, the heteroatom (X = N, O, and S) stabilizes the carbene complex by its electron pair donation to the carbene carbon atom. The resulting partial double-bond character between the heteroatom and the carbene carbon is manifested by a shortening of the carbon−heteroatom bond, C−X. The $Cr-C_{carbene}$, $C_{carbene}-X$ bond lengths on a collection of chromium−carbene complexes with X = O, N are listed in Table 3. In general, the $Cr-C_{carbene}$ bond is significantly shorter than the predicted $Cr-C_{sp^2}$ single bond,[84] but it is ~0.1 Å longer in amino carbene (X = N) than that in alkoxy carbene (X = O). This finding is reproduced in a recent theoretical calculation.[85] The C−X bond lengths are all longer than the expected C=O and C=N double-bond lengths. One exception is the carbene anion, $[NMe_4][(CO)_5CrC(O)CMeCH_2]$,[75] where C−X (1.232 Å) is apparently a

localized double bond and the corresponding Cr−C (2.147 Å) is the longest among the alkoxy carbenes. The inverse relationships between C−X and Cr−$C_{carbene}$ bond lengths in Fischer carbene complexes are well established;[74] this evidence is consistent with the "competition" between acyl (or imino) and carbene forms. The Cr−$C_{carbonyl}$ bond in these complexes is, on the average, 1.89−1.90 Å. However, in amino carbene, such a bond at the trans position (with respect to carbene) is usually 0.03−0.05 Å shorter than those at the cis position; the corresponding carbonyl bond (C≡O) is somewhat longer (1.152 vs 1.135 Å). This indicates that the π bond character is extended to the trans Cr−$C_{carbonyl}$ bond more prominently in the case of X = N than in the case of X = O. This is also found[85] in the calculated BDE, the BDE of trans Cr−$C_{carbonyl}$ being ~15 KJ/mol higher in an amino carbene, $(CO)_5Cr(NH_2)R$, than in an alkoxy one. The coordination sphere of Cr is roughly tetragonal distorted O_h, with the plane of carbene fragment making an angle of ϕ with respect to one of the cis Cr−$C_{carbonyl}$ axes. The angle (ϕ) is mostly in the range 30−45°; however, in three cases they are less than 10° (Table 3). Therefore the commonly observed conformation is with the carbene fragment plane close to the bisection of ∠$C_{carbonyl}$−Cr−$C_{carbonyl}$, i.e., at ϕ of 45°.

Deformation Density Maps. Deformation density maps on the equatorial $Cr(CO)_4$ plane are displayed in Figure 2 in terms of $\Delta\rho_{X-X}$, $\Delta\rho_{M-A}$, $\Delta\rho_{M-A,statics}$, $\Delta\rho_{res}$, and the corresponding calculated maps generated by ab initio and DFT calculations. The features on the Cr−$C_{carbonyl}$ and C≡O regions are as expected. It clearly shows the σ donor characteristics of the carbonyl carbon. The accumulation of density along the C≡O carbonyl bond is apparent. The agreement between experimental deformation density maps (a and b) and theoretical ones (c and e) are excellent at these regions. The lone pair electron density of the oxygen atom shown in the theoretical map (Figure 2c,e) is not observable in experimental maps (Figure 2a) and only slightly observable in the static model density map (Figure 2b). This is probably due to the limited range of data measurements and unavoidable thermal smearing effect in the experimental data. However, near the Cr nucleus, there is a significant difference between b and c in Figure 2. The asymmetric distribution around the Cr atom in $\Delta\rho_{X-X}$, $\Delta\rho_{M-A}$, is quite pronounced; that is, there is positive deformation density along the direction at the bisection of ∠C4−Cr−C3 (or ∠C5−Cr−C1), but no accumulation is observed along the direction at the bisection of ∠C4−Cr−C1 (or ∠C3−Cr−C5). It is worth mentioning that this direction (bisection of ∠C4−Cr−C1) is the plane of the carbene fragment. This is not expected on the basis of the simple crystal field theory around Cr. If we take a close look at the corresponding theoretical maps, the asymmetric distribution does exist near the Cr (Figure 2c) as well. To clarify this feature, a plot showing the positive contour only is given in Figure 2d, where it is clear that the positive deformation density is significantly more in one direction (bisection of ∠C4−Cr−C1) than the other. Such asymmetric distribution is similar to that observed in Figure 2b. A similar observation is made in the DFT calculation (Figure 2e). Obviously, the plane of the carbene fragment does play a certain role in such asymmetric density distribution around the Cr atom. The residual density in Figure 2f simply demonstrates the validity of the multipole model. The deformation density maps of the carbene plane and the plane perpendicular to it are shown in Figure 3 and 4, respectively. Other than the asymmetric distribution near Cr, all the features are in very good agreement between experiment (Figure 3a, 4a) and theory (Figure 3b,c, 4b,c); for example, the features along the Cr−C6, C6−C8 bonds and the C8−C9 triple bond agree very well with each other.

TABLE 5: Charges of Fragments of (a) 1; (b) 2[a]

(a)	HFSCF		CASSCF(6,6)		DFT		multi-
fragment	MPA	NPA	MPA	NPA	Hirshfeld	MPA	pole
$(CO)_5Cr$:	−0.06	−0.18	−0.03	−0.17	−0.11	−0.23	−0.38
:C(OH)	+0.06	+0.18	+0.03	+0.17	+0.11	+0.23	+0.38
(C≡CH)							

	HFSCF		CASSCF(6,6)		DFT	
(b) fragment	MPA	NPA	MPA	NPA	Hirshfeld	MPA
$(CO)_5Cr$:	−0.25	−0.31	−0.24	−0.30	−0.23	−0.43
$:C(NH_2)CH_3$	+0.25	+0.31	+0.24	+0.30	+0.23	+0.43

[a] MPA: Mulliken population analysis. NPA: Natural orbital population analysis.

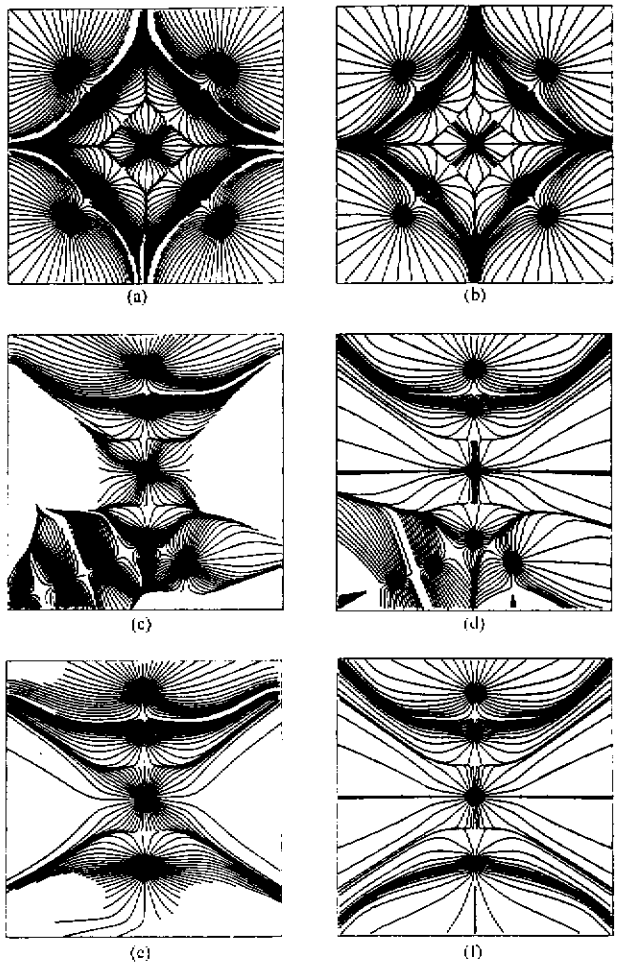

Figure 8. Gradient vector field, $\nabla\rho(r)$, of the electron density of **1**: a−f are defined as in Figure 6.

The discrepancy found near Cr may be partially due to the thermal effect since the correlation between the multipole coefficients and the thermal parameters can not be neglected; data measured at even lower temperature (e.g. 10 K) may resolve such problems in this respect.[40a,86] Deformation density maps of three planes (as in Figures 2, 3, and 4) are calculated via HF and DFT methods on an amino carbene complex **2**. The maps are displayed in Figure 5. The essential features are identical to those in Figures 2, 3, and 4.

Laplacian of Electron Density. The Laplacian of the electron density, $\nabla^2\rho(r)$, can also display the density accumulation (where $\nabla^2\rho(r) < 0$) and the density depletion ($\nabla^2\rho(r) > 0$). The advantage of the Laplacian over deformation is that it is unbiased from the promolecular model.[20,87−89] The negative Laplacians, $-\nabla^2\rho(r)$, on three unique planes both from experiment and from HF calculation are shown in Figure 6. The

TABLE 6: Topological Properties of Bond Critical Points of (a) 1 and (b) 2

(a) 1st line from experiment; 2nd line from theory; (b) from theory

(a) bond distance[a] (Å)	d1[b] (Å)	d2[b] (Å)	Hessian eigenvalues (e Å^{-5}) λ_1	λ_2	λ_3	$\nabla^2\rho(r_c)$[c] (e Å^{-5})	$\rho(r_c)$ (e Å^{-3})	ϵ[d]	$\lvert\lambda_1\rvert/\lambda_3$
Cr−C_{cis}[e]	0.957	0.953	−4.33	−3.92	19.12	10.87	0.78	0.11	0.23
1.910	0.921	0.989	−1.46	−1.43	19.18	16.29	0.61	0.02	0.07
Cr−C_{trans}[e]	0.973	0.935	−4.30	−3.94	20.62	12.38	0.78	0.09	0.21
1.906	0.923	0.987	−1.82	−1.01	19.15	16.32	0.61	0.81	0.10
Cr−C_{carb}	0.998	1.013	−3.82	−3.44	16.66	9.41	0.68	0.11	0.23
2.011	0.942	1.069	−1.44	−1.15	15.55	12.96	0.56	0.26	0.09
$(C-O)_{cis}$[e]	0.414	0.729	−38.11	−36.34	61.58	−12.87	3.39	0.05	0.62
1.143	0.388	0.755	−34.55	−34.52	78.90	9.83	2.67	0.00	0.44
$(C-O)_{trans}$	0.404	0.744	−37.13	−34.34	76.80	5.33	3.22	0.08	0.48
1.147	0.390	0.757	−34.08	−33.96	76.88	8.83	2.65	0.00	0.44
C_{carb}−O	0.537	0.785	−17.71	−16.19	20.80	−13.10	2.14	0.09	0.85
1.321	0.441	0.880	−17.16	−10.81	25.86	−2.11	1.68	0.59	0.66
C_{carb}−C8	0.694	0.723	−14.86	−12.79	12.60	−15.05	1.91	0.16	1.18
1.416	0.667	0.749	−13.08	−12.48	8.58	−16.98	1.68	0.05	1.52
C8−C9	0.515	0.706	−19.53	−16.92	15.23	−21.22	2.73	0.15	1.28
1.220	0.593	0.629	−15.13	−14.60	2.51	−27.23	2.29	0.04	6.03
(b)									
Cr−C_{cis}	0.914	0.970	−1.75	−1.55	20.31	17.01	0.65	0.13	0.09
1.884									
Cr−C_{trans}	0.907	0.950	−1.90	−1.50	21.40	18.00	0.70	0.26	0.09
1.857									
Cr−C_{carb}	0.965	1.117	−1.06	1.00	13.05	10.99	0.49	0.07	0.08
2.081									
$(C-O)_{cis}$	0.387	0.751	−35.36	−35.31	82.27	11.60	2.71	0.00	0.43
1.135									
$(C-O)_{trans}$	0.390	0.757	−34.07	−34.01	76.29	8.21	2.66	0.00	0.45
1.152									
C_{carb}−N	0.437	0.857	−20.38	−14.16	23.59	−10.96	1.99	0.44	0.86
1.293									
C_{carb}−C7	0.761	0.726	−11.14	−10.66	9.12	−12.68	1.51	0.04	1.22
1.486									

[a] Obtained from multipole refinement. [b] *d1*, *d2*: distances from BCP to the first and second atom of the bond. [c] Laplacian at critical point (BCP) $\nabla^2\rho(r_c) = (\lambda_1 + \lambda_2 + \lambda_3)$. [d] Ellipticity, $\epsilon = |\lambda_1/\lambda_2| - 1$. [e] Average value of four cis ones.

agreement between experiment and theory is very good, and the feature in the bond density accumulation is quite in correspondence with that in the deformation density. To clarify the asphericity in electron density near the Cr nucleus, the enlarged Laplacian maps at the Cr center are displayed in Figure 7. The accumulation in the d_π directions and the depletion along the d_σ (Cr−C) directions are clearly depicted. Unlike the descrepancies found in experimental and theoretical deformation density around Cr, the features in the density concentration and density depletion are similar between experiment and theory, but the valence shell charge concentration (VSCC)[33] in experimental maps (Figure 7c,e) tilts by a small angle (~10°) with respect to that in theoretical ones (Figure 7d,f). The inner shells of the Cr core are also displayed neatly in this figure. It seems advantageous using the Laplacian over deformation density to investigate the aspheric density distribution around the 3d transition metal, where the density accumulation and the density depletion are derived solely on the total electron density; no promolecular density is required. The corresponding theoretical Laplacian maps on amino carbene **2** give almost the same feature as in Figure 6 and 7; they are provided in the Supporting Information.

d Orbital Population and Net Atomic Charge. The d orbital populations of the Cr atom in compounds **1** and **2** are listed in Table 4, where the experiment is available only for compound **1**. The calculated ones include ab initio calculations at both HFSCF and CASSCF(6,6) levels and the DFT method. The agreement between various calculations in different partitions is reasonable, with less population on d_σ orbitals (d_{xy} and d_{z^2}) than on d_π orbitals ($d_{x^2-y^2}$, d_{yz}, and d_{xz}). No difference in d orbital populations is detectable between alkoxy- and amino-chromium carbenes, just as they are in Laplacian maps. The difference in atomic charges between the HFSCF and CASSCF calculations is minimal, but the difference in charges from various ways of partition is large. These differences are discussed extensively elsewhere.[90] Nevertheless, it is interesting to notice that charges of two fragments shown in Table 5 are such that the $(CO)_5Cr$ fragment is an electron acceptor (−0.38) and the carbene fragment, $:C(XR_1)(R_2)$, is an electron donor (+0.38) in experiment, which is in accord with all the calculations in compound **1**. The electron donor/acceptor roles for the two fragments are therefore clear.

Gradient Vector Field and Bond Critical Points. The gradient vector field on the total electron density of **1**, $\nabla\rho(r)$, is depicted in Figure 8 with three projections around the Cr atom. The agreement between experiment and theory is reasonably good. The bond critical point (BCP) and the atomic basin (domain) are easily recognized from the figure. To clarify such BCP and atom domain, the BCP of each chemical bond and atom domain are displayed in Figure 9 together with the bond path and the total electron density. Again the agreement between experiment and theory is good. The detailed properties at the BCP are given in Table 6, where λ_1, λ_2, and λ_3 are the eigenvalues of the Hessian matrix at the BCP, representing the Laplacian values perpendicular (λ_1, λ_2) and along (λ_3) the bond direction.[33] Apparently all Cr−C bonds can be characterized as a closed shell interaction according to the positive Laplacian value at the BCP and with $\rho(r_c)$ and $|\lambda_1|/\lambda_3$ values much less than 1. This is consistent with the results from the NBO analysis in either the HF or CASSCF calculation, where the Cr−C bond is analyzed as partially dative and partially covalent. The carbonyl C≡O and C≡C triple bonds obviously belong to shared

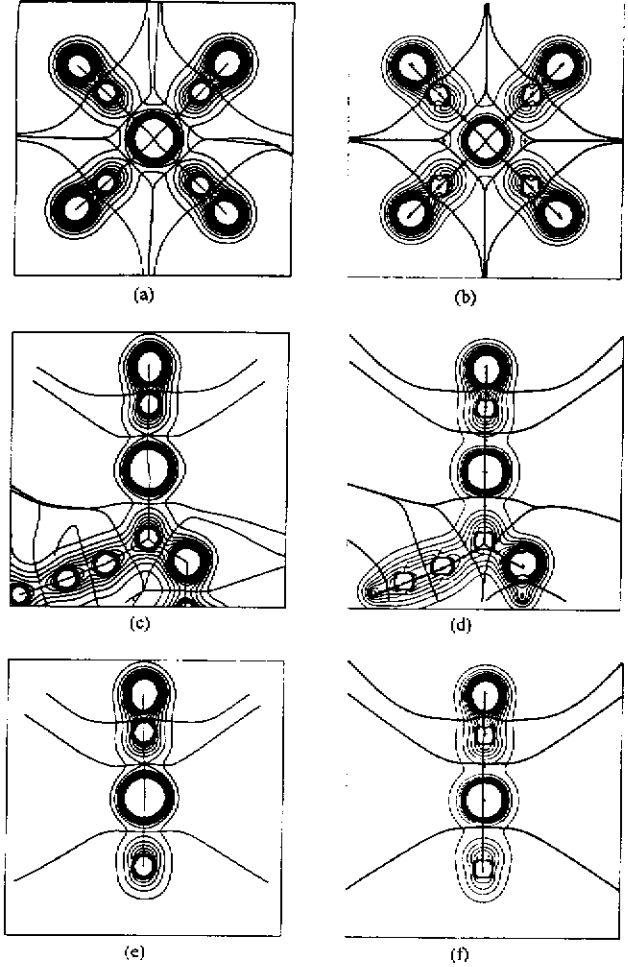

Figure 9. Total density, bond path, and atom domain of **1**: a−f are defined as in Figure 6. Contour interval of total density 0.4 e Å^{-3}.

interactions with high $\rho(r_c)$ and low ellipticity (ϵ). The positive Laplacian value of C≡O from theory was also found earlier on carbon monoxide by Bader et al.[33] due to the density polarization or transfer of charge from C to O in such a short bond. This is a general observation for all short C−O bonds with the result that the BCP lies just within the inner shell of charge depletion, thus making λ_3 a very large positive value. However, the large negative values of λ_1 and λ_2 are still indicative of a strong shared interaction for all the carbonyl C−O bonds. If only λ_1, λ_2 values are taken into account, the values of $(C-O)_{trans}$ and $(C-O)_{cis}$ in **1** are the same, but the values of $(C-O)_{cis}$ are slightly more negative than those of $(C-O)_{trans}$ in **2**, indicating that $(C-O)_{cis}$ is a slightly stronger bond than $(C-O)_{trans}$. This is in agreement with the NBO analysis of CASSCF result. In this respect, the experimental one seems better represented because the BCP from experiment is located not so close to C(d1) as that of the theoretical one. The values of $\rho(r_c)$ are in agreement with the bond order obtained from NBO analyses. However, the $\rho(r_c)$ values of $(C-O)_{cis}$ and $(C-O)_{trans}$ in **2** are not so much different as indicated in the NBO analysis.

Frontier Orbitals. Molecular orbital calculation based on the HFSCF method indicates that the LUMO of the title complex mainly consists of a π^*_{Cr-C6} and a π^*_{C8-C9}, with high coefficients on the carbene carbon (C6) and acetylene carbon atoms (C8, C9). The 1,3-dipolar cycloaddition is known to take place at the triple bond (C8≡C9).[91,92] The catalytic effects of the Fischer carbene toward the diene cycloaddition reaction can be interpreted as the HOMO/LUMO energy gap of the Fischer carbene being far less than those of corresponding ketones.

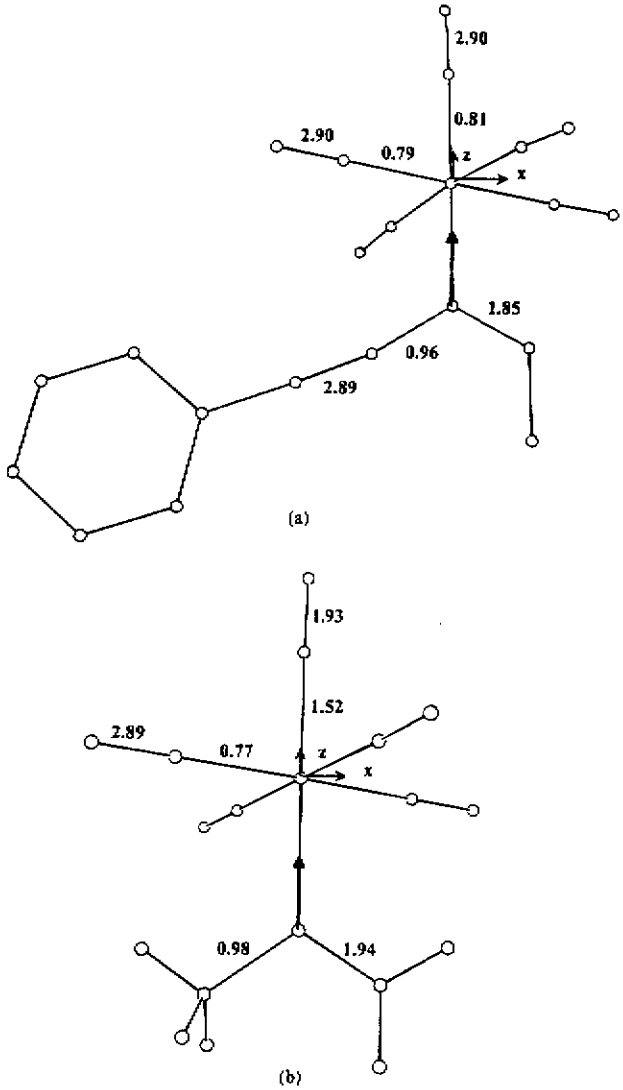

Figure 10. Local coordinate (Cr) and bond orders of (a) **1** and (b) **2** derived from CASSCF(6,6) calculations.

CASSCF. The result of CASSCF(6,6) shows that the HF ground state is obviously the dominant configuration, with a coefficient of 0.95 for both **1** and **2**. Similar results are found in CI calculations of molybdenum carbene, with the coefficient of the HF ground state being 0.98 and 0.97 for $(CO)_5Mo{=}CH(OH)$ and $(CO)_5Mo{=}CH_2$, respectively.[19] The following CASSCF(8,8) calculation[21] on the latter compound gives 0.94. The double excitations ($\pi_1^2 \rightarrow \pi_1^{*2}\sigma^2 \rightarrow \sigma^{*2}$, $\pi_2^{*2} \rightarrow \pi_2^{*2}\sigma\pi_1 \rightarrow \sigma^*\pi_1^*$, and $\sigma\pi_2 \rightarrow \sigma^*\pi_2^*$) are the important configurations, with coefficients in the range 0.10−0.17 for both compounds. Detailed analyses of the chemical bonds via wave functions obtained from HFSCF and CASSCF(6,6) calculations are performed using NBO analysis. The bond orders of the two molecules **1** and **2** from CASSCF(6,6) are listed in Figure 10. It is interesting to note that the main difference in the bond orders given in the figure is that the trans $Cr-C_{carbonyl}$ and carbonyl C−O bonds of **2** are of double-bond character, whereas in **1** the trans $Cr-C_{carbonyl}$ is still a single bond. This CAS result is consistent with the corresponding bond distances (Table 3). For $Cr-C_{carbene}$ and C−X bonds, they are a single and double bond, respectively, in both compounds. cis $Cr-C_{carbonyl}$ are all single and cis carbonyl C−O are all triple bonds. C8−C9 in **1** is a triple bond. Further detailed analyses of $Cr-C_{carbene}$, $Cr-CO_{trans}$, $C_{carbene}-O$ and $(C-O)_{trans}$ bonds of **1** into σ and π

TABLE 7: Natural Hybrid Orbital Analysis and Bond Occupancies of (a) 1; (b) 2

(a)

	$Cr-C_{carbene}$ HFSCF			$C_{carbene}-O$ HFSCF			$Cr-C_{trans}$ HFSCF			$(C-O)_{trans}$ HFSCF	
	NHO(%)	occ.		NHO(%)	occ.		NHO(%)	occ.		NHO(%)	occ.
σ	C sp_z(100)	1.557	σ	C sp_xp_z(30) O sp_xp_z(70)	1.991	σ	Cr sd_z^2(23) C sp_z(77)	1.952	σ	C sp_z(30) O sp_z(70)	1.997
n	Cr d_{yz}(100)	1.578	π	C p_y(11) O p_y(89)	1.994				π_x	C p_x(22) O p_x(78)	1.999
n	Cr d_{xz}(100)	1.756							π_y	C p_y(22) O p_y(78)	1.996
	CASSCF			CASSCF			CASSCF			CASSCF	
	NHO(%)	Occ.		NHO(%)	Occ.		NHO(%)	Occ.		NHO(%)	Occ.
σ	C sp_z(100)	1.554	σ	C sp_xp_z(30) O sp_xp_z(70)	1.992	σ	Cr sd_z^2(23) C sp_z(77)	1.953	σ	C sp_z(30) O sp_z(70)	1.997
n	Cr d_{yz}(100)	1.584	π	C p_y(13) O p_y(87)	1.992				π_x	C p_x(22) O p_x(78)	1.999
n	Cr d_{xz}(100)	1.749							π_y	C p_y(23) O p_y(77)	1.997

(b)

	$Cr-C_{carbene}$ HFSCF			$C_{carbene}-N$ HFSCF			$Cr-C_{trans}$ HFSCF			$(C-O)_{trans}$ HFSCF	
	NHO(%)	occ.		NHO(%)	occ.		NHO(%)	occ.		NHO(%)	occ.
σ	C sp_z(100)	1.584	σ	C sp_xp_z(36) N sp_xp_z(64)	1.990	σ	Cr sd_z^2(25) C sp_z(75)	1.949	σ	C sp_z(30) O sp_z(70)	1.998
n	Cr d_{yz}(100)	1.694	π	C p_y(17) N p_y(83)	1.996				π_x	C p_x(22) O p_x(78)	1.999
n	Cr d_{xz}(100)	1.767							π_y	C p_y(22) O p_y(78)	1.997
	CASSCF			CASSCF			CASSCF			CASSCF	
	NHO(%)	Occ.		NHO(%)	Occ.		NHO(%)	Occ.		NHO(%)	Occ.
σ	C sp_z(100)	1.585	σ	C sp_xp_z(36) N sp_xp_z(64)	1.990	σ	Cr sd_z^2(23) C sp_z(77)	1.949	σ	C sp_z(30) O sp_z(70)	1.997
n	Cr d_{yz}(100)	1.592	π	C p_y(20) N p_y(80)	1.995	π	Cr d_{xz}(93) C p_x(7)	1.833	π_y	C p_y(22) O p_y(78)	1.998
									n	O p_x(100)	1.586

characteristics from both HFSCF and CASSCF calculations are listed on Table 7a. The p_π orbital of the carbene carbon forms a π bond with the p_π orbital of the O atom in both results. The π bond density is not evenly distributed between the two centers but polarized toward O (87% from O); that is, there is little π density on the carbene carbon in either case. This leads to a feasible understanding of the nucleophilic attack at the carbene carbon site. The same analyses on compound **2** are given in Table 7b, where the $Cr-C_{carbene}$ bond is single in both HFSCF and CASSCF calculations; however the $Cr-CO_{trans}$ bond is double in CASSCF. The π bond is formed between d_{xz} of Cr and p_x of C_{trans} but with dominant contribution (93%) from Cr. The $C_{carbene}-N$ double bond is again mainly contributed from the N p_y orbitals (80%). So in compound **2**, the density along the p_y direction of the carbene carbon is also small (20%).

Orbital Correlation Diagram. A useful way of understanding the nature of the $Cr-C_{carbene}$ bond is to correlate the MOs of the metal carbonyl fragment with the MOs of the carbene fragments, where one fragment, $:Cr(CO)_5$, is in C_{4v} symmetry and the other fragment, $:C(OH)(C{\equiv}CH)$ or $:C(NH_2)CH_3$, is in C_s symmetry. Orbital correlation diagrams of **1** and **2** are given in Figure 11a,b. Five d orbitals of Cr are split into b_2, e, a_1, and b_1 states in C_{4v}. The a_1 (d_{z^2}) orbital, which is pointed toward the carbene carbon, forms a σ bond with the sp^2 hybrid orbital of the carbene carbon, and one of the e orbitals (a″ in C_s) forms a π bond with the p_π orbital of the carbene carbon. According to these correlation diagrams, it is clear that the carbene fragment mainly serves as a σ donor but only slightly as a π acceptor. The Cr−C π bond orbital (a″) can be described as the combination between the d_{yz} orbital of Cr and the π_{C-X} and π^*_{C-X} of carbene, shown in Figure 11. Therefore this π bond is best described as a three-centered four-electron π bond. Thus, it is reasonable to say that the π bond density is very polarized toward Cr or X atoms. The σ donor character is consistent with the fragment charge given above, where the carbene fragment is positive and the $(CO)_5Cr$ fragment is negative. One important fact is that the energy of the π^*_{C-N} orbital of the carbene fragment in **2** is very close to that of $\pi^*_{CO(trans)}$. Contrarily, the energy of the $\pi^*_{C-O,carbene}$ orbital of compound **1** is far lower than that of $\pi^*_{carbonyl}$. This gives a plausible explanation for the π bond being formed at $Cr-CO_{trans}$ in **2** but not in **1**.

Fermi Hole Density. The Fermi hole function is useful in describing the electron delocalization[93] and in leading to the understanding of electron pairs.[94] Such Fermi hole functions are applied to the bonding characterization of $(OC)_{trans}-Cr-C-X$. The reference electron (●) is placed on four atoms successively, but 0.5 au above the nuclear position in the π bond direction; the results of **1** and **2** are displayed in Figure 12. The delocalized π character through the trans carbonyl group is clearly indicated when the reference electron is at Cr. The three-centered π bond is apparent when the reference electron is placed on either $C_{carbene}$ or X. But the difference between the bonding of $Cr-CO_{trans}$ on **1** and **2** based on the

TABLE 8: Observed and Calculated Ionization Potentials for $(CO)_5Cr(XR')R$

orbital	observed[5]	DFT	HF	Fenske−Hall[5]
		$XR' = NH_2$; $R = C_6H_5$		
Cr $3d_{yz}$	7.25	7.77	8.29	8.12
Cr $3d_{xz}$	7.52	7.98	8.34	8.60
Cr $3d_{x^2-y^2}$	7.73	8.16	8.67	8.89
Ph	9.23	9.18	9.79	14.59
Ph	9.52	9.34	9.97	14.84
σ^*	9.80	10.18	11.99	12.15
C−N		11.06	13.81	18.83
Ph	10.52	11.44	14.26	17.92
Ph		11.60	14.53	18.65
		$XR' = NMe_2$; $R = C_6H_5$		
Cr $3d_{yz}$	7.02	7.49	8.05	7.94
Cr $3d_{xz}$	7.26	7.72	8.19	8.33
Cr $3d_{x^2-y^2}$	7.54	7.92	8.56	8.75
Ph	8.87	8.80	9.48	14.43
Ph	8.87	9.10	9.74	14.45
σ^*	9.49	9.94	11.73	11.74
C−N	10.58	10.36	12.37	15.98
Ph	10.16	11.23	14.31	17.71
Ph	10.96	11.37	14.35	18.16
		$XR' = OMe$; $R = C_6H_5$		
Cr $3d_{yz}$	7.39	7.83	8.30	8.27
Cr $3d_{xz}$	7.78	8.23	8.73	9.11
Cr $3d_{x^2-y^2}$	7.78	8.85	9.05	9.15
σ^*	9.26	8.98	9.41	11.28
Ph	9.66	9.01	9.78	14.36
Ph	10.06	9.81	11.78	14.53
Ph		10.73	13.37	17.90
Ph		11.40	14.09	18.22
		$XR' = NH_2$; $R = CH_3$		
Cr $3d_{yz}$	7.45	8.05	8.15	8.03
Cr $3d_{xz}$	7.80	8.26	8.35	8.51
Cr $3d_{x^2-y^2}$	7.80	8.46	8.68	8.79
σ^*	10.31	10.03	11.57	12.41
C−N		11.74	14.08	18.08
		$XR' = NH_2$; $R = (CH_3)_2$		
Cr $3d_{yz}$	7.12	7.48	8.01	7.79
Cr $3d_{xz}$	7.35	7.68	8.03	8.18
Cr $3d_{x^2-y^2}$	7.61	7.93	8.54	8.60
σ^*	9.72	9.19	10.71	11.86
C−N	10.67	10.20	11.92	16.09

TABLE 9: Bond Dissociation Energies (BDE, kcal/mol) of $M-C_{carbene}$

compound	BDE	type of calculation	ref
$(CO)_5CrC(OH)(C{\equiv}CH)$	38.4	HFSCF[a]	this work
	76.2	CASSCF(6,6)[a]	this work
	76.8	DFT(LDA)[a]	this work
	54.9	DFT(LDA/NL/BP)[a]	this work
	48.5	DFT(LDA/NL/BLYP)[a]	this work
$(CO)_5CrC(NH_2)CH_3$	40.5	HFSCF[a]	this work
	77.9	CASSCF(6,6)[a]	this work
	75.3	DFT(LDA)[a]	this work
	54.0	DFT(LDA/NL/BP)[a]	this work
	47.3	DFT(LDA/NL/BLYP)[a]	this work
$(CO)_5CrCH_2$	66.4	DFT(LDA/NL/BP)	32a,c
	66.9	DFT(LDA/NL/BP)	32a,c
$(CO)_5CrCH(OH)$	44	HFSCF	7
$[(CO)_5MnCH_2]^+$	75.9	DFT(LDA/NL/BP)	32c
$(CO)_5MoCH_2$	76.2	CASSCF(8,8)	32c, 21a
	55.7	MCSCF(GMO-CI)	19
	60.5	DFT(LDA/NL/BP)	32(a,c)
$Cr(CO)_6$	36.8	experiment	96
	21.0	HF	97
	62.1	DFT(LDA)	98
	45.9	DFT(LDA/NL/BP)	99
	36	DFT(LDA/NL/BLYP)	99

[a] Refers to a dissociation into two singlet fragments being 6.0 Å apart.

CASSCF result is not observed here, because the Fermi hole function is based on the HF calculation.

Ionization Potentials. Photoelectron spectroscopic data of nine pentacarbonylchromium−carbene complexes are available in the literature.[5] The corresponding molecular orbital (Fenske−Hall)[5] calculations are also available. The VIPs are calculated based on Koopmann's theory.[60] We have calculated the ionization potentials of five carbene complexes using ab initio/HF and DFT methods. The acquired values are listed in Table 8 in comparison with the measured ones.[5] It is obvious that values obtained in this work are far closer to the experimental ones than those from earlier calculations,[5] and values from DFT are better than those from HF. However it needs to be pointed out that the values from DFT are calculated on the basis of the transition state.[61−63] If we plotted the calculated values with respect to the observed ones as a linear function, the slope in DFT values is often close to 1, as found elsewhere.[95] One example on the first compound ($XR' = NH_2$, R = Ph) is such that the slopes are 1.00, 1.57, and 2.92 and the intercepts are 0.37, −3.60, and −13.50 respectively for DFT, ab initio/HF, and Fenske−Hall[5] calculations.

Bond Dissociation Energy. The BDEs of the metal carbene bond of Fischer-type carbenes have been investigated extensively.[7,9,21,32] Relevant BDEs are given in Table 9. The earlier work based on HFSCF gave 44 kcal/mol for the Cr−$C_{carbene}$ bond in $(CO)_5CrCH(OH)$.[7] Calculations at the post HF level yielded 56 and 60 kcal/mol[19] for the Mo−C bond in $(CO)_5MoCH_2$ and $(CO)_5MoCH(OH)$ respectively. The recent DFT calculation[32] gives 67 and 76 kcal/mole for $(CO)_5CrCH_2$ and $[(CO)_5MnCH_2]^+$, respectively. Apparently, the effect on electron correlation and nonlocal correction on DFT is important in such BDEs. In this work, BDEs based on CASSCF(6,6) give 76 and 78 kcal/mol respectively for compounds **1** and **2**. The ones based on DFT(LDA/NL/BP) give 55 and 54 kcal/mol correspondingly. The ones on DFT(LDA/NL/BLYP) give even lower energy of 48 and 47 kcal/mol. The magnitude in energy difference of the BDE with and without nonlocal corrections (BP, BLYP) in these two compounds is similar to that of the Cr−C bond in $Cr(CO)_6$.[96−99] Unfortunately, no experimental value that we are aware of is available for the Cr−$C_{carbene}$ bond. However, on the basis of the $Cr(CO)_6$ example (Table 9), the value from DFT with nonlocal correction BLYP gives the closest value to the experimental one. Both CASSCF and DFT/LDA results overestimate the energy, but the HF result underestimates the BDE.

Conclusion

This is a comparative study between experiment and theory that makes use of the energy, the electron density, and its topology. Experimental deformation density and topological analyses of compound **1** are in good agreement with those calculated from molecular orbital calculations. The asphericity in electron density around the Cr atom or the d orbital populations of Cr is in accord with the crystal field theory. Orbital energies calculated from DFT are close to the measured values from PES. The bonding characteristics of Fischer-type carbenes are as follows: the Cr−$C_{carbene}$ σ bond is formed by electron donating from the carbene carbon. The Cr−$C_{carbene}$ π bond is actually a Cr−C−X three-centered four-electron π bond having the π density largely located at both Cr and X. The difference in bonding of carbenes between X = O and X = N

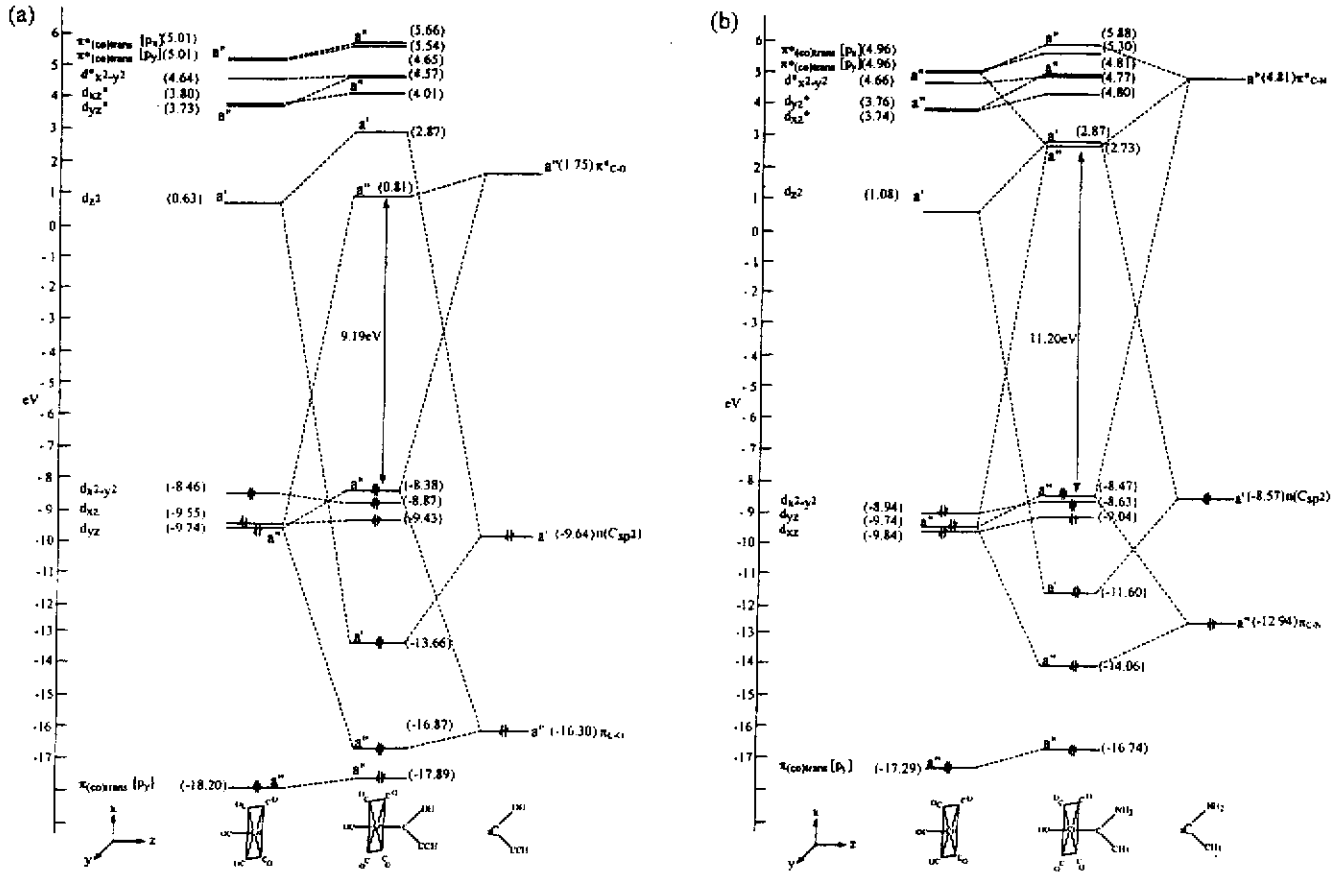

Figure 11. Orbital correlation diagram of (a) **1** and (b) **2**.

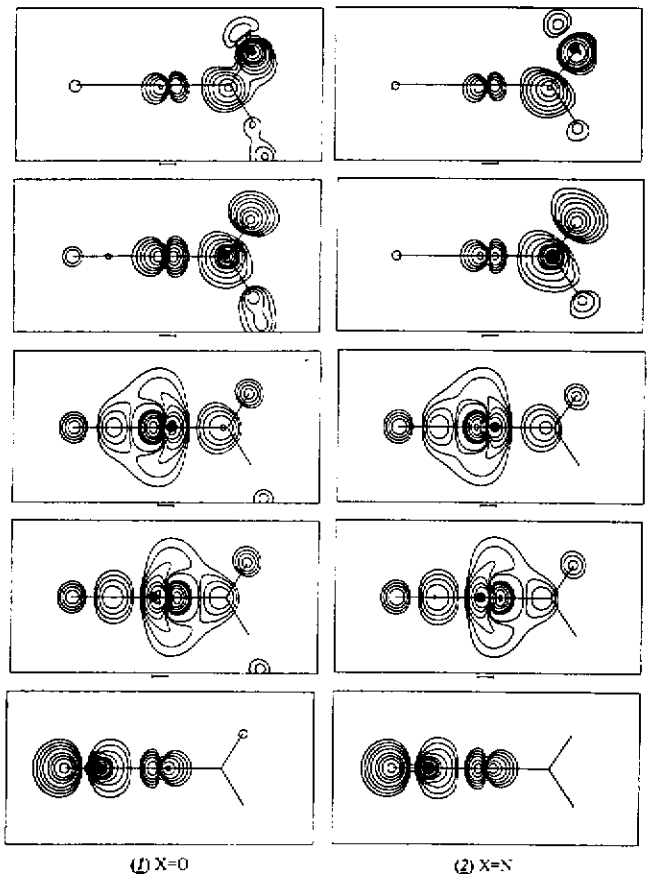

Figure 12. Fermi hole density with the reference electron (●) placed at 0.5 au above the plane. The right column is of **1** and the left column is of **2**. The contours are in atomic unit with $2^j \times 10^i$ ($i = 0, 1, 2, 3$; $j = -3, -2, -1$).

is in the $M-CO_{trans}$ bond. The summary of the bonding character is described in the following diagram.

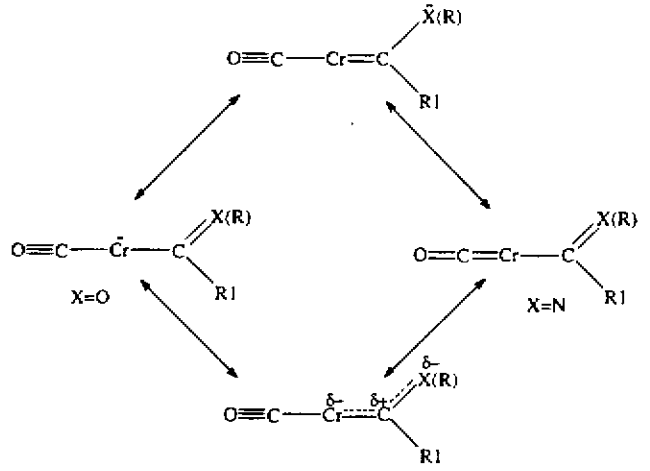

Acknowledgment. Financial support of this work from the National Science Council of ROC is appreciated. Thanks are due to the National Center for High Performance Computing for providing computing facilities and software packages. Special thanks go to Professor R. F. W. Bader, Professor N. Hansen, and Professor M. Souhassou for their kindly supplies of AIMPAC, SALLY, and PROP programs respectively.

Supporting Information Available: Tables of crystal data, atomic coordinates and thermal parameters, and bond distances and angles of compounds **1**−**4** and multipole coefficients of compound **1**. Figures of negative Laplacian of electron density of **2**, negative Laplacian around Cr of **2**, gradient vector field of the electron density of **2**, and total density, bond path, and

atom domain of **2** (20 pages). Ordering information is given on any current masthead page.

References and Notes

(1) Collman, J. P.; Hegedus, L. S.; Norton, J. R.; Finke, P. G. *Principles and Application of Organometallic Metal Chemistry*; Mill Vally: CA, 1987.

(2) (a) Cardin, D. J.; Cetinkaga, B.; Lappert, M. F. *Chem. Rev. (Washington, D.C.)* **1972**, *72*, 545−574. (b) Adams, R. D. *Chem. Rev. (Washington, D.C.)* **1989**, *89*, 1703−1712.

(3) Fischer, E. O.; Maasböl, D. C. A. *Angew. Chem., Int. Ed. Engl.* **1964**, *3*, 580−581.

(4) (a) Schrock, R. R. *J. Organomet. Chem.* **1986**, *300*, 249−262. (b) Schrock, R. R. *Acc. Chem. Res.* **1979**, *12*, 98−104. (c) Schrock, R. R. *Acc. Chem. Res.* **1990**, *23*, 158−165.

(5) Block, T. F.; Fenske, R. F. *J. Am. Chem. Soc.* **1977**, *99*, 4321−4330.

(6) Spangler, D.; Wendoloski, J. J.; Dupuis, M.; Chen, M. M. L.; Schaefer, H. F., III. *J. Am. Chem. Soc.* **1981**, *103*, 3985−3990.

(7) Nakatsuji, H.; Ushio, J.; Han, S.; Yonezawa, T. *J. Am. Chem. Soc.* **1983**, *105*, 426−434.

(8) Goddard, R. J.; Hoffmann, R.; Jemmis, E. D. *J. Am. Chem. Soc.* **1980**, *102*, 7667−7676.

(9) Volatron, F.; Eisenstein, O. *J. Am. Chem. Soc.* **1986**, *108*, 2173−2179.

(10) Block, T. F.; Fenske, R. F.; Casey, C. P. *J. Am. Chem. Soc.* **1976**, *98*, 441−443.

(11) Kostic, N. M.; Fenske, R. F. *J. Am. Chem. Soc.* **1981**, *103*, 4677−4685.

(12) Hall, M. B.; Fenske, R. F. *Inorg. Chem.* **1972**, *11*, 768−775.

(13) Kostic, N. M.; Fenske, R. F. *Organometallics* **1982**, *1*, 489−496.

(14) Francl, M. M.; Pietro, W. J.; Hout, R. F.; Hehre, W. J. *Organometallics* **1983**, *2*, 281−286.

(15) Rappé, A. K.; Goddard, W. A., III. *J. Am. Chem. Soc.* **1977**, *99*, 3966−3968.

(16) Rappé, A. K.; Goddard, W. A., III. *J. Am. Chem. Soc.* **1982**, *104*, 448−456.

(17) Carter, E. A.; Goddard, W. A., III. *J. Am. Chem. Soc.* **1986**, *108*, 4746−4754.

(18) Marynick, D. S.; Kirkpatrick, C. M. *J. Am. Chem. Soc.* **1985**, *107*, 1993−1994.

(19) Taylor, T. E.; Hall, M. B. *J. Am. Chem. Soc.* **1984**, *106*, 1576−1584.

(20) Biré, A. S.; Dao, N. Q.; Strich, A.; Thieffry, C.; Bénard, M. *Inorg. Chem.* **1990**, *29*, 4908−4915.

(21) (a) Márquez, A.; Sanz, J. F. *J. Am. Chem. Soc.* **1992**, *114*, 2903−2909. (b) Márquez, A.; Sanz, J. F. *J. Am. Chem. Soc.* **1992**, *114*, 10019−10024. (c) Selmani, A.; Salahub, D. R. *J. Chem. Phys.* **1988**, *89*, 1529−1532.

(22) Cundari, T. R.; Gordon, M. S. *J. Am. Chem. Soc.* **1991**, *113*, 5231−5243.

(23) Cundari, T. R.; Gordon, M. S. *J. Am. Chem. Soc.* **1992**, *114*, 539−548.

(24) Roos, B. O.; Taylor, P. R.; Siegbahn, P. E. M. *Chem. Phys.* **1980**, *48*, 157−173.

(25) Siegbahn, P. E. M.; Almlöf, J.; Heiberg, A.; Roos, B. O. *J. Chem. Phys.* **1981**, *74*, 2384−2396.

(26) Mcdouall, J. J. W.; Robb, M. A. *Chem. Phys. Lett.* **1986**, *132*, 319−324.

(27) Ruedenberg, K.; Schmidt, M. W.; Gilbert, M. M.; Elbert, S. T. *Chem. Phys.* **1982**, *71*, 41−49.

(28) Ruedenberg, K.; Schmidt, M. W.; Gilbert, M. M. *Chem. Phys.* **1982**, *71*, 51−64.

(29) Poblet, J. M.; Strich, A.; Wiest, R.; Bénard, M. *Chem. Phys. Lett.* **1986**, *126*, 169−175.

(30) Ziegler, T. *Pure Appl. Chem.* **1991**, *28*, 1271.

(31) Ziegler, T. *Chem. Rev. (Washington, D.C.)* **1991**, *91*, 651−667.

(32) (a) Jacobsen, H.; Schreckenbach, G.; Ziegler, T. *J. Phys. Chem.* **1994**, *98*, 11406−11410. (b) Jacobsen, H.; Ziegler, T. *Organometallics* **1995**, *14*, 224−230. (c) Jacobsen, H.; Ziegler, T. *Inorg. Chem.* **1996**, *35*, 775−783.

(33) Bader, R. F. W. *Atoms in Molecules, A Quantum Theory*; Calendron Press: Oxford, 1990.

(34) Bader, R. F. W.; Essén, H. *J. Chem. Phys.* **1984**, *80*, 1943−1960.

(35) Carroll, M. T.; Cheeseman, J. R.; Osman, R.; Weinstein, H. *J. Phys. Chem.* **1989**, *93*, 5120−5123.

(36) Bader, R. F. W.; Nguyen−Dang, T. T.; Tal, Y. *J. Chem. Phys.* **1979**, *70*, 4316−4329.

(37) Zou, P. F.; Bader, R. F. W. *Acta. Crystallogr.* **1994**, *A50*, 714−725.

(38) Chan, K. S.; Wulff, W. D. *J. Am. Chem. Soc.* **1986**, *108*, 5229−5236.

(39) *International Tables for X−ray Crystallography*; Kynoch Press: Birmingham, U.K., 1974; Vol. IV.

(40) (a) Coppens, P.; Hall, M. B. *Electron Distribution and the Chemical Bond*; Plenum Press, New York, 1982. (b) Hansen, N. K.; Coppens, P. *Acta. Crystallogr.* **1978**, *A34*, 909−921. (c) Program producing static deformation density by Dr. N. K. Hansen, at the University of Nancy, France.

(41) Gabe, E. J.; Le Page, Y.; Charland, J.-P.; Lee, F. L.; White, P. S. *J. Appl. Crystallogr.* **1989**, *22*, 384−385.

(42) PROP program: A program developed by Sauhassou, M.; Hansen, N. K.; Stevens, E.; Craven, B.; Bouhmeida, N.; Ghermani, N.; Lecomte, C.

(43) Tsai, C. J. Master Thesis, National Taiwan University, Taiwan, 1982.

(44) Rappe, A. K.; Smedley, T. A.; Goddard, W. A., III. *J. Phys. Chem.* **1981**, *85*, 2607−2611.

(45) Wachters, A. J. H. *J. Chem. Phys.* **1970**, *52*, 1033−1036.

(46) (a) von Barth, U.; Hedin, L. *J. Phys. C* **1972**, *5*, 1629−1642. (b) Versluis, L.; Ziegler, T. *J. Chem. Phys.* **1988**, *88*, 3322−3330. (c) Hirshfeld, F. L. *Theor. Chim. Acta.* **1977**, *B44*, 129.

(47) Vosko, S. J.; Wilk, L.; Nusair, M. *Can. J. Phys.* **1980**, *58*, 1200−1211.

(48) Becke, A. D. *J. Chem. Phys.* **1986**, 84, 4524−4529. (b) Becke, A. D. *J. Chem. Phys.* **1988**, *88*, 1053−1062.

(49) Perdew, J. P. *Phys. Rev.* **1986**, *B33*, 8822.

(50) Reed, A. E.; Weinhold, F. *J. Chem. Phys.* **1985**, *83*, 1736−1740.

(51) Foster, J. P.; Weinhold, F. *J. Am. Chem. Soc.* **1980**, *102*, 7211−7218.

(52) Reed, A. E.; Curtiss, L. A.; Weinhold, F. *Chem. Rev. (Washington, D.C.)* **1988**, *88*, 899−926.

(53) Reed, A. E.; Weistock, R. B.; Weinhold, F. *J. Chem. Phys.* **1985**, *83*, 735−746.

(54) Löwdin, P. O. *Phys. Rev.* **1955**, *97*, 1474−1489.

(55) (a) Pauling, L. *J. Am. Chem. Soc.* **1931**, *53*, 1367−1400. (b) Coulson, C. A. *Valence*, 2nd ed.; Oxford University Press: London, 1952.

(56) McWeeny, R.; Diereksen, G. *J. Chem. Phys.* **1968**, *49*, 4852−4856.

(57) McWeeny, R. *Rev. Mod. Phys.* **1960**, *32*, 335.

(58) Bader, R. F. W.; Stephens, M. E. *Chem. Phys. Lett.* **1974**, *26*, 445.

(59) Bader, R. F. W.; Stephens, M. E. *J. Am. Chem. Soc.* **1975**, *97*, 7391−7399.

(60) Koopmans, T. *Physica (Utrecht)* **1933**, *1*, 104.

(61) Slater, J. C. *Adv. Quantum Chem.* **1972**, *6*, 1.

(62) Åsbrink, L.; Fridh, C.; Lindholm, E. *Chem. Phys. Lett.* **1977**, *52*, 69−71.

(63) Chong, D. P. *J. Chin. Chem. Soc.* **1992**, *6*, 20.

(64) Frisch, M. J.; Trucks, G. W.; Schlegel, H. B.; Gill, P. M. W.; Johnson, B. G.; Robb, M. A.; Cheeseman, J. R.; Keith, T. A.; Petersson, G. A.; Montgomery, J. A.; Raghavachari, K.; Al-Laham, M. A.; Zakrzewski, V. G.; Martin, R. L.; Ortiz, J. V.; Foresman, J. B.; Cioslowski, J.; Stefanov, B. B.; Nanayakkara, A.; Challacombe, M.; Peng, C. Y.; Ayala, P. Y.; Chen, W.; Wong, M. W.; Andres, J. L.; Replogle, E. S.; Gomperts, R.; Martin, R. L.; Fox, D. J.; Binkley, J. S.; Defrees, D. J.; Baker, J.; Stewart, J. P.; Head-Gordon, M.; Gonzalez, C.; Pople, J. A. *Gaussian 94* (Revision A.1); Gaussian Inc.: Pittsburg, PA, 1995.

(65) Delley, B. *J. Chem. Phys.* **1990**, 92, 508−517.

(66) Lichtenberger, D. L.; Fenske, R. F. MOPLOT. *QCPE* 1975.

(67) AIMPAC: a set of programs for the Theory of Atoms in Molecules: Bader, R. F. W., co-workers, Eds.: McMaster University, Hamilton, Ontario, Canada.

(68) Mills, O. S.; Redhouse, A. D. *J. Chem. Soc. A* **1968**, 642−647.

(69) Huttner, G.; Lorenz, H. *Chem. Ber.* **1975**, *108*, 1864−1870.

(70) (a) Perry, W. B.; Schaaf, T. F.; Jolly, W. L. *Inorg. Chem.* **1974**, *13*, 2038−2329. (b) Kruger, C.; Goddard, R.; Claus, K. H. *Z. Naturforsch.* **1983**, *B38*, 1431.

(71) Dotz, K. H.; Kuhn, W.; Ackermann, K. *Z. Naturforsch.* **1983**, *B38*, 1351.

(72) Dotz, K. H.; Kuhn, W.; Thewalt, U. *Chem. Ber.* **1985**, *118*, 1126.

(73) Klingler, R. J.; Huffman, J. C.; Kochi, J. K. *Inorg. Chem.* **1981**, *20*, 34−40.

(74) Aumann, R.; Hinterding, P.; Kruger, C.; Betz, P. *Chem. Ber.* **1990**, *123*, 1847.

(75) Sabat, M.; Gross, M. F.; Finn, M. G. *Organometallics* **1992**, *11*, 745−751.

(76) Baikie, P. E.; Fischer, E. O.; Mills, O. S. *Chem. Comm.* **1967**, 1199.

(77) Connor, J. A.; Mills, O. S. *J. Chem. Soc. A* **1969**, 334−341.

(78) Rudler, H.; Parlier, A.; Yefsah, R.; Denise, B.; Daran, J. C.; Vaissermann, J.; Knobler, C. *J. Organomet. Chem.* **1988**, *358*, 245−272.

(79) Alvarez, C.; Parlier, A.; Rudler, H.; Yefsah, R.; Daran, J. C.; Knobler, C. *Organometallics* **1989**, *8*, 2253−2259.

(80) Denise, B.; Goumont, R.; Parlier, A.; Rudler, H.; Daran, J. C.; Vaissermann, J. *J. Organomet. Chem.* **1989**, *377*, 89−104.

(81) Barluenga, J.; Aznar, F.; Martín, A.; García-Granda, S.; Pérez-Carreño, E. *J. Am. Chem. Soc.* **1994**, *116*, 11191−11192.

(82) Yang, D. C.; Dragisich, V.; Wulff, W. D.; Huffman, J. C. *J. Am. Chem. Soc.* **1988**, *110*, 307−309.

(83) Huttner, G.; Lange, S. *Chem. Ber.* **1970**, *103*, 3149.

(84) Cotton, F. A.; Richardson, D. C. *Inorg. Chem.* **1966**, *5*, 1851−1854.

(85) Gleichmann, M. M.; Dötz, K. H.; Hess, B. A. *J. Am. Chem. Soc.* **1996**, 118, 10551−10560.

(86) Fabius, B.; Cohen-Addad, C.; Larsen, F. K.; Lehmann, M. S.; Becker, P. *J. Am. Chem. Soc.* **1989**, *111*, 5728−5732.

(87) Schwarz, W. H. E.; Ruedenberg, K.; Mensching, L. *J. Am. Chem. Soc.* **1989**, *111*, 6926−6933.

(88) Kunze, K. L.; Hall, M. B. *J. Am. Chem. Soc.* **1987**, *109*, 7617−7623.

(89) Dunitz, J. D.; Seiler, P. *J. Am. Chem. Soc.* **1983**, *105*, 7056.

(90) (a) Cioslowski, J.; Hay, P. J.; Ritchie, J. P. *J. Phys. Chem.* **1990**, *94*, 148−151. (b) Wang, C. C.; Wang, Y.; Chou, L. K.; Che, C. M. *J. Phys. Chem.* **1995**, *99*, 13899−13008. (c) Lee, C. S.; Hwang, T. S.; Wang. Y.; Peng, S. M.; Hwang, C. S. *J. Phys. Chem.* **1996**, *100*, 2934−2941.

(91) (a) Wulff, W. D.; Bauta, W. E.; Kaesler, R. W.; Lankford, P. J.; Miller, R. A.; Murray, C. K.; Yang, D. C. *J. Am. Chem. Soc.* **1990**, *112*, 3642−3659. (b) Wulff, W. D.; Yang, D. C. *J. Am. Chem. Soc.* **1984**, *106*, 7565−7567.

(92) Sustmann, R.; Trill, H. *Angew. Chem., Int. Ed. Engl.* **1972**, *11*, 838−839.

(93) Bader, R. F. W.; Streitwieser, A.; Neuhaus, A.; Laidig, K. E.; Speers, P. *J. Am. Chem. Soc.* **1996**, *118*, 4959−4965.

(94) Bader, R. F. W.; Johnson, S.; Tang, T.-H.; Popelier, P. L. A. *J. Phys. Chem.* **1996**, *100*, 15398−15415.

(95) Hwang, T. S.; Chong, D. P.; Wang, Y. *J. Chin. Chem. Soc.* **1994**, *41*, 673−677.

(96) Lewis, K. E.; Golden, D. M.; Smith, G. P. *J. Am. Chem. Soc.* **1984**, *106*, 3905−3912.

(97) Ehlers, A. W.; Frenking, G. *J. Am. Chem. Soc.* **1994**, *116*, 1514−1520.

(98) (a) Li, J.; Schreckenbach, G.; Ziegler, T. *J. Am. Chem. Soc.* **1995**, *117*, 486−494. (b) Li, J.; Schreckenbach, G.; Ziegler, T. *J. Phys. Chem.* **1994**, *98*, 4838−4841.

(99) Jonas, V.; Thiel, W. *J. Chem. Phys.* **1995**, *102*, 8474−8484.

Topological Analysis of the Electron Density Distribution of Bis(diiminosuccinonitrilo)nickel, $Ni(C_4N_4H_2)_2$: Comparison between Experiment and Theory

Tsong-Song Hwang and Yu Wang

Department of Chemistry, National Taiwan University, Taipei, Taiwan, ROC

The Journal of
Physical Chemistry A®

Reprinted from
Volume 102, Number 21, Pages 3726–3731

Topological Analysis of the Electron Density Distribution of Bis(diiminosuccinonitrilo)nickel, $Ni(C_4N_4H_2)_2$: Comparison between Experiment and Theory

Tsong-Song Hwang and Yu Wang*,†

Department of Chemistry, National Taiwan University, Taipei, Taiwan, ROC

Received: July 29, 1997; In Final Form: November 10, 1997

A quantitative description of chemical bonds in bis(diiminosuccinonitrilo)nickel, $Ni(disn)_2$, is made in terms of topological properties of electron densities. These properties are obtained both from an X-ray diffraction experiment and from molecular orbital calculations. The asphericity in electron density around the Ni ion is surely observable from the Laplacian of the electron density with density accumulation in the d_π direction but density depletion along the d_σ (Ni−N) direction. On the basis of the topological properties at bond critical points, the bonding between Ni and the imino nitrogen atom is classified as mainly a closed-shell interaction but with some covalent character. The bonds within the ligand, disn, are all shared interactions, and the bond order is reflected clearly from the density at the critical point, $\rho(\mathbf{r}_c)$. The π-delocalization of the molecule is precisely indicated by the bond ellipticity and is illustrated by Fermi-hole distribution. Atom domains in the molecule are demonstrated. Molecular electrostatic potential is derived both from experiment and from MO calculations. For all the properties, the agreement between experiment and theory is reasonable.

Introduction

Charge density distribution of the title compound has been investigated recently through deformation density distribution on a combined experimental and theoretical study.[1] Topological theory of atoms in molecules[2] brings in a new insight into chemical bonding characterization. The bias[3−6] on how to deal with the proper model for the promolecule is no longer a worry since the topological analysis is based entirely on the total electron density of the molecule. This analysis has been mainly applied on the basis of molecular orbital calculations.[7−9] Recently, a few examples were given using experimental electron density.[10−14] Such application to experimental X-ray diffraction data requires the multipole model of atomic density.[15−17] The results of the topological analysis do provide precise information on chemical bonding which, in fact, enhances the value of such a multipole model. Since the bond topological properties give a quantitative characterization of chemical bonds, it is important to compare the properties derived both from experiment and from wave functions. Recently, the classification of chemical bonds based on topological analysis of electron localization functions (ELF)[18,19] demonstrated even clearer features concerning lone pairs and single, double, or triple bonds. The result of such ELF analysis correlates precisely with VSEPR theory. The purpose of this work is to obtain a quantitative characterization of chemical bonds through topological analysis in a combined experimental and theoretical study. The magnitude of the electron density at the bond critical point, $\rho(\mathbf{r}_c)$, correlates directly with the bond distance and the bond order. The Laplacian of electron density depicts the charge concentration and depletion. This topology of Laplacian of electron density also provides the physical basis for the Lewis and VSEPR models.[2,20−22] When $\nabla^2\rho(\mathbf{r}) < 0$, it means the electron density is locally concentrated at $\mathbf{r}$, and when $\nabla^2\rho(\mathbf{r}) > 0$, the electron density is locally depleted at $\mathbf{r}$. In addition, the Laplacian value at a (3, −1) bond critical point provides the description of the interaction between the bonded atoms as being closed shell (ionic) or electron shared (covalent).[2] The bond ellipticity, ϵ, is a direct indicator of the π bond character. The Fermi-hole function[23−25] is a measure of Pauli repulsion and is very useful for realizing the bond delocalization. Molecular electrostatic potential[26] (MEP) is helpful for predicting a long-range electrostatic interaction[27−33] such as protonation and intramolecular hydrogen bonds.

Computation Details

The total electron density of the molecule from experiment is calculated on the basis of the multipole parameters which are given in our previous work[1]. Although the exact molecular symmetry in the crystal is C_i, the actual geometry can be considered as D_{2h} within three standard deviations. The multipole coefficients, P_{lm}, were constrained in D_{2h} fashion.[1] Since we are mainly interested in the molecular properties, total electron density is only calculated for a single molecule both in experiment and in theory. The total electron density from theory is obtained by an ab initio molecular orbital calculation at HF level, which takes no account of electron correlation effects. The basis set of Ni atom is [14, 9, 5]/[6, 3, 2].[34] Basis sets of C, N, and H atoms are taken from 6-31G**. The geometry of the molecule is taken to be D_2h by imposing a C_2 symmetry on the coordinates obtained from X-ray diffraction data.[1]

A critical point (CP), $\mathbf{r}_c$, is a point satisfying the condition $\nabla\rho(\mathbf{r}_c) = 0$, where

$$\nabla\rho(\mathbf{r}) = i\frac{\partial\rho(r)}{\partial x} + j\frac{\partial\rho(r)}{\partial y} + k\frac{\partial\rho(r)}{\partial z}$$

This is made by the Newton−Raphson method, and the initial position can be assigned at a point near the expected CP. The gradient vector field of charge density is represented through a display of the trajectories traced out by the vector $\nabla\rho$. A

* To whom correspondence should be addressed.
† E-mail: yuwang@chem38.cn.ntu.edu.tw.

S1089-5639(97)02468-7 CCC: $15.00
Published on Web 04/30/1998

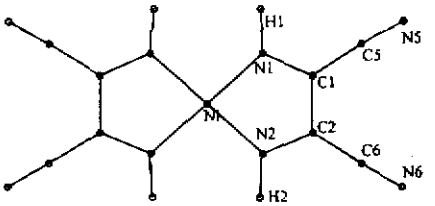

Figure 1. Molecular geometry and the atomic labeling of the molecule.

trajectory of $\nabla\rho$ (gradient path) starts from some arbitrary point $\mathbf{r}_0$ and moves with a step size of Δr in the direction of $\nabla\rho(\mathbf{r}_0)$ and then repeats with the same procedure at the next step until such path terminates. The gradient vector field map in this work is drawn in such a way that 48 equally spaced directions are started around each nucleus on the projected molecular plane. Bond paths are pairs of gradient vectors originated from bond critical point (BCP) and terminated at neighboring atomic nucleus, in other words, the path which goes through the maximum local density. An atom domain is a surface of zero flux which normally pass through BCPs and is perpendicular to bond paths; therefore, the atom domain characterizes a unique volume around each nucleus. MEP is obtained according to[26]

$$V(\mathbf{r}) = \sum_{\alpha}^{\text{nuclei}} \frac{Z_\alpha}{|r_\alpha - r|} - \int \frac{dr_1\, \rho(r_1)}{|r_1 - r|}$$

where Z_α and r_α are the charge and the location of nucleus α, respectively.

The Gaussian94 program[35] is used to do the MO calculations. The Fermi-hole function is calculated from HF calculation and displayed as a contour map to illustrate the electron delocalization. Molecular total electron density, BCP, bond path, atom domain, Laplacian, field gradient vector, and MEP are calculated using the PROP[36] and AIMPAC[37] programs respectively for experiment and theory.

Results and Discussion

Topological Properties and Critical Points. The molecular structure based on the diffraction data[1] is given in Figure 1. A local maximum in electron density corresponding to a (3, −3) CP is found at each atomic site in the molecule. A (3, −1) BCP is located at each chemical bond in the molecule. An additional (3, 1) ring critical point is found at the center of the five-membered ring both from experiment and from calculation.

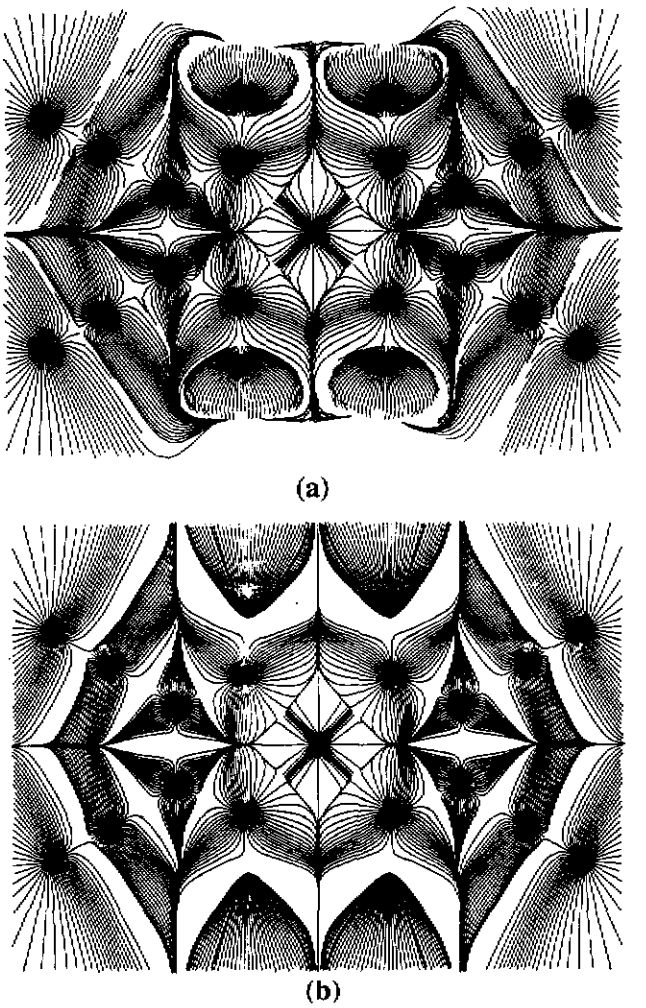

Figure 2. Gradient vector field from (a) experiment and (b) calculation.

Starting from the BCP, there is only one direction to go, uphill in the density, and such a path along the direction of the steepest ascent will always terminate at a (3, −3) CP, the nucleus. Such a trajectory is a topological bond path. The bond paths from experiment and from theory coincide well with the actual molecular structure. The only significant difference between experiment and theory is in the region very close to the Ni nucleus, where the bond path angle of N−Ni−N is slightly smaller as calculated than as found experimentally (black lines

TABLE 1: Properties Associated with Bond Critical Points (1st Line Experimental Values; 2nd Line Theoretical Values)

bond (BL (Å))[a]	d_1[b] (Å)	d_2[c] (Å)	Hessian eigenvalue[d] (e Å^{-5}) λ_1	λ_2	λ_3	$\nabla^2\rho(\mathbf{r}_c)$[e] (e Å^{-5})	ϵ $(\lvert\lambda_1/\lambda_2\rvert - 1)$	$\lvert\lambda_1/\lambda_3\rvert$	$\rho(\mathbf{r}_c)$ (e Å^{-3})
Ni−N1	0.91	0.92	−5.49	−5.17	22.94	12.28	0.06	0.24	0.94
(1.828)	0.86	0.97	−3.11	−2.74	26.27	20.41	0.14	0.12	0.78
N1−C1	0.81	0.52	−20.97	−16.67	16.98	−20.65	0.26	1.23	2.31
(1.332)	0.88	0.44	−20.51	−16.42	15.54	−21.39	0.25	1.32	2.39
C1−C2	0.70	0.72	−16.82	−13.77	12.72	−17.87	0.22	1.32	2.05
(1.411)	0.70	0.70	−17.55	−13.83	7.01	−24.36	0.27	2.50	2.18
C1−C5	0.72	0.71	−14.54	−12.98	13.68	−13.84	0.12	1.06	1.90
(1.432)	0.65	0.78	−14.87	−13.74	5.55	−23.06	0.08	2.68	1.99
C5−N5	0.46	0.70	−27.03	−25.73	30.41	−22.35	0.05	0.89	3.27
(1.152)	0.39	0.76	−24.53	−23.81	65.10	16.76	0.03	0.38	3.25
N1−H1	0.79	0.29	−20.21	−19.39	31.01	−8.59	0.04	0.65	1.64
(1.08)	0.81	0.27	−23.57	−23.16	14.55	−32.19	0.02	1.62	1.91
RCP[f]			−0.67	1.30	3.32	3.95			0.26
			−0.64	1.82	4.17	5.35			0.22

[a] BL is the bond length from experiment constrained in D_{2h}. [b] d_1 is the distance between BCP to the first atom in the bond. [c] d_2 is the distance between BCP to the second atom in the bond. [d] λ_1, λ_2, and λ_3 are Hessian eigenvalues at the critical point. λ_3 is along the bond path, and λ_1 and λ_2 are along the directions perpendicular to the bond path. [e] $\nabla^2\rho(\mathbf{r}_c) = \lambda_1 + \lambda_2 + \lambda_3$, Laplacian value at CP. [f] RCP is the ring critical point.

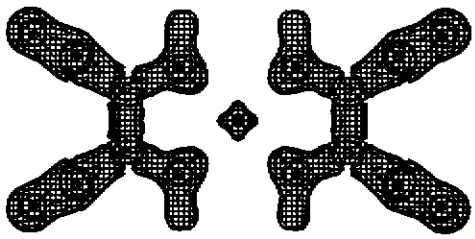

Figure 3. Isovalue surface of the zero Laplacian from the MO calculations.

in Figure 5a, b). This difference is even clearly displayed in the gradient vector maps shown in Figure 2. The relative distribution of the tightness and looseness of the gradient paths around Ni is quite different near the Ni nucleus (Figure 2a,b). Detailed properties at BCP are listed in Table 1. In general, the values from experiment and theory are in reasonably good agreement with each other. However, significant discrepancies are found in the $\nabla^2\rho(\mathbf{r}_c)$ values of the short triple C5−N5 and N−H bonds. This is due to the fact that the BCP are apparently very close to the electropositive centers C (0.39 Å) and H (0.29 Å). This will lead to the transfer of charge from the C or H to N, as indicated by Bader for C−O and C−S bonds.[2] Such polarization may yield the fact that the BCP lies just within the inner shell of charge depletion of C or H nucleus and thus gives a large positive λ_3 value. This is the case for C5−N5 triple bond, and the theoretical value of λ_3 is much larger than that of experimental one, so that the sign of the $\nabla^2\rho(\mathbf{r}_c)$ value, i.e., $\lambda_1 + \lambda_2 + \lambda_3$, is different between experiment and theory. Nevertheless, simply looking at λ_1 and λ_2 values, they are all large negative numbers indicating there is electron concentration along the bond. The different positions for the BCPs between experiment and theory are also shown in Table 1. In general, the difference in d_1 and d_2 is larger from MO calculation than that from experiment, especially for the bond with polar electron density distribution. The strong effect of such difference on the λ_3 value is quite pronounced. From the table, it is apparent that all bonds in the ligand are shared interactions. However the bond between Ni and nitrogen atom is more like a closed shell interaction with λ_1/λ_3 much less than 1, a positive $\nabla^2\rho(\mathbf{r}_c)$ value, and a small value of $\rho(\mathbf{r}_c)$. This is quite consistent with our earlier NBO analysis,[1] defining it as mainly a "dative" or "coordinated" bond with a small percentage of covalent character. A recent work[14] points out that a positive Laplacian value at BCP does not necessarily indicate a closed-shell, noncovalent interaction, especially when the charge distribution is diffuse. The $\rho(\mathbf{r}_c)$ value is often recognized as a number highly correlated with the bond order. Sure enough, the C5−N5 triple bond has the highest $\rho(\mathbf{r}_c)$ value of 3.27. The delocalized C−C, C−N bonds have the values of 2.0−2.4. The

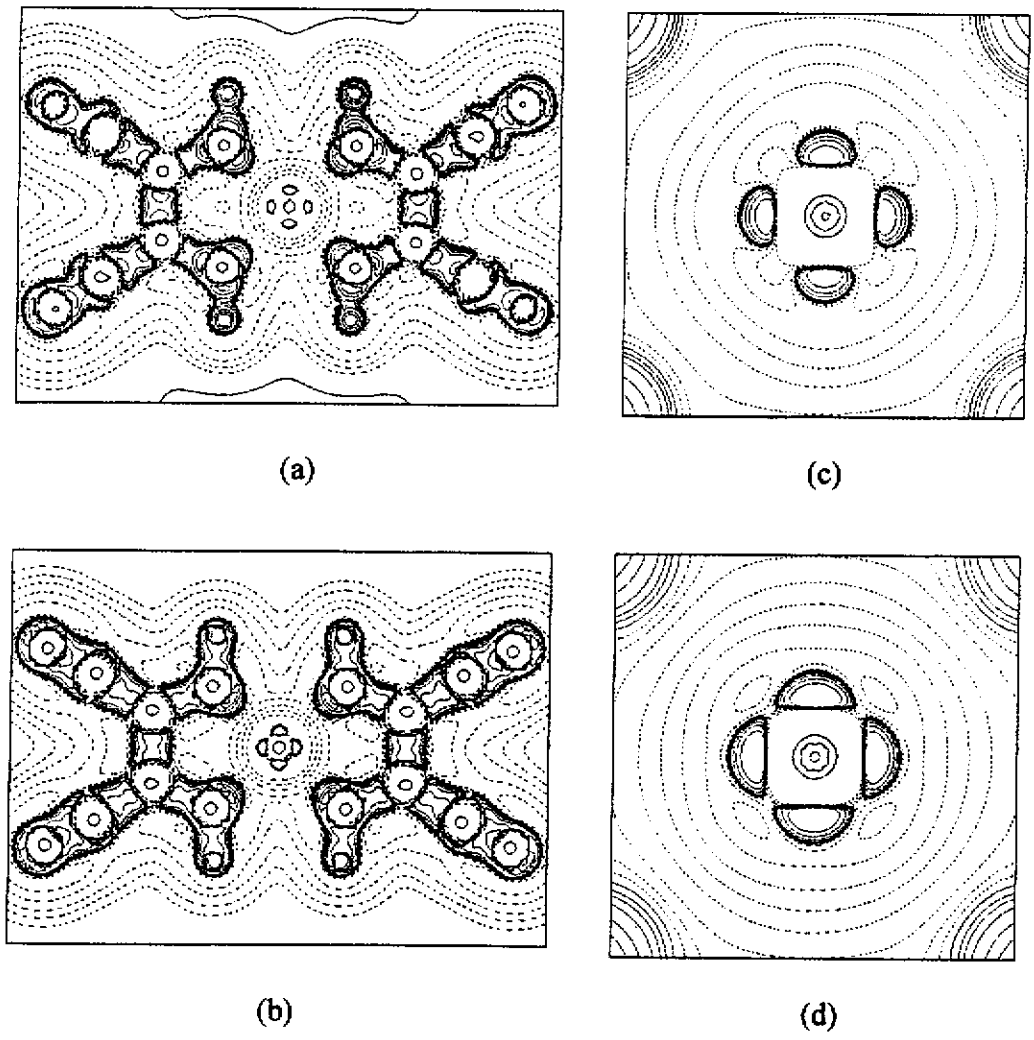

Figure 4. Negative Laplacian at the molecular plane (a, b) and the enlarged plot around Ni (c, d),where (a) and (c) are from experiment and (b) and (d) are from calculation. Contours are $(2^i \times 10^j\ e\text{Å}^{-5}, (i = 1, 2, 3)$, where $j = -1, 0, 1$ for (a, b) and $j = 0, 1, 2$ for (c, d). The solid red line means positive, the broken blue line negative, and the green line zero values.

N−H bond has a value of 1.6 e Å^{-3}, and Ni−N, 0.94 e Å^{-3}. The π-bond character is also indicated in the bond ellipticity, ϵ ($\lambda_1/\lambda_2 - 1$) value; for example, the N−H single bond and C5−N5 triple bond are essentially cylindrically symmetric bonds, so the ϵ value is very small (<0.05). In contrast, the ϵ values of the ring C−C and C−N bond are greater than 0.2, which strongly supports a π bond character perpendicular to the molecular plane.

Laplacian of the Electron Density

The zero isovalue envelope surface of the Laplacian, $\nabla^2\rho$, obtained from the calculation is displayed in Figure 3. This surface separates the valence shell charge concentration (VSCC $\nabla^2\rho < 0$) from the region of charge depletion ($\nabla^2\rho > 0$). This surface encompasses the VSCC of each nucleus, (3, −3) CP, and is continuous to the VSCC on the bonded atoms. The Ni−N bonds, in contrary, show little charge concentration along the bond. To further characterize the local charge concentration and the local charge depletion in the molecule, the negative Laplacian of the molecule is depicted in Figure 4. For the ring C, N atoms of the ligand, each displays three local concentrations of electron density around the nucleus; this signifies an sp^2-type of valence shell. The exocyclic C and N nuclei show two local concentrations in a linear fashion expected from a sp-hybrid valence shell. The most exciting feature of the negative Laplacian distribution is around the transition metal Ni nucleus. If one looks at the enlarged map of Ni (Figure 4b,d), it is clearly shown that the local concentrations of electron density are at the bisection of two ∠N1−Ni−N2 angles and the charge depletions are along the Ni−N directions. This is exactly in accord with the form predicted by the crystal field theory, where electron density in the valence shell is depleted in d_σ (along Ni−N) and is accumulated along the d_π direction (bisection of ∠N1−Ni−N2). Again the agreement between the experiment (Figure 4a,b) and the theory (Figure 4c,d) is satisfactory. Such a feature of the asphericity in electron density around Ni was also found in the deformation density distribution.[1]

Atom Domain

According to Bader et al.,[2] every atom, whether free or bound, is assigned to have its own unique space. The space of a bound atom is often delimited by curved surfaces because of its interaction with neighbors. This space is transferable to an atom with a similar coordination environment. The collection of atomic domains yields an atlas for the molecule. The atom domain can be identified as a zero flux surface around each atom. Such partitions projected on the molecular plane together with the total electron density and bond paths are illustrated in Figure 5 both from experiment (Figure 5a) and from MO calculation (Figure 5b). Again the comparison between experiment and theory is good with the shape and the areas of the domains are nearly superimposable on each other.

Fermi-Hole Function and Electron Delocalization

A correlation function is defined by McWeeny[7,23] to attribute the relationship between the Fermi correlation and the spatial localization of electrons. The Fermi-hole function is a distribution function for an electron of a given spin that determines the decrease in the probability of finding another electron with the same spin relative to a fixed position of the electron in question (reference electron). Thus the Fermi hole describes the region where the charge of the reference electron is spread out in space.

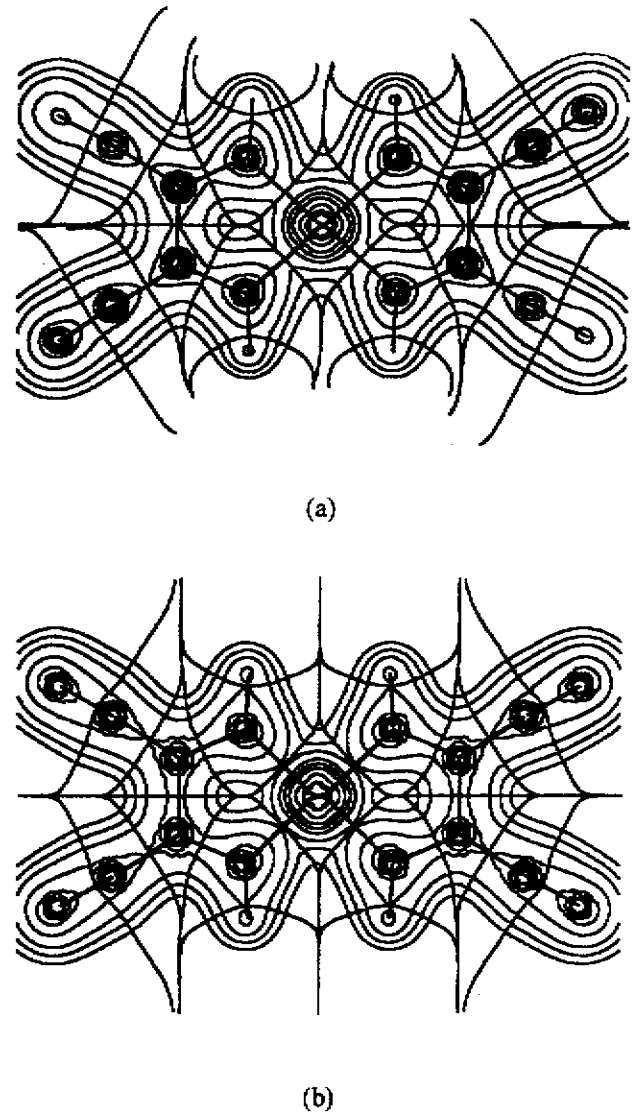

(a)

(b)

Figure 5. Total electron density (red), $\rho(\mathbf{r})$, bond path (black), and atom domain separated with green lines from (a) experiment and (b) calculation. Contours of $\rho(\mathbf{r})$ are as in Figure 4a.

This function can only be derived by MO calculation. Accordingly, the Fermi hole can provide information about the localization or delocalization of the electron density. Recently such delocalization properties of the Fermi-hole density have been utilized to quantitatively assess the delocalization of electrons in some aliphatic and aromatic compounds.[38] Here we try to use the same idea to analyze the π-delocalization of the ligand. On the basis of the bond distances of the molecule,[1] the ligand, disn, is best described as a totally π-electron delocalized monoanionic form.[39,40] Fermi-hole densities with reference electron located at 0.7 au above the molecular plane (π-density) on various atomic sites of the ligand are displayed in Figure 6a−d. Apparently π-density at the nitrilo C and N atoms (Figure 6b,d) is essentially distributed between the neighboring atoms; that is, the bond is a localized π-bond. In contrast, when the reference electron is placed on any ring C or N atom, the Fermi-hole density is spreading out to all eight ring atoms. (Figure 6a,c) This result reemphasizes the fact that the ligand is a totally π-electron delocalized monoanionic form, which is consistent with the result from earlier NBO analysis.[1] Figure 6e indicates the bond interaction between ring N and Ni at the molecular plane (σ-density); this manifests that although the Ni−N bond is largely dative indicated from the positive

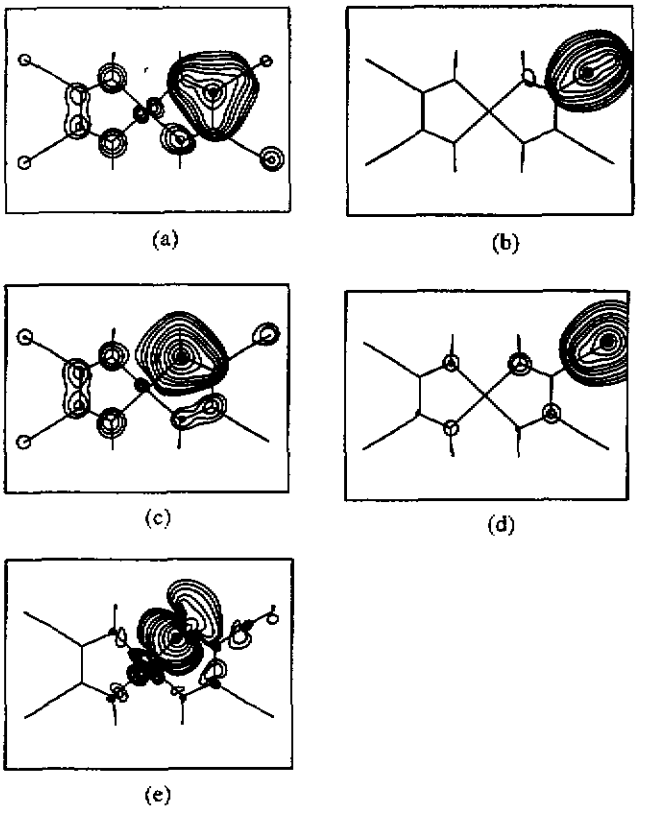

Figure 6. Fermi-hole functions at the plane of 0.7 au above the molecular plane with the reference electron (●) placed on this plane at (a) N1, (b) Cl, (c) C5, (d) N5, and (e) Fermi−hole functions at the molecular plane with reference electron situated at N1.

$\nabla^2\rho(\mathbf{r}_c)$, there is still some covalent character along this bond, again consistent with the earlier NBO results.[1]

Molecular Electrostatic Potential

MEP is often used as a tool to correlate structure and reactivity of a molecule. However it is only applied in the case where the classical Coulombic interaction is dominant, such as in protonation processes and in hydration phenomena. In general, the MEP has long been used as a reactivity index of long-range chemical interactions.[27-33,42] Many studies of MEP are based on molecular orbital calculations. It would be very useful to be able to obtain accurate values of $\rho(\mathbf{r})$ and electrostatic potential, $V(\mathbf{r})$, directly from experiment[43,44] to compare with the quantum mechanical calculation or to test the accuracy both on experiment and on theory. Here we present in Figure 7 the MEP of the molecule both from the multipole model and from the HF calculation. It is pleasing to see that the agreement between them is very good with the minimum potential of -0.1 e Å^{-1} (33.2 kcal/mol) located at the nitrilo-N atom. The intermolecular interaction cannot be addressed properly here since the electron density is calculated only for one molecule both in experiment and in theory, though the multipole coefficients are indeed affected somewhat by the crystal packing force, if there is any. For this molecular crystal, such crystal packing force is assumed to be small. However, electrostatic potential (EP) based on the calculated structure F_c model[41] can be used for understanding the intermolecular interactions such as a hydrogen bond.[10]

Conclusion

The combined experimental and molecular orbital calculated electron densities accompanied by their topological analyses are used to give a quantitative characterization of bonding. The Ni−N bond is classified as mainly a closed-shell interaction with some covalent character while all the intraligand bonds are shared interactions or covalent bonds. The π-delocalization on the ligand is clearly indicated by bond critical point properties and by the Fermi-hole function. Atom domains in the molecule are illustrated to be correlated with the atomic hybrid types in their valence shells. For all these properties, comparison is made between experiment and theory.

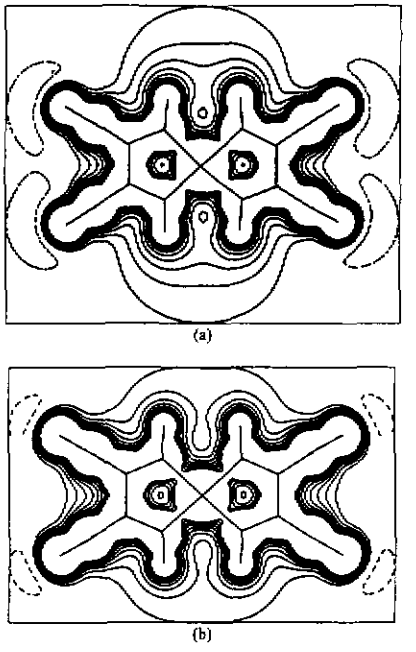

Figure 7. Molecular electrostatic potential calculated from (a) experiment and (b) calculation, where contour intervals are in 0.1 e Å^{-1} (33.2 kcal/mol) units.

Acknowledgment. Financial support of this work from National Science Council of ROC is appreciated. Thanks are due to the National Center for High Performance Computing for providing computing facilities and software packages. Special thanks to Professor R. F. W. Bader and Professor M. Souhassou for their kindly supplying a copy of the AIMPAC and PROP programs, respectively.

References and Notes

(1) Lee, C. S.; Hwang, T. S.; Wang, Y.; Peng, S. M.; Hwang, C. S. *J. Phys. Chem.* **1996**, *100*, 2934−2941.

(2) Bader, R. F. W. *Atom in Molecules-A Quantum Theory*; Clarendon Press: Oxford, U.K., 1990.

(3) Schwarz, W. H. E.; Ruedenberg, K.; Mensching, L. *J. Am. Chem. Soc.* **1989**, *111*, 6926−6933.

(4) Kunze, K. L.; Hall, M. B. *J. Am. Chem. Soc.* **1986**, *108*, 5122.

(5) Dunitz, J. D.; Seiler, P. *J. Am. Chem. Soc.* **1983**, *105*, 7056.

(6) Spasojevicdebire, A.; Dao, N. Q.; Strich, A.; Thieffry, C.; Benard, M. *Inorg. Chem.* **1990**, *29*, 4908−4915.

(7) Bader, R. F. W. *Chem. Rev.* **1991**, *91*, 893.

(8) MacDougall, P. J.; Hall, M. B.; Bader, R. F. W.; Cheeseman, J. R. *Can. J. Chem.* **1990**, *67*, 1842.

(9) Sierraalta, A.; Ruette, F. *Int. Quantum Chem.* **1996**, *60*, 1015−1026.

(10) Flensburg, C.; Larsen, S.; Stewart, R. F. *J. Phys. Chem.* **1995**, *99*, 10130−10141.

(11) Koritsanszky, T.; Buschmann, J.; Luger, P. *J. Phys. Chem.* **1996**, *100*, 10547−10553.

(12) Yufit, D. S.; Mallinson, P. R.; Muir, K. W.; Kozhushkov, S. I.; Demeijere, A. *Acta Crystallogr.* **1996**, *B52*, 668−676.

(13) Howard, S. T.; Hursthouse, M. B.; Lehmann, C. W.; Poyner, E. A. *Acta Crystallogr.* **1995**, *B51*, 328−337.

(14) Smith, G. T.; Mallinson, P. R.; Frampton, C. S.; Farrugia, L. J.; Peacock, R. D.; Howard, J. A. K. *J. Am. Chem. Soc.* **1997**, *119*, 5028−5034.
(15) Stewart, R. F. *J. Chem. Phys.* **1969**, *51*, 4569−4577.
(16) Hansen, N. K.; Coppens, P. *Acta Crystallogr.* **1978**, *A34*, 909.
(17) Hirshfeld, F. L. *Isr. J. Chem.* **1977**, *16*, 226.
(18) Silvi, B.; Savin, A. *Nature* **1994**, *371*, 683−686.
(19) Bader, R. F. W.; Johnson, S.; Tang, T.-H.; Popelier, P. L. A. *J. Phys. Chem.* **1996**, *100*, 15398−15415.
(20) Bader, R. F. W.; Gillespie, R. J.; MacDougall, P. J. *J. Am. Chem. Soc.* **1988**, *110*, 7329.
(21) Gillespie, R. J. *Can. J. Chem.* **1992**, *70*, 742.
(22) Bader, R. F. W.; Popelier, P. L. A.; Chang, C. J. *J. Mol. Struct. (THEOCHEM)* **1992**, *255*, 145.
(23) McWeeny, R. *Rev. Mod. Phys.* **1960**, *32*, 335.
(24) Bader, R. F. W.; Stephens, M. E. *Chem. Phys. Lett.* **1974**, *26*, 445.
(25) Bader, R. F. W.; Stephens, M. E. *J. Am. Chem. Soc.* **1975**, *97*, 7391.
(26) Politzer, P.; Truhlar, D. G. *Chemical Applications of Atomic and Molecular Electrostatic Potential*; Plenum Press: New York, 1981.
(27) Lin, K. J.; Cheng, M. C.; Wang, Y. *J. Phys. Chem.* **1994**, *98*, 11685−11693.
(28) Lugue, F. J.; Orozco, M.; Illas, F.; Rubio, J. *J. Am. Chem. Soc.* **1991**, *113*, 5203.
(29) Faerman, C. H.; Price, S. L. *J. Am. Chem. Soc.* **1990**, *112*, 4915.
(30) Stone, A. *J. Chem. Phys. Lett.* **1981**, *83*, 233.
(31) Stone, A. J.; Alderton, M. *Mol. Phys.* **1985**, *56*, 1047.
(32) Murray, J. S.; Lane, P.; Politzer, P. *J. Mol. Struct.(THEOCHEM)* **1990**, *209*, 163.
(33) Murray, J.; Redfern, P. C.; Lane, P.; Politzer, P. *J. Mol. Struct-.(THEOCHEM)* **1990**, *207*, 177.
(34) Wachter, A. J. H. *J. Chem. Phys.* **1907**, *52*, 1033. (b) Gianolo, L.; Pavani, R.; Clementi, E. G. *Chim. Ital.* **1978**, *108*, 181.
(35) Frisch, M. J.; Trucks, G. W.; Schlegel, H. B.; Gill, P. M. W.; Johnson, B. G.; Robb, M. A.; Cheeseman, J. R.; Keith, T. A.; Petersson, G. A.; Montgomery, J. A.; Raghavachari, K.; Al-Laham, M. A.; Zakrzewski, V. G.; Martin, R. L.; Ortiz, J. V.; Foresman, J. B.; Cioslowski, J.; Stefanov, B. B.; Nanayakkara, A.; Challacombe, M.; Gomperts, R.; Fox, D. J.; Binkley, J. S.; Defrees, D. J.; Baker, J.; Stewart, J. P.; Head-Gordon, M.; Conzalez, C.; Pople, J. A. *Gaussian 94*, revision A.1; Gaussian Inc.: Pittsburgh, PA, 1995.
(36) PROP program: A program developed by M. Souhassou, N. K. Hansen, E. Stevens, B. Craven, N. Bouhmeida, N. Ghermani, and C. Lecomte.
(37) *AIMPAC: a set of programs for the Theory of Atom in Molecules*; Bader, R. F. W., and co-workers, Eds.; McMaster University: Hamilton, Ontario, Canada.
(38) Bader, R. F. W.; Streitwieser, A.; Neuhaus, A.; Laidig, K. E.; Speers, P. *J. Am. Chem. Soc.* **1996**, *118*, 4959.
(39) Peng, S. M.; Simon, A.; Wang, Y.; Liaw, D. S. *Angew. Chem., Int. Ed. Engl.* **1985**, *24*, 210.
(40) Adams, D. M.; Dei, A.; Rheingold, A. L.; Hendrickson, D. N. *J. Am. Chem. Soc.* **1993**, *115*, 8221.
(41) Stewart, R. F. *God. Jugosl. Gent. Kristalogr.* **1982**, *17*, 1.
(42) Fan, J. M.; Wang, Y.; Ueng, C. H. *J. Phys. Chem.* **1993**, *97*, 8193−8199.
(43) Espinosa, E.; Lecomte C.; Ghermani, N. E.; Devemy, J.; Rohmer, M. M.; Benard, M.; Molins, E. *J. Am. Chem. Soc.* **1996**, *118*, 2501−2502.
(44) Su, Z. W.; Coppens, P. *Acta Crystallogr.* **1992**, *A48*, 188.

Bond Characterization of Metal Squarate Complexes [$M^{II}(C_4O_4)(H_2O)_4$; M = Fe, Co, Ni, Zn]

Chi-Rung Lee, Chih-Chieh Wang, Ko-Chun Chen, Gene-Hsiang Lee, and Yu Wang

Department of Chemistry, National Taiwan University, Taipei, Taiwan, ROC, and Instrumentation Center, National Taiwan University, Taipei, Taiwan, ROC

The Journal of Physical Chemistry A®

Reprinted from
Volume 103, Number 1, Pages 156–165

Bond Characterization of Metal Squarate Complexes [$M^{II}(C_4O_4)(H_2O)_4$; M = Fe, Co, Ni, Zn]

Chi-Rung Lee,[†] Chih-Chieh Wang,[†] Ko-Chun Chen,[‡] Gene-Hsiang Lee,[‡] and Yu Wang*[,†,‡]

Department of Chemistry, National Taiwan University, Taipei, Taiwan, ROC, and Instrumentation Center, National Taiwan University, Taipei, Taiwan, ROC

Received: June 19, 1998; In Final Form: October 1, 1998

Tetraaqua metal squarate complexes, $M(C_4O_4)(H_2O)_4$, (M = Fe, Co, Ni, Zn), are known to have a polymeric chain structure with $C_4O_4^{2-}$ as a bridge (μ-2) ligand between two metal ions in the trans position. Each metal ion is bonded to two $C_4O_4^{2-}$ and four water molecules. They are all isostructural with space group *C*2/*c*. A complete Ewald sphere of data is measured at 120 K up to 2θ of 100−120° using Mo Kα radiation for each complex. Such carefully measured intensities are used to investigate the detailed electron density distribution in order to understand the chemical bonding and the d-orbital splitting of the metal ions subjected in such a ligand field. Results on the electron density distribution will be presented in the form of deformation density and of Laplacian maps. Deformation density will be presented in terms of experimental $\Delta\rho_{x-x}$, $\Delta\rho_{m-s}$ (multipole model), and of theoretical $\Delta\rho$ derived from the HF and DFT calculations. The interesting bent bond feature on the four-membered ring ligand $C_4O_4^{2-}$ is explicitly demonstrated by the deformation density distribution and the bond path of the cyclic carbon−carbon bond. The asphericity in electron density distribution around the metal ion is also clearly illustrated in these compounds both in the deformation density and in Laplacian of the density. The comparison on the series of 3d-transition metal complexes will be made not only by the deformation density distribution and by the Laplacian of the density but also by the d-orbital population and by the associated topological properties at the bond critical point. The total number of d-electrons from the experiments are 6.05, 6.88, 7.89, and 8.40, respectively, for Fe(II), Co(II), Ni(II), and Zn(II) ions in these compounds. A comparison between experiment and theory is made for the Ni complex.

Introduction

The electron density distribution of transition metal complexes has been investigated extensively using the single-crystal X-ray diffraction method during the last decade.[1−19] Systematic studies on the 3d-transition metal complexes are made for the purpose of understanding the trend of electronic structure around the metal ion. The electronic structures of hexaaquametal(II) ions[1−13] are of archetypal importance in understanding metal−ligand (oxygen) bonds. Ammonium metal Tutton salts, $(NH_4)_2[M^{II}(H_2O)_6](SO_4)_2$ (M^{II} = V,[15,20] Cr,[3] Mn,[14,21] Fe,[5,16,20] Co,[20] Ni,[1,22] Cu,[2,4,23,24] Zn[25]), have been studied by X-ray[1−6] and polarized neutron diffraction,[11−13] where detailed charge[1−6] and spin densities[11−13] are given. The extent of σ and π metal−water bonding, electron correlation effects, and spin−orbit coupling effects are also discussed.[1−6,11−13] The Jahn−Teller distortions are demonstrated in Cr(II)[3] and Cu(II)[2,4] complexes in comparison with the nondistorted Fe(II)[5] complex. These series of studies give a good example that by systematically varying the central 3d-transition metal in an isostructural environment, detailed information can be provided not only on the metal ligand bond but also on the crystal field effect exerted on the metal ions.

The squarate dianion, $C_4O_4^{2-}$, is a simple, interesting cyclic compound with aromaticity.[26−30] With four C−O partial double bonds, it is a potential bridging ligand with possible μ-2[26,27] to μ-4[28,30] bridging ligands between the metals. The intermolecular H-bond does play an important role in such complexes[26−32] as well as in the simple squaric acid.[33−39] There are symmetric and asymmetric H-bonds in the solid.[26−39] Detailed structural relationships for various metal squarate complexes are discussed in a recent report.[32] Three types of metal squarate complexes are known for the 3d-transition metals. They are $M(C_4O_4)(H_2O)_4$ (M = Mn, Fe, Co, Ni, Cu, Zn),[26,27] $M(HC_4O_4)_2(H_2O)_4$ (M = Mn, Fe),[31,32] and $M(C_4O_4)(H_2O)_2$ (M = Mn, Fe, Co, Ni, Cu, Zn).[28−30] Recently, additional types have been found in $Co_3(\mu_2\text{-}OH)_2(C_4O_4)_2(H_2O)_3$,[40] $[V(OH)(C_4O_4)(H_2O)]_2$,[41] and $[V(OH)(C_4O_4)]_2\cdot 4H_2O$.[41] For $M(C_4O_4)(H_2O)_4$ complexes, they are of the linear chain type, where each $C_4O_4^{2-}$ is coordinated with two metals in the trans position and each metal is again linked by two $C_4O_4^{2-}$. In the case of Mn, Fe, Co, Ni, and Zn,[26,27] they are isostructural. These complexes, in general, give good quality of diffraction data. Accurate charge density studies on a series of these transition metal complexes are undertaken in order to further our understanding on the metal−aqua and metal−squarate bonding as well as the crystal field effect on the d-orbital populations. It will provide a valuable comparison with those paralleling structures found in the metal Tutton salts[4−6] since both types of complexes have six M−O bonds at a roughly octahedral symmetry.

The bonding in the planar four-membered ring ligand with aromaticity is also an interesting feature to look into via the electron density distribution. Such a distribution will be compared with our recent work on a related ammonium salt $(Me_2NH_2)[H_3(C_4O_4)_2]$.[39]

* To whom all correspondence should be addressed.
† Department of Chemistry.
‡ Instrumentation Center.

10.1021/jp982696c CCC: $18.00
Published on Web 12/17/1998

TABLE 1: Crystal Data of $[M(C_4O_4)(H_2O)_4]$ (M = Fe, Co, Ni, Zn)

		Crystal Data		
chemical formula	$Fe(C_4O_4)(H_2O)_4$	$Co(C_4O_4)(H_2O)_4$	$Ni(C_4O_4)(H_2O)_4$	$Zn(C_4O_4)(H_2O)_4$
chemical formula weight	239.95	243.03	242.81	249.48
cell setting	monoclinic	monoclinic	monoclinic	monoclinic
space group	*C2/c*	*C2/c*	*C2/c*	*C2/c*
a, Å	9.032(1)	8.965(1)	8.913(3)	8.986(2)
b, Å	13.381(1)	13. 376(3)	13.232 (4)	13.333(2)
c, Å	6.734(2)	6.680(1)	6.654 (3)	6.694(3)
β, deg	99.19(2)	99.67 (1)	99.71 (3)	99.67(2)
V, $Å^{-3}$	803.0(3)	789.7(3)	773.4 (5)	790.6(3)
Z	4	4	4	4
D_x, Mg m^{-3}	1.984	2.044	2.085	2.096
radiation type	Mo Kα	Mo Kα	Mo Kα	Mo Kα
wavelength, Å	0.7107	0.7107	0.7107	0.7107
no. of reflns for cell parameters	25	25	25	25
2θ range for unit cell detn, deg	89−108	75−98	71−96	40−90
μ, cm^{-1}	18.9	21.8	25.3	31.9
temperature, K	120	120	120	120
crystal size, mm	0.15 × 0.15 × 0.3	0.36 × 0.20 × 0.20	0.25 × 0.15 × 0.15	0.33 × 0.2 × 0.25
		Data Collection and Reduction		
diffractometer	Nonius CAD4	Nonius CAD4	Nonius CAD4	Nonius CAD4
data collection control	$\theta/2\theta$ scan mode	$\theta/2\theta$ scan mode	$\theta/2\theta$ scan mode	$\theta/2\theta$ scan mode
2θ scan width, deg	$2(0.65 + 0.35 \tan\theta)$	$2(0.70 + 0.35 \tan\theta)$	$2(0.70 + 0.35 \tan\theta)$	$2(0.70 + 0.35 \tan\theta$
speed, deg min^{-1}	2.06, 8.14	2.06, 8.14	2.06, 8.14	2.06, 8.14
absorption correction	Gaussian integration	Gaussian integration	Gaussian integration	Gaussian integration
T_{min}	0.660	0.550	0.564	0.434
T_{max}	0.807	0.693	0.716	0.584
no. of measured reflns	22539	17952	19497	19653
no. of unique reflns	6082	5633	4054	4140
no. of observed reflns	4642	4071	3186	3237
criterion for observed reflns	$I > 2\sigma(I)$	$I > 2\sigma(I)$	$I > 2\sigma(I)$	$I > 2\sigma(I)$
R_{int}[a]	0.023	0.021	0.027	0.023
$2\theta_{max}$, deg	120	110	100	100
range of *h*, *k*, *l*	$-21 \rightarrow h \rightarrow 21$	$-20 \rightarrow h \rightarrow 20$	$-19 \rightarrow h \rightarrow 18$	$-19 \rightarrow h \rightarrow 19$
	$0 \rightarrow k \rightarrow 32$	$0 \rightarrow k \rightarrow 30$	$0 \rightarrow k \rightarrow 28$	$0 \rightarrow k \rightarrow 28$
	$0 \rightarrow l \rightarrow 16$	$0 \rightarrow l \rightarrow 15$	$0 \rightarrow l \rightarrow 14$	$0 \rightarrow l \rightarrow 14$
no. of standard reflns	3	3	3	3
frequency of standard reflns	once per hour	once per hour	once per hour	once per hour
		Refinement		
refinement on	*F*	*F*	*F*	*F*
R[a]	0.024	0.023	0.025	0.024
R_w[a]	0.024	0.026	0.025	0.024
S[a]	2.91	2.84	2.54	2.47
no. of reflns used in refinement	4642	4071	3186	4140
no. of parameters used	78	78	78	78
H-atom treatment	difference Fourier	difference Fourier	difference Fourier	difference Fourier
weighting scheme	$1/[\sigma^2(F_o) + 10^{-5}(F_o^2)]$	$1/[\sigma^2(F_o) + 10^{-5}(F_o^2)]$	$1/[\sigma^2(F_o) + 10^{-5}(F_o^2)]$	$1/[\sigma^2(F_o) + 10^{-5}(F_o^2)]$
$(\Delta/\sigma)_{max}$	0.0006	0.064	0.002	0.001
$\Delta\rho$ max, e $Å^{-3}$	0.92	0.95	1.29	0.79
$\Delta\rho$ min, e $Å^{-3}$	−1.03	−1.04	−0.98	−1.13
extinction method	secondary (Larson, 1970)[68]	secondary (Larson, 1970)[68]	secondary (Larson, 1970)[68]	secondary (Larson, 1970)[68]
extinction coefficient × 10^4	0.29(1)	0.125(9)	0.086(2)	0.202(9)
source of atomic scattering factors	*International Tables for X-ray Crystallography* (1974, Vol. IV)	*International Tables for X-ray Crystallography* (1974, Vol. IV)	*International Tables for X-ray Crystallography* (1974, Vol. IV)	*International Tables for X-ray Crystallography* (1974, Vol. IV)
computer program used	NRCVAX[40]	NRCVAX[40]	NRCVAX[40]	NRCVAX[40]

[a] $R = \sum|F_o - F_c|/\sum F_o$. $R_w = [\sum w|F_o - F_c|^2/\sum wF_o^2]^{1/2}$. $R_{int} = \sum|I_i - \langle I\rangle|/\sum I_i$. $S = [\sum w|F_o - F_c|^2/(NR - NV)]^{1/2}$; NR = no. of reflns, NV = no. of variables.

Experimental Section

Data Collection. Title compounds were synthesized according to the literature.[26,27] Suitable single crystals were obtained by direct crystallization out of aqueous solution. Each crystal was sealed in a glass capillary tube for data measurement. Intensity data were collected using Mo Kα radiation at 120 K with a liquid nitrogen device. A full sphere of reflections (four equivalent sets) was collected, and an absorption correction was applied before the averaging of equivalents based on the face measurements. The correctness of the absorption correction was checked against the experimental ψ curves for a few adequate reflections. The interset agreement was reasonable for all four complexes. Each reflection was then corrected for Lorentz and polarization effects. Three standard reflections were monitored every hour throughout the data measurement; the variation in intensity was all within ±5%. Other details are listed in Table 1.

Refinement. Conventional refinements are performed[42] with the full-matrix least-squares process both on full data and on high-order data ($\sin\theta/\lambda \geq 0.6$). The standard deviation of the average intensity is taken from the geometric mean of the equivalents. Results of the refinements are also given in Table 1.

Additional multipole refinements are performed with the MOLLY program,[43] where all the multipolar terms are expressed as a series expansion of the spherical harmonic functions. A multipole model is such that the atomic density is expressed as the sum of a core density, a spherical valence density, and a series of spherical harmonic terms with variable population, P_{lmp}, to describe the nonspherical feature of atomic electron density. The exact expression[43] is

$$\rho(\mathbf{r}) = \rho_{\text{core}} + \kappa^3 P_{\text{valence}} \rho_{\text{valence}}(\kappa r) + \sum_{n=0}^{l} R_{n,l}(r) \sum_{m=0,p=\pm}^{+l} P_{lmp} y_{lmp}(\mathbf{r}/r)$$

$$R_{n,l}(r) = N r^{n_l} \exp(-\zeta_l r)$$

where ρ_{core} and ρ_{valence} are spherical core and valence densities, respectively, κ is a radial contraction−expansion parameter, y_{lmp} is the spherical harmonic angular function in real form, $R_{n,l}$ is the radial part of the function where N is a normalization factor, and n_l and ζ_l are chosen for each l value.[43] P_{valence}, P_{lmp}, and κ are refinable parameters in addition to the atomic positional and vibrational parameters. Multipole terms up to hexadecapoles are included for metal ions; up to octapole are included for carbon and oxygen atoms, and up to dipole is for the hydrogen atom. The core and valence scattering factors for each atom are taken from *International Tables for X-ray Crystallography* (1974, Vol. IV). The core electron configurations are assumed to be He core for O and C; Ca core for all metal atoms.

Deformation Density Maps. Three types of experimental deformation density maps are presented in this work. The first one is the experimental $\Delta\rho_{x-x}$, where Fourier coefficients are obtained from the difference between F_o and F_c. F_c is calculated based on the parameters obtained from the high-order ($\sin\theta/\lambda \geq 0.6$) refinements. H atoms are moved along O−H vectors to make an O−H distance of 0.957 Å.[44] The second one is a model deformation density map $\Delta\rho_{m-a,\text{dynamic}}$, which is derived from a multipole model where Fourier coefficients are differences between two F_c values—one derived from a multipole model shown above, the other being the first two terms of the equation (spherical part) but with P_{valence} set to be neutral atom and κ reset to 1. The third one is a static model ($\Delta\rho_{m-a,\text{static}}$), which is obtained by plotting the density of each atom in direct space according to the equation given above, where no nuclear vibrations are taken into account. To check the correctness of the model deformation density, a residual density map $\Delta\rho_{\text{res}}$ is normally generated after the multipole refinement. This map is the difference density between the observed and the multipole model density. Deformation density distribution of $[Ni(C_4O_4)(H_2O)_4]$ is also investigated with theoretical calculations based on the ab initio method at the HF level and on the density functional (DFT) method, where the sum of atomic densities is subtracted from the molecular densities.

A critical point (CP), r_c, is a point in space that satisfies the condition of $\nabla\rho(r_c) = 0$. The Laplacian of the density can be obtained from the second derivative of the total electron density, $\nabla^2\rho$. When $\nabla^2\rho(r) < 0$, the electron density is locally concentrated at r; when $\nabla^2\rho(r) > 0$, the electron density is locally depleted at r. In addition, the Laplacian value and the eigenvalues of the Hessian matrix (λ_1, λ_2, λ_3) at the bond critical point (BCP) (3, −1) provide a description of the interaction between the bonded atoms as being either closed shell (ionic) or shared (covalent) interaction. The electron density at BCP, $\rho(r_c)$, is a direct indicator of the bond order. The Fermi hole function is an effective tool for recognizing the electron delocalization. Detailed definitions of all these topological properties are given elsewhere.[45,46]

TABLE 2: Non-Hydrogen Atomic Parameters and Equivalent Isotropic Thermal Parameters (Å²) with Esd's in Parentheses for the Structures of $M(C_4O_4)(H_2O)_4$ (M = Fe, Co, Ni, and Zn) at 120 K

		Fe	Co	Ni	Zn
M	x	0.75	0.75	0.75	0.75
	y	0.25	0.25	0.25	0.25
	z	0.0	0.0	0.0	0.0
	B_{iso}	0.529(2)	0.547(2)	0.499(3)	0.544(3)
O1	x	0.94979(4)	0.94684(4)	0.94523(5)	0.94649(6)
	y	0.16732(3)	0.16711(3)	0.16855(4)	0.16751(4)
	z	0.01120(7)	0.00858(7)	0.01018(9)	0.01044(9)
	B_{iso}	0.74(1)	0.77(1)	0.71(1)	0.73(1)
O2	x	0.25180(5)	0.24897(4)	0.25034(6)	0.24862(6)
	y	0.04002(3)	0.04179(3)	0.04283(4)	0.04224(4)
	z	0.00868(7)	0.00549(7)	0.00915(9)	0.00876(9)
	B_{iso}	0.80(1)	0.86(1)	0.80(1)	0.80(1)
O3	x	0.62708(5)	0.62555(5)	0.62480(6)	0.62414(6)
	y	0.12399(3)	0.13005(3)	0.13198(4)	0.12993(4)
	z	0.10222(7)	0.09708(8)	0.09314(9)	0.09568(9)
	B_{iso}	0.89(1)	0.93(1)	0.85(2)	0.87(2)
O4	x	0.81971(5)	0.81848(5)	0.81642(7)	0.81800(7)
	y	0.28939(4)	0.28743(4)	0.28608(5)	0.28735(5)
	z	0.30268(7)	0.30083(7)	0.29854(9)	0.30149(9)
	B_{iso}	1.04(1)	1.09(1)	1.04(2)	1.05(2)
C1	x	0.97512(5)	0.97360(5)	0.97274(7)	0.97350(7)
	y	0.07529(3)	0.07522(3)	0.07581(4)	0.07533(5)
	z	0.00463(8)	0.00381(8)	0.0043(1)	0.0045(1)
	B_{iso}	0.55(1)	0.58(1)	0.55(2)	0.55(2)
C2	x	0.11260(5)	0.11308(5)	0.11361(7)	0.11282(7)
	y	0.01755(3)	0.01834(3)	0.01890(5)	0.01859(5)
	z	0.00431(8)	0.00309(8)	0.0048(1)	0.0045(1)
	B_{iso}	0.56(1)	0.60(1)	0.57(2)	0.56(2)

TABLE 3: Selected Bond Distances (Å) and Angles (deg) of $M(C_4O_4)(H_2O)_4$ (M = Fe, Co, Ni, and Zn)

	Fe	Co	Ni	Zn
		Bond Distance (Å)		
M−O1(sq[a])	2.1076(4)	2.0767(4)	2.0381(7)	2.0714(6)
M−O3(wi[a])	2.1394(5)	2.1173(5)	2.0739(7)	2.1202(6)
M−O4(wo[a])	2.1021(7)	2.0619(6)	2.032(2)	2.069(1)
O1−C1	1.2546(6)	1.2538(6)	1.2532(8)	1.2546(8)
O2−C2	1.2569(7)	1.2555(6)	1.2547(9)	1.2561(8)
C1−C2	1.4627(7)	1.4645(6)	1.4636(9)	1.4628(9)
		Bond Angle (deg)		
O1−M−O3	85.329(2)	85.64(2)	84.76(3)	85.19(2)
O1−M−O4	91.448(2)	90.56(2)	90.83(3)	90.88(3)
O3−M−O4	91.817(2)	91.64(2)	91.86(3)	91.60(3)
M−O1−C1	132.37(3)	133.48(3)	133.40(4)	133.43(5)
O1−C1−C2	132.70(5)	132.57(4)	132.53(6)	132.60(6)
O2−C2−C1	136.06(4)	136.05(5)	135.85(6)	135.99(6)
C1−C2−C1	89.68(4)	89.73(4)	89.75(5)	89.71(5)
C2−C1−C2	90.32(4)	90.27(4)	90.25(5)	90.29(5)

[a] wi: in-plane M−O_w. wo: out of plane M−O_w. sq: squarate.

Computational Detail. The model compound chosen for the calculation in the theoretical comparison is $[Ni(HC_4O_4)_2(H_2O)_4]$. The geometry is taken from the diffraction data. To simplify the computation, the polymeric geometry is broken into a monomer by replacing two μ-C_4O_4 ligands with the HC_4O_4 moiety. The molecular symmetry is C_i with the center of inversion at the metal ion. For both HF and DFT calculations, the functions used for the Ni atom are (14, 9, 6)/[8, 4, 3] contractions: (626*1/5112/411),[47,48] where the (14s, 9p) primitive Gaussian functions are taken from Wachters[48] and the (6d) basis set is from Goddard.[47] The basis sets used for the O, C, and H atom are 6-31G**. The nonlocal correction applied in DFT is B3PW91.[49−52] All these calculations are made using the Gaussian94 program.[53] Total electron density from the

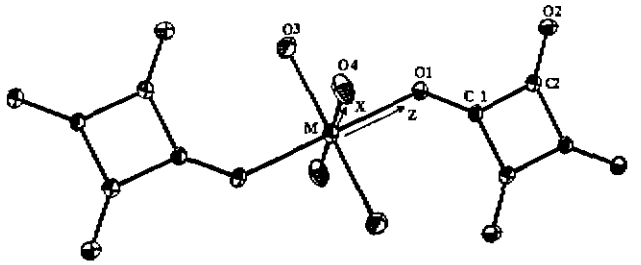

Figure 1. Molecular drawing with 50% probability in thermal ellipsoids at 120 K and choice of local Cartesian axis of metal centers.

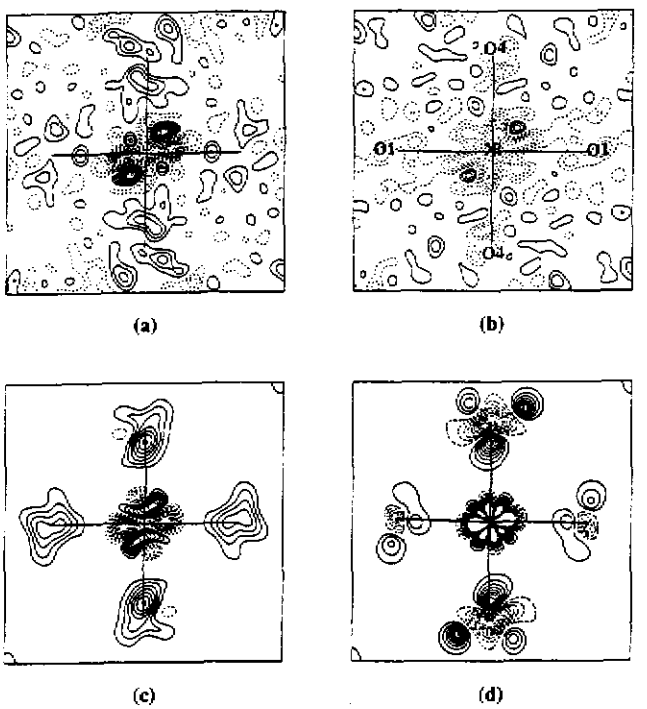

Figure 2. Deformation density maps of the O1−Ni−O4 plane, contours interval 0.1 e Å^{-3} within ±1.8 e Å^{-3}: (solid line) positive; (dashed line) negative; (a) $\Delta\rho_{x-x}$; (b) $\Delta\rho_{res}$; (c) $\Delta\rho_{m-a,dynamic}$; (d) $\Delta\rho_{m-a,static}$.

experiment is calculated on the basis of the multipole parameters.[43] Maps of Laplacian and the other topological properties are obtained using PROP[54] and AIMPAC[55] programs, respectively, for experiment and MO calculation.

Result and Discussion

Structure. The crystal structures at 120 K are the same as those at room temperature for all four complexes. They are isostructural in space group *C2/c*, and the metal is at the $\bar{1}$ site. The molecular structure and atomic coordinates obtained from full-matrix least-squares refinements are listed in Table 2. The metal ions are six-coordinated, with four aqueous (O_w) and two squarate (O_{sq}) oxygen atoms. Selected bond distances and bond angles are given in Table 3. The molecular structure, atomic labeling, and internal coordinates of the metal ion are shown in Figure 1. There are two M−O_w bonds, one (M−O3) is parallel to the C_4O_4 plane (in-plane), and the other (M−O4) is perpendicular to the C_4O_4 plane (out-of-plane). One finds that the in-plane M−O3 bond is much longer than the out-of-plane M−O4 bond and the M−O_{sq} bond. Therefore, the coordination of the metal ion in these complexes can be considered as a tetragonally distorted octahedron. However, the distortion is along one of the M−O_w (in-plane) directions. According to the literature,[27] this type of complex is more stable than the type

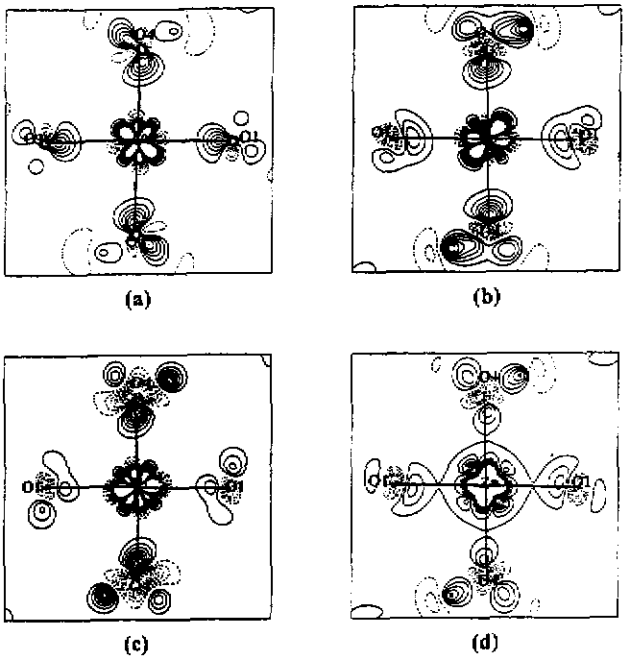

Figure 3. Deformation density maps of the O1−M−O4 and C_4O_4 ring plane: (a) Fe; (b) Co; (c) Ni; (d) Zn (in charge model). Contours are as in Figure 2.

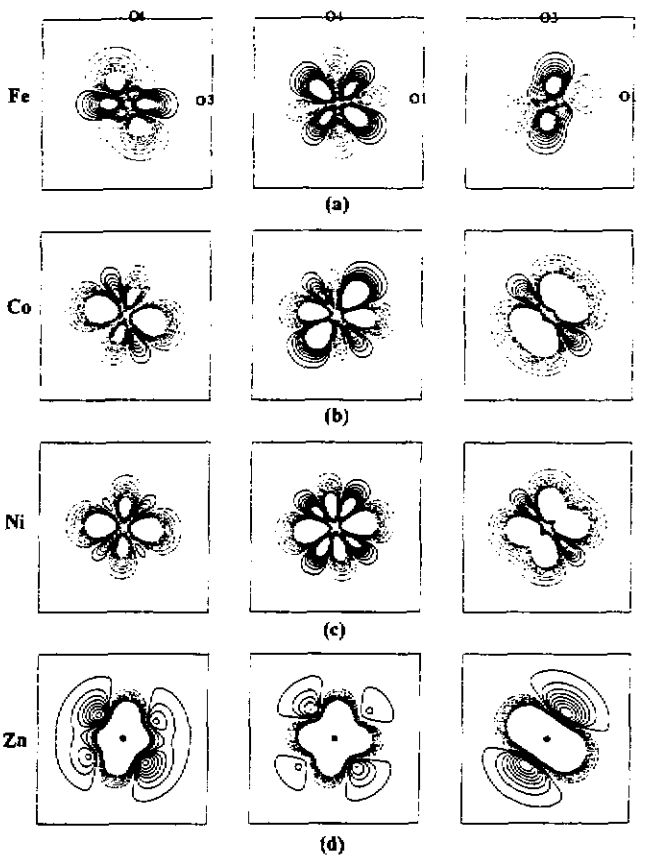

Figure 4. Deformation density maps of three unique planes (O3−M−O4, O1−M−O4, O1−M−O3) around the metal ion, contour interval 0.2 e Å^{-3} within ±1.8 e Å^{-3}: (a) Fe; (b) Co; (c) Ni; (d) Zn (in charge model), plot size 2 × 2 Å. The directions of O1, O3 and O4 are labeled in (a).

of $M(C_4O_4)(H_2O)_2$ at low temperature; presumably, the weaker in-plane M−O3 bond in the $M(C_4O_4)(H_2O)_4$ compounds is replaced by another M−O_{sq} bond and becomes $M(C_4O_4)(H_2O)_2$. According to bond distances of the M−O given in Table 3, the

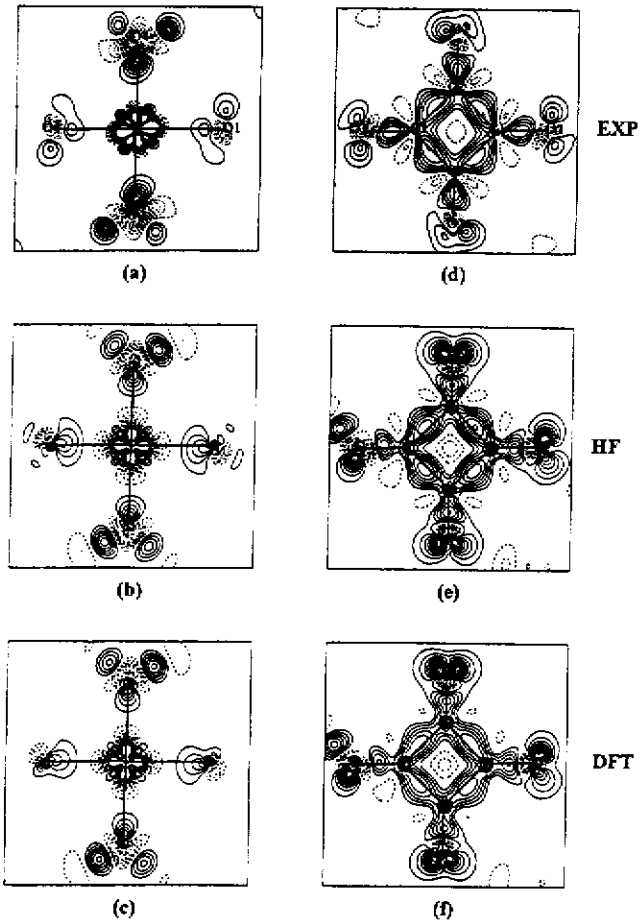

Figure 5. Deformation density maps of the O1−Ni−O4 plane (a−c) and C_4O_4 ring plane (d−f): (a) and (d) experiment; (b) and (e) HF; (c) and (f) DFT. Contours are as in Figure 2.

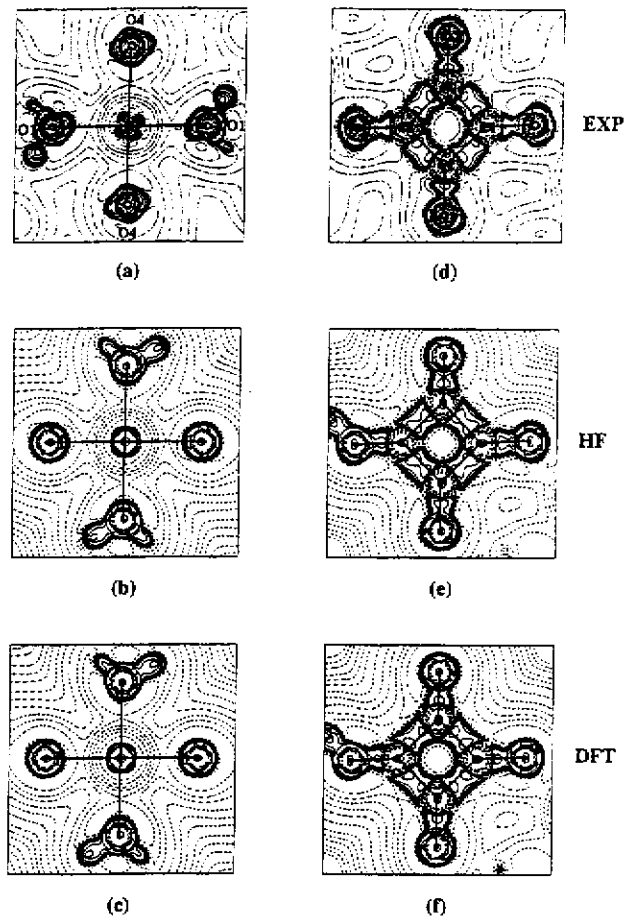

Figure 6. Negative Laplacian maps of the Ni complex: (solid line) positive; (dotted line) negative. The contour changes in steps of $(-1)^l 2^m 10^n$ (l = 1, 0; m = 1−3; n = −3 to +3). (a)−(d) are defined as in Figure 5.

TABLE 4: Agreement Indices of Various Refinements

	Fe	Co	Ni	Zn
NR[a]	4642	4071	3186	3237
		Conventional		
NV[b]	62	62	62	62
R	0.0262	0.0242	0.0260	0.0305
R_w	0.0316	0.0306	0.0294	0.0404
R_2[c]	0.0378	0.0385	0.0369	0.0440
R_{2w}[d]	0.0510	0.0482	0.0441	0.0601
S	3.858	3.355	2.921	4.209
		Monopole		
NV	76	76	76	76
R	0.0237	0.0226	0.0246	0.0235
R_w	0.0220	0.0246	0.0243	0.0221
R_2	0.0325	0.0344	0.0336	0.0352
R_{2w}	0.0347	0.0405	0.0365	0.0429
S	2.691	2.697	2.418	2.306
		Hexadecapole		
NV	192	192	192	192
R	0.0183	0.0170	0.0197	0.0189
R_w	0.0133	0.0165	0.0175	0.0156
R_2	0.0226	0.0231	0.0254	0.0267
R_{2w}	0.0194	0.0270	0.0270	0.0353
S	1.664	1.835	1.774	1.668

[a] NR: number of reflections. [b] NV: number of variables. [c] $R_2 = \sum|F_o^2 - F_c^2|/\sum F_o^2$. [d] $R_{2w} = (\sum w|F_o^2 - F_c^2|^2/\sum w|F_o|^4)^{1/2}$.

Fe−O bond length is the longest and the Ni−O is the shortest among the four complexes. This trend is exactly the same as those in Tutton salts[56] and other hexaaquametal ions.[6-8] The expected trend, predicted by ligand field theory (LFT) for these octahedral high-spin species, is such that the longest M−O distance should be found in manganese (d^5) and zinc (d^{10}) complexes and the shortest in vanadium (d^3) and nickel (d^8) complexes.[56] For the ligand part, the squarate dianion, $C_4O_4^{2-}$, is in a perfect D_{4h} symmetry with a C−O distance of 1.255 Å and a C−C distance of 1.463 Å. Weak H-bonds are found between water molecules and squarates of the neighboring chain.[32]

Deformation Density. Significant improvements on the agreement indices over the additional multipole terms are apparent in Table 4. This indicates that the multipole model does give a better representation of the electron density distribution than the spherical model does. For each complex, the deformation density distribution is calculated using $\Delta\rho_{x-x}$, $\Delta\rho_{m-a,dynamic}$, and $\Delta\rho_{m-a,static}$. The main features are quite similar between all these maps and the residual map $\Delta\rho_{res}$ is quite reasonable. One example for the Ni complex is displayed in Figure 2. For clarity, only the static maps are given for the other complexes. Static deformation density maps of a specific molecular plane, namely the plane passing through O1−M−O4, are depicted in Figure 3 for all the complexes. Four plots including three unique planes (O3−M−O4; O1−M−O4; O1−M−O3) around each metal ion are compared in Figure 4. The comparison of $\Delta\rho$ in the Ni complex between experiment and theory is shown in Figure 5, where one molecular plane (O1−M−O4) of the Ni complex and the plane of the squarate ligand are given. The maps of the ligand plane for all four complexes are nearly identical with the electron density accumulated at the bonding region of the C−O and C−C bonds and the lone

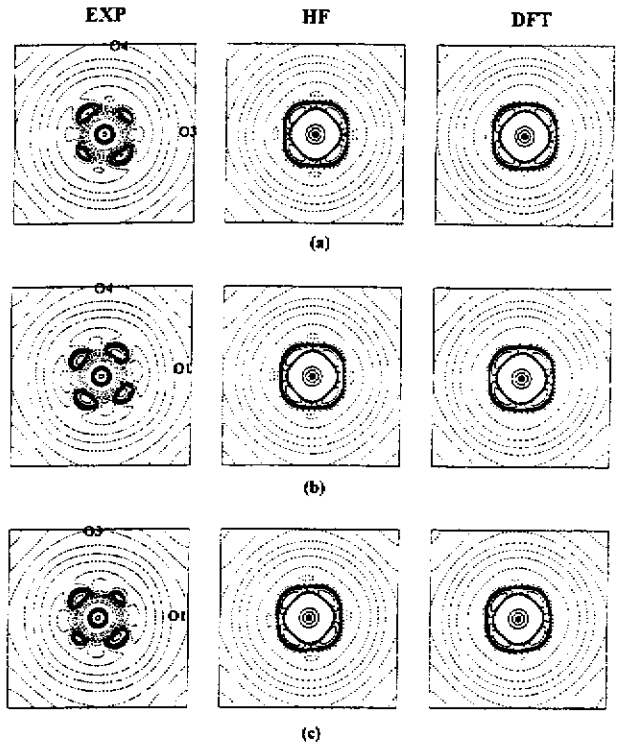

Figure 7. Negative Laplacian maps of the Ni complex obtained from experimental and theoretical results: (a) O3−M−O4; (b) O1−M−O4; (c) O1−M−O3 plane. Contours and plot size are as in Figure 6.

pair of the oxygen; one example is given in Figure 5d. It is also in good agreement with the corresponding map in $[H(HC_4O_4)_2^-]$,[39] although such an anion is actually in a dimeric form connected by a symmetric H-bond.[39] It is interesting to notice that the electron density distribution on the squarate plane clearly shows the ring strain of a four-membered ring. The analysis of $\Delta\rho$ (Figure 5d) provides a basis for a quantitative description of a "convex" bent bond expected for such a small ring compound.[39,57] The bonding electron density maximum is outward from the C−C interatomic axis (exocyclic) in the deformation density maps. It gives an angle of 110° between two bonding maxima at the carbon atom (C2) when the corresponding bond angle ∠C1−C2−C1′ is only ~90°. This is consistent with the four-centered σ bond being composed of four tangentially oriented (t-set) p-orbitals.[39,57] However, the bent bond feature is not so pronounced in the theoretically calculated ones shown in Figure 5e,f. Similar observation is found in $[H_3(C_4O_4)_2^-]$.[39] The lone pair electrons of oxygen atoms are quite observable in the O1−M−O4 planes (Figure 3). The σ donor character of the lone pair electrons at oxygen toward the metal ion is obvious. Actually, all three O−M−O planes give the same feature in deformation density maps. The asphericity in density around the metal ion is apparent (Figure 4) with electron depletion along d_σ and electron accumulation along the d_π direction, which is expected in terms of simple crystal field theory; the only exception is found along the Fe−O3 bond, which happens to be the longest M−O bond in all these compounds. The same feature is also noticed in (ND_4)-$[M(D_2O)_6](SO_4)_2$ along the Fe−O[5] and Cu−O bond.[4] However, such asymmetric density distribution is usually not found in the theoretically calculated maps. The asymmetric distribution near the metal center is nevertheless found quite often in other experimental maps,[1-6,18] specially where the concerning bond angles differed substantially, in this case 85° vs 91°. The discrepancies may due to the effect of the thermal parameters

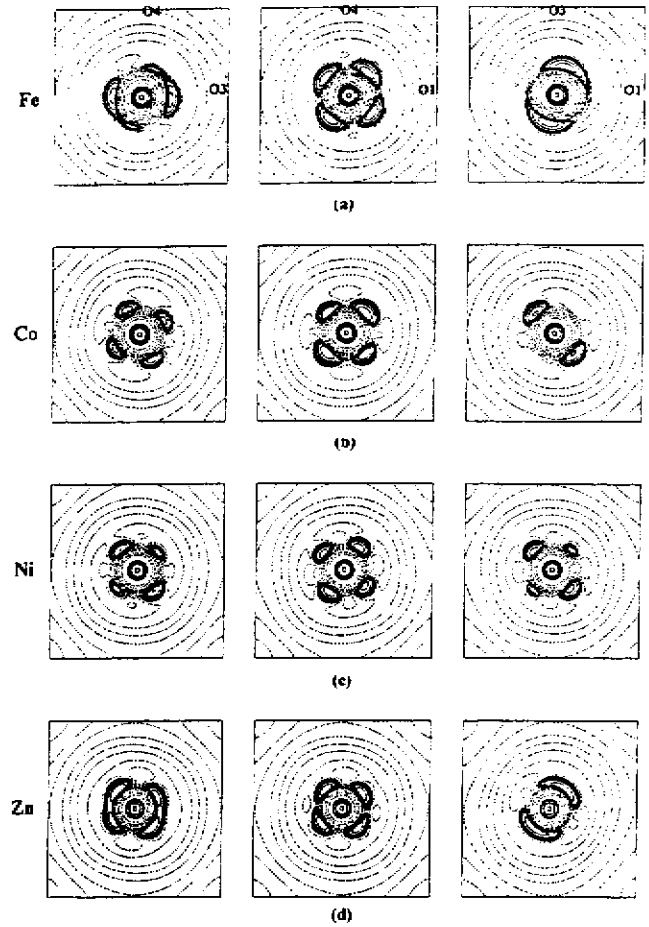

Figure 8. Negative Laplacian maps of the metal center from experimental results: (a) Fe; (b) Co; (c) Ni; (d) Zn. The directions of O1, O3, O4 are labeled in (a). Contours are defined as in Figure 6.

being not completely unbiased from the multipole coefficients even at 100 K.[58] The density distributions around the metal ions are very similar in shape; they correspond to high-spin configurations with t_{2g}-orbitals more populated than e_g-orbitals. Because of the high positive charge of the Zn atom (+1.97), the deformation density (Figure 4d) is derived by the subtraction of the charged atom instead of the neutral atom. The agreement between the experiment and theory on the Ni complex (Figure 5a−c) is reasonable. The agreement in the ligand part (Figure 5d−f) is very good.

Laplacian and Bond Critical Points. The local density accumulation and depletion, or the valence shell charge concentration (VSCC), can also be realized via a Laplacian of the density, $\nabla^2\rho$. The Laplacian of the total electron density derived from the experiment (multipole model) and from the HF and DFT calculations is presented in Figure 6 for the Ni complex. The charge concentration (CC) on C−C and C−O bonds and near the oxygen atom toward the nickel ion as well as the lone pair regions of carbonyl oxygen are clearly shown both in experiment and in theory. The local density concentration and depletion around the Ni atom is also clearly shown in Figure 7. The agreement between experiment and theory is adequate; however, the separation between local charge concentration and depletion is much clearer in the experimental ones than that in the theoretical ones. To compare the region near the metal center of all these complexes, the Laplacian of three unique planes around each metal ion is displayed in Figure 8. It is worth noticing that in these figures, the charge concentrations (CCs)

TABLE 5: Properties Associated with Bond Critical Points of $M(C_4O_4)(H_2O)_4$

bond	BL (Å)	metal center	d_1[a] (Å)	$\rho(r_c)$ (e Å^{-3})	$\nabla^2\rho(r_c)$[b] (e Å^{-5})	ϵ[c]	λ_1[d] (e Å^{-5})	λ_2[d] (e Å^{-5})	λ_3[d] (e Å^{-5})
M−O1	2.1076(4)	Fe	1.05	0.40	7.09	0.15			
	2.0767(4)	Co	1.03	0.46	7.36	0.01			
	2.0381(7)	Ni	1.02	0.47	8.07	0.31	−2.32	−1.77	12.16
		Ni[e]	0.97	0.35	10.15	0.06	−1.28	−1.21	12.64
		Ni[f]	0.98	0.38	8.94	0.05	−1.59	−1.52	12.06
	2.0714(6)	Zn	1.03	0.49	7.25	0.05			
M−O3	2.1394(5)	Fe	1.05	0.39	6.84	0.15			
	2.1173(5)	Co	1.06	0.41	6.42	0.10			
	2.0739(7)	Ni	1.03	0.44	7.16	0.18	−2.18	−1.84	11.18
		Ni[e]	0.98	0.32	9.14	0.06	−1.18	−1.11	11.43
		Ni[f]	0.99	0.35	8.15	0.05	−1.39	−1.32	10.86
	2.1202(6)	Zn	1.05	0.44	6.67	0.02			
O1−C1	1.2546(6)	Fe	0.75	2.93	−33.38	0.01			
	1.2538(6)	Co	0.77	2.42	−18.75	0.35			
	1.2532(8)	Ni	0.78	2.52	−21.42	0.20	−25.24	−20.97	24.79
		Ni[e]	0.85	2.23	0.39	0.04	−24.20	−23.18	47.77
		Ni[f]	0.84	2.19	1.54	0.02	−21.14	−20.76	43.44
	1.2546(8)	Zn	0.77	2.82	−29.05	0.16			
C1−C2	1.4627(7)	Fe	0.71	1.89	−13.93	0.12			
	1.4645(6)	Co	0.75	1.80	−12.57	0.25			
	1.4636(9)	Ni	0.75	1.84	−13.88	0.23	−14.13	−11.47	11.72
		Ni[e]	0.75	1.82	−22.53	0.14	−16.25	−14.23	7.96
		Ni[f]	0.75	1.72	−17.96	0.15	−14.56	−12.61	9.21
	1.4628(9)	Zn	0.72	1.84	−11.82	0.20			

[a] d_1 is the distance between BCP to the first atom in the bond. [b] $\nabla^2\rho(r_c) = \lambda_1 + \lambda_2 + \lambda_3$, Laplacian value at CP. [c] $\epsilon = |\lambda_1/\lambda_2| - 1$. [d] λ_1, λ_2, and λ_3 are the Hessian eigenvalues at BCP. λ_3 is along the bond path, and λ_1 and λ_2 are along the direction perpendicular to the bond path. [e] From HF result. [f] From DFT result.

for the metal atom occur in its third quantum shell, and thus are identified with the density of the 3d-orbitals. The pattern of CCs found in the VSCC of the metal atom is a reflection of the uneven populations among five d-orbitals. There are eight lobes of such CCs in the VSCC, located toward the eight triangular faces of the octahedron around the metal center. This geometry can be realized by the linear combination of three t_{2g}-orbitals. Such a feature will give a cubelike domain[59] for the metal (see below in atom domain section).

Bond critical points and the associated properties are given in Table 5. According to these properties, the M−O bond is best described as a closed shell interaction, with $|\lambda_1|/\lambda_3$ much less than 1.0, with $\rho(r_c)$ less than 1.0, and with a positive $\nabla^2\rho(r_c)$ at the BCP, though it was emphasized[60] that this may not be true when the charge distribution is diffused. In this case, we believe that there is some covalent character in the M−O bond, it will be discussed further in the Fermi hole section. On the other hand, for the C_4O_4 ligand, all C−C and C−O bonds are definitely shared interactions, i.e., covalent in character. A large negative $\nabla^2\rho(r_c)$ value and a much greater than 1.0 of $\rho(r_c)$ occur at the BCP. The positive $\nabla^2\rho(r_c)$ of the C−O bond in the MO calculation is rationalized by the electron polarization of such an extremely short bond.[45] The bond ellipticity, ϵ, is a good index for the π-bond character; it is clear that ϵ values of C−C bonds are 0.12−0.25 in experiment, but 0.15 in theory, which is in good agreement with the ϵ value of C−C in benzene (0.23).[45] However, the ϵ values of the C−O bond exhibit a discrepancy between experiment and theory; this is due to the fact that BCP is too close to the C nucleus in theory.[45] The $\rho(r_c)$ value normally correlates well with the bond order; they are 1.8 and 2.6 e Å^{-3}, respectively, for C−C and C−O bonds of squarate, indicating a partial double bond character.

Fermi Hole Function. Bond delocalization is best recognized by the Fermi hole function.[61−63] It was demonstrated[64] that all physical measures of the electron localization or delocalization[65] can be determined by the corresponding localization or delocalization of the Fermi hole density. The Fermi hole density is displayed in Figure 9a−d with the reference electron located

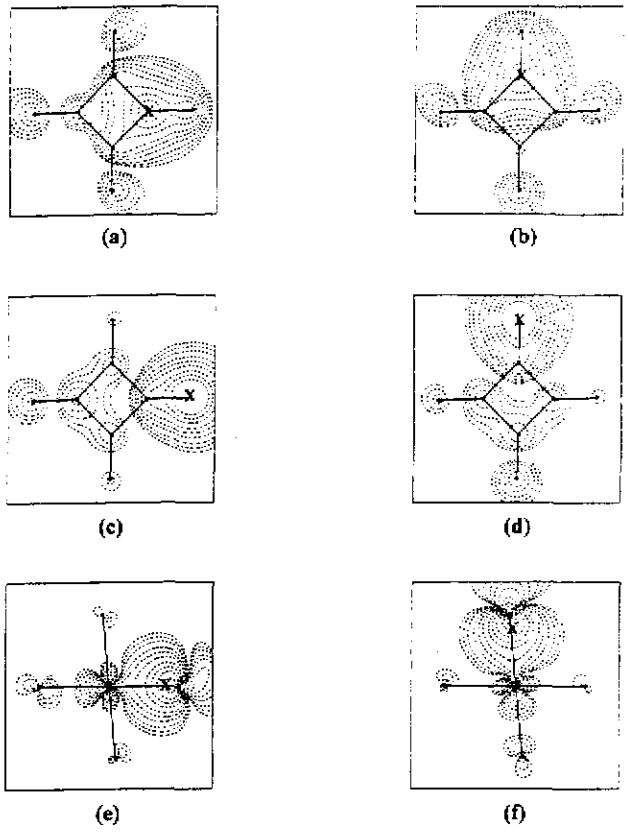

Figure 9. Fermi hole functions from DFT: (a)−(d) at the plane of 0.35 Å above the molecular plane with the reference electron (x) placed on this plane at (a) C1, (b) C2, (c) O1, (d) O2; (e), (f) Fermi hole functions at the molecular plane with reference electron situated at (e) O1 in the O1−Ni−O4 plane and (f) O4 in the O1−Ni−O4 plane.

0.35 Å above the squarate plane at various atomic sites. The density indicates the existence of π delocalization of the squarate ligand; however, the density spread in space is covered over the whole ligand when the reference electron is placed on the

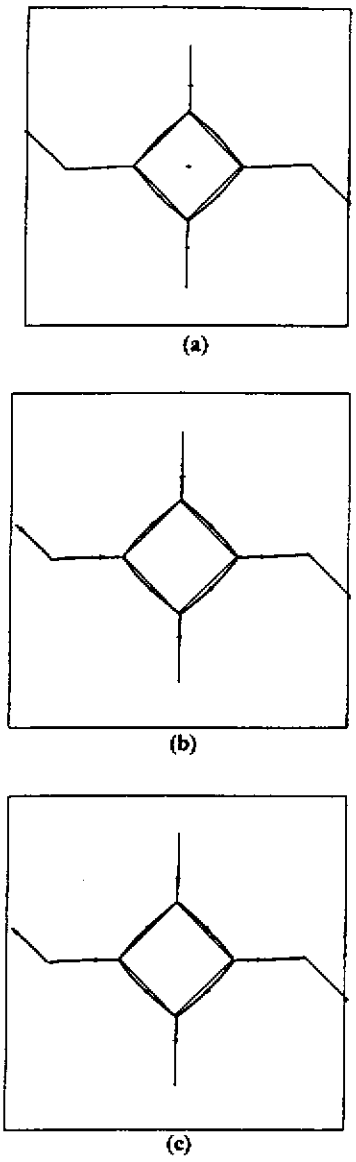

Figure 10. Bond path (with BCP) and interatomic axes of the C_4O_4 plane of the Ni complex from (a) experiment, (b) HF, and (c) DFT.

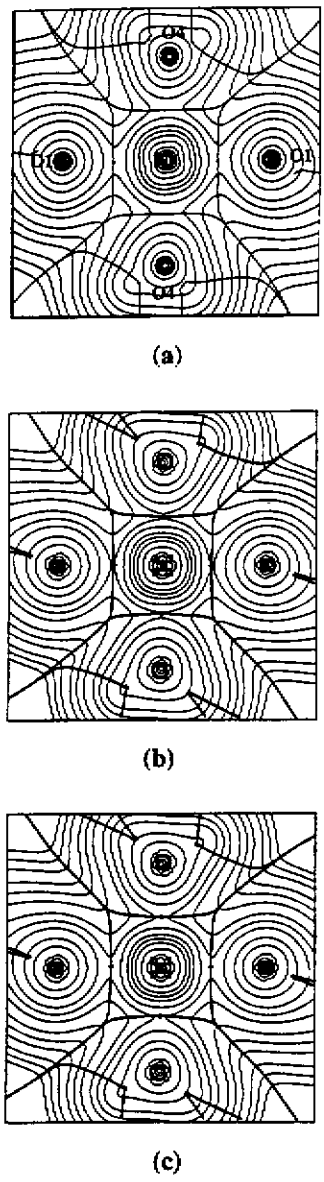

Figure 11. Atom domain and total electron density for the Ni center at the projection of the O1−Ni−O4 plane: (a) experiment; (b) HF; (c) DFT. Contours of electron density are in steps of 2^m10^n e Å^{-3} (m = 1−3; n = −3 to +3).

C atom, while the density spread is only at the C atom and the trans oxygen atom when the reference electron is placed at the oxygen atom. Therefore the delocalization of the p_π-orbital on the ring carbon atoms is more evenly distributed among the C−C bond than that of the C−O bond. These π characters are also consistent with the experimental ϵ values in Table 5.

To probe the M−O σ bond character, a Fermi hole density distribution is plotted in Figure 9e−f with the reference electron located at the lone pair position of oxygen (aq and sq) in the direction of the O−M bond. The distribution clearly indicates the existence of shared character in the $M-O_{sq}$ or $M-O_{aq}$ bond. A similar finding is realized on other transition metal complexes.[46]

Bond Path and Atom Domain. Although the Laplacian of the C_4O_4 plane (Figure 6d−f) does not give so clear an indication of the bent bond as that of deformation density (Figure 5d−f), the C−C bond path does show that the bond path is bent. Figure 10 depicts the bond path together with the interatomic axis (molecular frame) of the C_4O_4 plane from both experiment and theory; the bent feature on the bond path is clearly presented. The atom domain is the partition of molecular electron density into the sum of individual atoms. The atom domain of the metal center in an O_h environment is roughly a cube; one projection is shown in Figure 11 for the Ni complex both from experiment and from theory. The volume of this cube based on the BCP of experiment is 9.3, 9.1, 8.4, and 8.9 Å^3 for Fe, Co, Ni, and Zn, respectively. The smallest one is for Ni, as predicted from ligand field theory.

TABLE 6: d-Orbital Populations of $M(C_4O_4)(H_2O)_4$ (M = Fe, Co, Ni, and Zn)

	Fe	Co	Ni	Ni[a]	Ni[b]	Zn
d_{z^2}	1.09(3)	0.98(4)	0.95(7)	1.09	1.22	1.36(7)
$d_{x^2-y^2}$	1.20(4)	1.11(5)	1.33(8)	1.06	1.15	1.64(8)
d_{xz}	1.43(5)	2.06(6)	2.02(9)	2.01	2.01	1.78(9)
d_{yz}	1.23(4)	1.22(6)	1.71(9)	1.98	2.02	1.55(9)
d_{xy}	1.10(4)	1.51(5)	1.84(8)	2.00	2.01	2.07(8)
total	6.05	6.88	7.89	8.14	8.41	8.40

[a,b] The same as in Table 5.

d-Orbital Populations and Net Atomic Charges. The asphericity in the density distribution around the metal ion can

TABLE 7: Net Atomic Charge of $M(C_4O_4)(H_2O)_4$ (M = Fe, Co, Ni, and Zn)

	Fe	Co	Ni	Ni[a]	Ni[b]	Zn
M	0.28(2)	0.49(5)	0.47(5)	1.66	1.23	1.97(5)
O1	−0.45(2)	−0.39(2)	−0.39(2)	−0.82	−0.60	−0.48(2)
O2	−0.34(2)	−0.30(2)	−0.37(3)	−0.67	−0.51	−0.45(2)
O1′				−0.63	−0.47	
O2′				−0.75	−0.57	
O3	−0.61(2)	−0.53(2)	−0.52(3)	−0.79	−0.67	−0.64(3)
O4	−0.59(2)	−0.55(2)	−0.53(3)	−0.77	−0.66	−0.51(3)
C1	0.10(3)	0.05(3)	0.05(4)	0.44	0.29	−0.13(4)
C2	0.00(3)	−0.09(3)	0.03(4)	0.43	0.27	−0.10(4)
C1′				0.33	0.24	
C2′				0.41	0.26	
H1	0.39(1)	0.37(2)	0.36(2)	0.43	0.36	0.35(2)
H2	0.49(1)	0.40(2)	0.37(2)	0.37	0.34	0.30(2)
H3	0.41(1)	0.38(2)	0.38(2)	0.40	0.37	0.43(2)
H4	0.46(1)	0.41(2)	0.39(2)	0.40	0.37	0.25(2)
H5				0.42	0.37	
C_4O_4	−1.38	−1.45	−1.37	−0.86[c]	−0.72[c]	−2.33
H_2O	0.27, 0.28	0.24, 0.24	0.21, 0.24	0.01, 0.03	0.03, 0.08	0.01, 0.17
$M(H_2O)_4$	1.38	1.45	1.37	1.74	1.46	2.33

[a] [b]The same as in Table 5. [c] The charge of the HC_4O_4 unit.

also be illustrated with the d-orbital populations, which can be derived directly from the multipole coefficients,[66] P_{lmp}. They are listed in Table 6. The populations of d-electrons are 6.05, 6.88, 7.89, and 8.40 for Fe(d^6), Co(d^7), Ni(d^8), and Zn(d^{10}), respectively. In the cases of Fe and Co complexes, they are obviously a high-spin configuration, which are in accord with the magnetic measurement.[67] In all four metal complexes, the populations on e_g-orbitals are, in general, less than those on t_{2g}-orbitals. According to the d-orbital population, the population at d_{z^2} is less than that at $d_{x^2-y^2}$, which is rationalized with a M−O1 bond (z-direction) being 0.04 Å shorter. However, the theoretical calculations in the Ni case give roughly equal population on these two orbitals. Among t_{2g}-orbitals, the population of d_{xz} is significantly higher than the other two for Fe, Co, and Ni complexes; this may well be explained as having some π character in $M-O_{sq}$. A similar statement was mentioned in Tutton salt.[3-5] For the Fe complex, the d-orbital population presented here is in remarkable agreement with those of the Tutton salt both from experiment[5] and from local density approximation (LDA)[9b] calculation. Net atomic charges obtained from the charged spherical model (monopole) of all four complexes are reported in Table 7, together with the ones from MO calculation on the Ni complex. The agreement between experiment and theory on the Ni complex is reasonable. Among the four transition metal ions, Fe, Co, and Ni are nearly neutral and Zn is positive [+(1.97(5)]. The charges of the squarate dianion in Fe, Co, and Ni complexes are roughly "−1"; but in the Zn complex, it is "−2". The difference in the charges of squarate is the reflection of Zn being much more positive than the other metal ions, which has the same trend in the Tutton salt for Cu (+1.8) versus the other metal ions (+0.7 to +1.2).[5] The coordinated H_2O molecule is slightly positive, which is similar to the case of the Tutton salts. Overall, one can probably say that electron transfer is from H_2O to the metal center, and then from the metal ion to the squarate dianion. In the Fe Tutton salt, the charge on OD_2 is slightly positive (0.09), ND_4 is +0.6, and Fe and SO_4 are +0.7 and −2.2, respectively,[5] whereas in the Fe squarate complex, both H_2O and Fe are +0.28 and squarate is −1.38.

Conclusion

Charge density studies on a series of isostructures of 3d-transition metal complexes containing d^6 d^7 d^8 and d^{10} successfully illustrate the consistent deformation density and Laplacian features both on the ligand and at the metal ion. The "bent" bond feature of the four-membered carbon ring is clearly demonstrated both by the deformation density map and by the bond path. The π delocalization on the ligand squarate is demonstrated via the Fermi hole function. The bonding between the metal and oxygen is mainly a σ donor from oxygen lone pairs with covalent character. The total number of d-electrons out of experiment is 6.05, 6.88, 7.89, and 8.40 for Fe, Co, Ni, and Zn, respectively. The asphericity in density near the metal ion is apparent. The agreement between the experiment and theory on the Ni complex is reasonable. The atom domain of the metal ion is 9.3, 9.1, 8.4, and 8.9 $Å^3$ for Fe, Co, Ni, and Zn, respectively.

Acknowledgment. The authors would like to thank the National Science Council of ROC for financial support and NCHC for making the computers and software avaiable. Thanks are due to Professor Bader and Professor Souhassou for their kindly supplying the necessary softwares.

Supporting Information Available: Multipole coefficients, P_{lmp}, of four compounds (Table IS−IVS) are available free of charge via the Internet at http://pubs.acs.org.

References and Notes

(1) Maslen, E. N.; Ridout, S. C.; Watson, K. J. *Acta Crystallogr.* **1988**, *B44*, 96.

(2) Maslen, E. N.; Watson, K. J.; Moore, F. H. *Acta Crystallogr.* **1988**, *B44*, 102.

(3) Figgis, B. N.; Kucharski, E. S.; Reynolds, P. A. *Acta Crystallogr.* **1990**, *B46*, 577.

(4) (a) Figgis, B. N.; Khor, L.; Kucharski, E. S.; Reynolds, P. A. *Acta Crystallogr.* **1992**, *B48*, 144. (b) Figgis, B. N.; Iversen, B. B.; Larsen, F. K.; Reynolds, P. A. *Acta Crystallogr.* **1993**, *B49*, 794.

(5) Figgis, B. N.; Kepert, C. J.; Kucharski, E. S.; Reynolds, P. A. *Acta Crystallogr.* **1992**, *B48*, 753.

(6) Hester, J. R.; Maslen, E. N.; Glazer, A. M.; Stadnicka, K. *Acta Crystallogr.* **1993**, *B49*, 641.

(7) Kellersohn, T.; Delaplane, R. G.; Olovsson, I.; McIntyre, G. J. *Acta Crystallogr.* **1993**, *B49*, 179.

(8) Ptasiewicz-Bak, H.; Olovsson, I.; McIntyre, G. J. *Acta Crystallogr.* **1993**, *B49*, 192.

(9) (a) Chandler, G. S.; Christos, G. A.; Figgis, B. N.; Gribble, D. P.; Reynolds, P. A. *J. Chem. Soc., Faraday Trans.* **1992**, *88*, 1953. (b) Chandler, G. S.; Christos, G. A.; Figgis, B. N.; Reynolds, P. A. *J. Chem. Soc., Faraday Trans.* **1992**, *88*, 1961.

(10) Akesson, R.; Pettersson, L. G. M.; Sandström, M.; Siegbahn, P. E. M.; Wahlgren, U. *J. Phys. Chem.* **1992**, *96*, 10773.
(11) Fender, B. E. F.; Figgis, B. N.; Forsyth, J. B.; Reynolds, P. A.; Stevens, E. *Proc. R. Soc. London* **1986**, *A404*, 127.
(12) Deeth, R. J.; Figgis, B. N.; Forsyth, J. B.; Kucharski, E. S.; Reynolds, P. A. *Proc. R. Soc. London* **1989**, *A421*, 153.
(13) Figgis, B. N.; Forsyth, J. B.; Kucharski, E. S.; Reynolds, P. A.; Tasset, F. *Proc. R. Soc. London* **1990**, *A428*, 113.
(14) Reynolds, P. A.; Figgis, B. N.; Kucharski, E. S. Mason, S. A. *Acta Crystallogr.* **1991**, *B47*, 899.
(15) Hjorth, M.; Norrestam, R.; Johansen, H. *Acta Crystallogr.* **1990**, *B46*, 1.
(16) Kellersohn, T.; Delaplane, R. G.; Olovsson, I. *Acta Crystallogr.* **1994**, *B50*, 316.
(17) Yeh, S. K.; Wu, S. Y.; Lee, C. S.; Wang, Y. *Acta Crystallogr.* **1993**, *B49*, 806.
(18) Wang, C. C.; Wang, Y.; Chou, L. K.; Che, C. M. *J. Phys. Chem.* **1995**, *99*, 13899.
(19) Lee, C. S.; Hwang, T. S.; Wang, Y.; Peng, S. M.; Hwang, C. S. *J. Phys. Chem.* **1996**, *100*, 2934.
(20) Montgomery, H.; Chastain, R. V.; Natt, J. J., Witkowska, A. M.; Lingafelter, E. *C. Acta Crystallogr.* **1967**, *22*, 775.
(21) Montgomery, H.; Chastain, R. V.; Lingafelter, E. C. *Acta Crystallogr.* **1966**, *20*, 731.
(22) Grimes, N. W.; Kay, H. F.; Webb, M. W. *Acta Crystallogr.* **1963**, *16*, 823.
(23) Webb, M. W.; Kay, H. F.; Grimesn, N. W. *Acta Crystallogr.* **1965**, *18*, 740.
(24) Brown, G. M.; Chidambaram, R. *Acta Crystallogr.* **1969**, *B25*, 676.
(25) Montgomery, H.; Lingafelter, E. C. *Acta Crystallogr.* **1964**, *17*, 1295.
(26) Frankenbach, G. M.; Beno, M. A.; Kini, A. M.; Williams, J. M.; Welp, U.; Thompson, J. E.; Whangbo, M.-H. *Inorg. Chim. Acta* **1992**, *192*, 195.
(27) Weiss, A.; Riegler, E.; Alt, I.; Bohme, H.; Robl. Ch. Z. *Naturforsch.* **1986**, *41B*, 18.
(28) Weiss, A.; Riegler, E.; Robl. Ch. Z. *Naturforsch.* **1986**, *41B*, 1333.
(29) Robl. Ch.; Weiss, A. Z. *Naturforsch.* **1986**, *41B*, 1341.
(30) Gerstein, B. C.; Habenschuss, M. *J. Appl. Phys.* **1972**, *43*, 5155.
(31) Yaghi, O. M.; Li, G.; Groy, T. L. *J. Chem. Soc., Dalton Trans.* **1995**, 727.
(32) Lee, C. R.; Wang. C. C.; Wang, Y. *Acta Crystallogr.* **1996**, B52, 966.
(33) Wang, Y.; Stucky, G. D.; Williams, J. M. *J. Chem. Soc., Perkin Trans. 2* **1974**, 35.
(34) Semmingsen, D.; Hollander, F. J.; Koetzle, T. F. *J. Chem. Phys.* **1977**, *66*, 4405.
(35) Semmingsen, D. *Tetrahedron Lett.* **1973**, 807.
(36) Cohen, S.; Lacher, J. R.; Park, J. D. *J. Am. Chem. Soc.* **1959**, *81*, 3480.
(37) Semmingsen, D. *Acta Chem. Scand.* **1973**, *27*, 3961.
(38) Wang, Y.; Stucky, G. D. *J. Chem. Soc., Perkin Trans. 2* **1974**, 925.
(39) Lin, K. J.; Cheng, M. C.; Wang, Y. *J. Phys. Chem.* **1994**, *98*, 11685.
(40) Gutschke, S. O. H.; Molinier, M.; Powell, A. K.; Wood, P. T. *Angew. Chem., Int. Ed. Engl.* **1997**, *36*, 991.
(41) Lin, K. J.; Lii, K. H. *Angew Chem., Int. Ed. Engl.* **1997**, *36*, 2076.
(42) Gabe, E. J.; Le Page, Y.; Charland, J.-P.; Lee, F. L.; White, P. S. *J. Appl. Cryst.* **1989**, *22*, 384.
(43) Hansen, N. K.; Coppens, P. *Acta Crystallogr.* **1978**, *A34*, 909.
(44) Ebsworth, E. A.; Connor, J. A.; Turner, J. J. *Oxygen fluorides*; In *Comprehensive Inorganic Chemistry*; Bailar, J. C., Emeleus, H. J., Nyholm, R. S., Trotman-Dickenson, A. F., Eds.; Pergamon Press: Oxford, U.K., 1973; Vol. 2, Chapter 22, Section 5, pp 747−771.
(45) Bader, R. F. W. *Atom in Molecule—A Quantum Theory*; Clarendon Press: Oxford, U.K., 1990.
(46) Hwang, T. S.; Wang, Y. *J. Phys. Chem.* **1998**, *A102*, 3726.
(47) Rappe, A. K.; Smedley, T. A.; Goddard, W. A., III. *J. Phys. Chem.* **1981**, *85*, 2607.
(48) Wachters, A. J. H. *J. Chem. Phys.* **1970**, *52*, 1033.
(49) Becke, A. D. *J Chem. Phys.* **1993**, *98*, 5648.
(50) Pople, J. A.; Head-Gordon, M.; Fox, D. J.; Raghavachari, K.; Curtiss, L. A. *J. Chem. Phys.* **1989**, *90*, 5622.
(51) Curtiss, L. A.; Jones, C.; Trucks, G. W.; Raghavachari, K.; Pople, J. A. *J. Chem. Phys.* **1990**, *93*, 2537.
(52) Perdew, J. P.; Wang, Y. *Phys. Rev.* **1992**, *B45*, 3244.
(53) Gaussian94, (Revision A. 1); Frisch, M. J., Trucks, G. W., Schlegel, H. B., Gill, P. M. W., Johnson, B. G., Robb, M. A., Cheeseman, J. R., Keith, T. A., Petersson, G. A., Montgomery, J. A., Raghavachari, K., Al-Laham, M. A., Zakrzewski, V. G., Martin, R. L., Ortiz, J. V., Foresman, J. B., Cioslowski, J., Stefanov, B. B., Nanayakkara, A., Challacombe, M., Gomperts, R., Fox, D. J., Binkley, J. S., Defrees, D. J., Baker, J., Stewart, J. P., Head-gordon, M., Conzalez, C., Pople, J. A. Gaussian Inc.: Pittsburgh, PA, 1995.
(54) PROP program: A program developed by M. Souhassou, N. K. Hansen, E. Stevens, B. Craven, N. Bouhmeida, N. Ghermani, and C. Lecomte.
(55) AIMPAC: a set of programs for the Theory of Atom in Molecules; Bader, B. F. W., and co-workers, Eds.; McMaster University: Hamilton, Ontario, Canada, 1994.
(56) Cotton, F. A.; Daniels, L. M.; Murillo, C. A.; Quesada, J. F. *Inorg. Chem.* **1993**, *32*, 4861.
(57) (a) Dewar, M. S. *J. Am. Chem. Soc.* **1984**, *106*, 669. (b) Cremer, D. *Tetrahedron* **1988**, *44*, 7427.
(58) Iversen, B. B.; Larsen, F. K.; Figgis, B. N.; Reynolds, P. A. *J. Chem. Soc., Dalton Trans.* **1997**, 2227.
(59) MacDougall, P. J.; Hall, M. B. *ACA Trans.* **1990**, *26*, 105.
(60) Smith, G. T.; Mallinson, P. R.; Frampton, C. S.; Farrugia, L. J.; Peacock, R. D.; Howard, J. A. K. *J. Am. Chem. Soc.* **1997**, *119*, 5028.
(61) McWeeny, R. *Rev. Mod. Phys.* **1960**, *32*, 335.
(62) Bader, R. F. W.; Stephens, M. E. *Chem. Phys. Lett.* **1974**, *26*, 445.
(63) Bader, R. F. W.; Stephens, M. E. *J. Am. Chem. Soc.* **1975**, *97*, 7391.
(64) Bader, R. F. W.; Johnson, S.; Tang, T.-H.; Popelier, P. L. A. *J. Phys. Chem.* **1996**, *100*, 15398.
(65) Bader, R. F. W.; Streitwieser, A.; Neuhaus, A.; Laidig, K. E.; Speers, P. *J. Am. Chem. Soc.* **1996**, *118*, 4959.
(66) Coppens, P. *Coord. Chem. Rev.* **1985**, *65*, 285.
(67) West, R.; Niu, H. Y. *J. Am. Chem. Soc.* **1963**, *85*, 2589.
(68) Larson, A. C. *Crystallographic Computing*; Copenhagen: Munkasgaard, 1970; p 293.

Structural and Electron Density Studies on a Chromium(IV)-Oxo Complex [Cr^{IV}(O)(TMP)]

Hsiu-Mei Lin (林秀美), Hwo-Shuenn Sheu* (許火順), Chih-Chieh Wang (王志傑), Chi-Ming Che# (支志明) and Yu Wang* (王 瑜)
Department of Chemistry, National Taiwan University, Taipei, Taiwan, R.O.C.

The electron density distribution of a chromium(IV)-oxo complex, [Cr^{IV}(O)(TMP)] (TMP = 5,10,15,20-tetrakis-*p*-methoxyphenyl porphyrin), is investigated by molecular orbital calculation. The molecular and crystal structure of the compound is studied by x-ray diffraction. It belongs to the space group *I* 2, Z = 2, a = 14.979(4) Å, b = 9.752(3), c = 15.605(3) Å, β = 100.97(2)°, V = 2238(1) Å^3, Mo Kα radiation λ = 0.7107 Å, R = 4.9%, Rw = 3.5% for 3575 observed reflections. Cr is five-coordinated in a square pyramidal fashion with the Cr atom located 0.42 Å toward the oxo-ligand. Deformation density maps are derived from the single point molecular orbital calculation on the basis of HF and DFT(density functional theory) calculations. The accumulation of deformation density along the C-H, C-C, C-N and C-O bonds in the porphyrin ligand is well represented. The asphericity in electron density around the Cr ion is clearly demonstrated. Natural bond orbital analysis (NBO) reveals that the Cr-O_{oxo} is actually a triple-bond character ($\sigma^2\pi^4$) and the four N of pyrrole serves as a σ-donor to Cr. The Cr-$N_{pyrrole}$ bond is essentially a dative bond. d-Orbital populations of Cr derived from both calculations are in good agreement with each other. Planar d_π-orbital is the most populated, which is in accord with the prediction from crystal field theory. Detail bond characterization of the Cr-L multiple bond is discussed.

INTRODUCTION

Transition metal complexes with multiple metal-ligand bonds often show a fascinating variety of structures and reactivities and therefore have become a very active field of chemical research.[1] Among the ligands which are capable of forming the metal-ligand multiple bond, oxo ligand have been studied the most and the chemistry of oxo-complexes have been extensively developed.[2,3] Nature also utilizes metal-oxo complexes in a ubiquitous series of important enzymes. Cytochrome P-450 enzyme can catalyze,[4] among other reactions, the epoxidation of alkenes.[5] The reactive intermediates in these chemical reactions, as well as for the enzymatic system, are thought to be high-valent oxo metalloporphyrin complexes such as the oxo-iron(IV) porphyrin π-cation radical,[6] oxo-manganese(IV) porphyrin.[7] Metal-oxo species are also present on the surface of industrially important heterogeneous catalysts.[1] One important and long-standing application of metal oxo derivatives is the oxidant in organic synthesis.[1] The use of oxo derivatives, e.g. K_2CrO_4, $KMnO_4$, RuO_4 and OsO_4, in this regard have been documented.[8] The interest in these compounds arises also from the fact that the oxo and nitrido moieties, in particular, are important building blocks for new electronic materials.[1,9,10] Among such five-coordinated Cr(IV) complexes which have structurally characterized,[1] the coordination geometries at the Cr ion are always between a square pyramid and a trigonal bipyramid. The title complex is in a square pyramidal geometry with an oxygen O atom at the axial position. With the structural analysis and the molecular orbital calculation, it is our hope to clarify the true electronic structure of this high-valent Cr(IV) ion and to characterize the important Cr-O_{oxo} multiple bond in order to understand further its chemical reactivity. Bond characterization of a similar five-coordinated Cr(V) nitrido complex has been reported[11] recently both by accurate x-ray diffraction and by molecular orbital calculation. A comparison of the Cr ligand multiple bond of four chromium complexes will also be made.

EXPERIMENTAL SYNTHESIS

Materials

Dichloromethane and toluene were refluxed over calcium hydride for 3 h prior to distillation. Iodosylbenzene(PHIO) and 5,10,15,20-tetrakis-*p*-methoxyphenyl porphyrin (H_2TMP)[13] were synthesized according to descrip-

*: present address: SRRC, Hsin-Chu, Taiwan
#: present address: Department of Chemistry, The University of Hong Kong, Pokfulam Road, Hong Kong

tion in the literature.[12,13] Cr(TMP)Cl was synthesised and purified as previously described.[13]

Synthesis of Oxo(5,10,15,20-tetrakis-*p*-methoxyphenyl porphyrinaton)chromium(IV) [Cr(O)(TMP)] with Iodosylbenzene[15,16]

Preparation followed the method of Groves:[14] [Cr(TMP)Cl] (140 mg) was added to 10 mL of degassed methylene chloride, followed by iodosylbenzene (150 mg), and the mixture was stirred for 5 min. After addition of 500 mg of KOH powder and 5 min of stirring, the reaction mixture was applied to a dry alumina column. The red fraction was collected and concentrated under vaccum to give a solid. This material was filtered and washed with acetone to remove iodosylbenzene. Recrystallization from methylene chloride/pentane gave a final yield of 25%.

Crystal Structure Determination of [Cr(O)(TMP)]·C_7H_8

Crystals of [Cr(O)(TMP)]·C_7H_8 suitable for single-crystal x-ray diffraction were grown from a toluene solution of [Cr(O)(TMP)] with slow vapor diffusion of hexane. A dark brown crystal (0.2 × 0.3 × 0.4 mm) was mounted on a glass fiber for data collection by using Mo Kα radiation on a CAD4 diffractometer at room temperature. Detailed data collection parameters are given in Table 1. Cell parameters are refined from 24 reflections with the 2θ range 16-37°. Three standard reflections were monitored every two hours throughout the data collection. The variation in intensity is within 3%. Lorentz and Polarization corrections are applied. A semiempirical absorption correction is applied based on azimuthal scans of three reflections. The structure is solved by conventional heavy-atom method, the coordinate of Cr atom is determined from the Patterson function and those of the remaining atoms from subsequent different Fourier syntheses. All the non-hydrogen atoms are refined anisotropically. Hydrogen atoms of porphyrin are refined isotropically and the rest are fixed at positions with C-H distance of 0.96 Å. Structural analyses are performed by using NRCSDP[17] program on an alpha workstation.

Table 1. Crystal Data of CrO(TMP)·toluene

empirical formula	$C_{55}CrH_{41}N_4O_5$
color	dark brown
crystal size	0.20 × 0.30 × 0.40 mm
crystal system	monoclinic
space group	*I* 2
a, Å	14.979(4)
b, Å	9.752(3)
c, Å	15.605(3)
β, °	100.97(2)
V	2238(1) Å^3
Z	2
fw	890
density (calc)	1.32 Mg/m^{-3}
μ	3.0 cm^{-1}
diffractometer	CAD4
radiation	Mo Kα (λ = 0.7107 Å)
temperature	298K
2θ range	2. -50°
scan type	θ - 2θ
h k l range	(-17, 17); (0, 11); (0, 18)
no. of reflns measured	4350
no. of unique reflns	3929
N_o, no. of obsd reflns with $I > 2\sigma(I)$	3575
N_v, no. of parameters refined	307
R	0.049
R_w	0.035
GOF	3.76
$(\Delta/\sigma)_{max}$	0.02
D_{map} min; max	-0.77; 0.72 e/Å^3

$R = \Sigma||F_o|-|F_c||/\Sigma|F_o|$
$R_w = [\Sigma w(|F_o|-|F_c|)^2/\Sigma w|F_o|^2]^{1/2}$
$w = 1/\sigma^2(F_o)$
$GOF = [\Sigma w(|F_o|-|F_c|)^2/(N_o-N_v)]^{1/2}$

Molecular Orbital Calculations

Geometry and Basis Function

The basis set used for Cr atom is (14,9,6)/[8,4,3] contractions, i.e. (626*1/5112/411), where (14s,9p) primitive Gaussian functions are taken from Wachter[18] and (6d) functions are taken from Goddard.[19] The basis sets used for N, O, C and H atoms are taken from split valence double-ζ 3-21G. The basis set used in DFT calculation is a double numerical basis set augmented by polarization function (DNP).[20] Electron correlation is treated within the local density approximation (LDA) in the parameterization of Vosko et al.[21] The local density approximation is applied, where VWN potential is used. The molecular geometry is taken from the diffraction data. In order to reduce the computational time, a C_4, symmetry is assumed and *p*-methoxyphenyl is replaced by hydrogen, so the ligand is porphyrin(por), instead of TMP. The local coordinate at the Cr atom is defined so that z-axis is along the Cr-O_{oxo}, and x,y-axes are at the bisections of ∠N-Cr-N, shown in Fig. 2.

Natural Bond Orbital Analysis

Natural bond orbital analysis[22-25] comprises a sequence of transformations from the given basis sets to various localized sets: natural atomic orbitals (NAOs), natural hybrid orbitals (NHOs),[23] natural bond orbitals(NBOs),[25] and natural localized molecular orbitals (NLMOs).[22,24] The NLMOs can then be transformed to the occupied MOs of HF functions.

given basis sets NAOs → NHOs → NBOs → NLMOs

These procedures derive their names and inspirations from

the natural orbitals of Löwdin,[26] which are obtained from the diagonalization of one particle density matrix. The given basis functions are taken from HF calculation. The results after NBO analysis are generally in good agreement with Lewis structure concepts and the Pauling-Slater-Coulson[27] concept of bond hybridization and polarization. Net atomic charges, orbital populations, and bond orders are thus generated by means of NBO analysis. The charges and orbital populations obtained this way are designed as the natural orbital population analysis (NPA), which is compared with the Mulliken population analysis (MPA).

Theoretical Deformation Density

The theoretical deformation density ($\Delta\rho_{theo}$) is defined as the difference between the total molecular electron density and the promolecular electron density. The total molecular density is calculated either from occupied molecular wave functions at HF level or from DFT. The promolecular electron density is the sum of superposition of the spherical atomic electron density with atoms at the same nuclear positions as in the molecular geometry. The spherical atomic density is calculated at the ROHF/GVB level; each outer valence orbital is assigned to have an equal population of electrons, e.g., 2/3 and 1 for each 2p-orbital (p_x, p_y, p_z) of a carbon and a nitrogen atom, respectively.

All computations were performed on a CONVEX C3840 and Power Challenge computers using the Gaussiam92[28] and DMol programs.[29] The MOPLOT[30] program was used for the deformation density calculation.

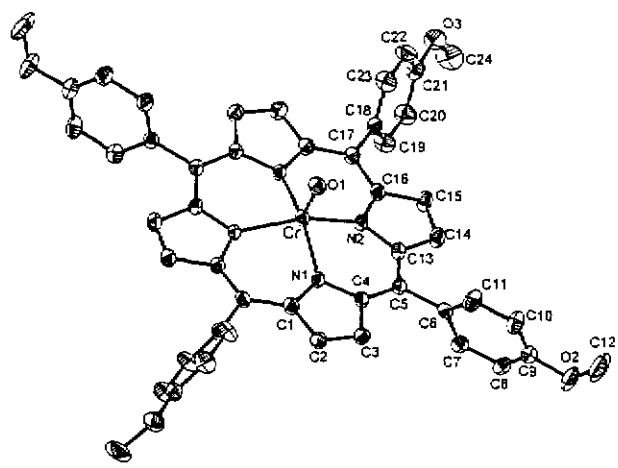

Fig. 1. Molecular structure of Cr(O)(TMP), Thermal ellipsoids are at 50% prohability. Selected bond distances (Å): Cr-O1 1.588(4); Cr-N1 2.025(3); Cr-N2 2.040(3). Angles (°): O1-Cr-N1 103.7(1), O1-Cr-N2 101.0(1); N1-Cr-N2 87.5(1); N1-Cr-N1' 87.3(1).

RESULTS AND DISCUSSION

Structure

The molecular structure and atomic labelling scheme of [Cr(O)TMP] are shown in Fig. 1. All non-hydrogen atomic positions and Beq (Å^2) are given in Table 2, [Cr(O)(TMP)]·C_7H_8 crystallizes in the space group *I* 2 with 2 molecules per unit cell. The molecular symmetry is C_2 with Cr and O1 located at 2-fold axis. The chromium ion is 0.42 Å displaced from the porphyrin plane toward the O ligand. The Cr-$N_{pyrrole}$ distances are 2.025(3) and 2.040(3) Å which are typical values observed for other chromium porphyrins.[15,16] The chromium-oxo bond distance is very short, 1.588(4) Å, implying a chromium-oxo multiple bond character in such a five-coordinated complex. Toluene molecules are packed between the porphyrin molecules; the toluene molecule is also in C_2 symmetry with three C atoms located at 2-fold axis; and the methyl H atoms are in disorder.

Deformation Density

Deformation density maps are depicted in terms of the theoretical map ($\Delta\rho_{HF}$ and $\Delta\rho_{DFT}$). The asphericity in the electron density distribution around the Cr atom is important evidence for assessing the bonding situation of the metal atom. The bond feature between Cr and the porphyrin ligand is displayed in two planes: one at Cr atom parallel to the porphyrin plane, the other at the plane of O-Cr-N. Fig. 3a and Fig. 4a display the deformation densities at a plane parallel to four nitrogen atoms at Cr atom (0.4 Å above the plane). It is quite clear that there is depletion of density along the d_σ-direction and surplus of density along d_π-direction; this is expected in terms of the simple crystal field theory. A large positive deformation density is found near each

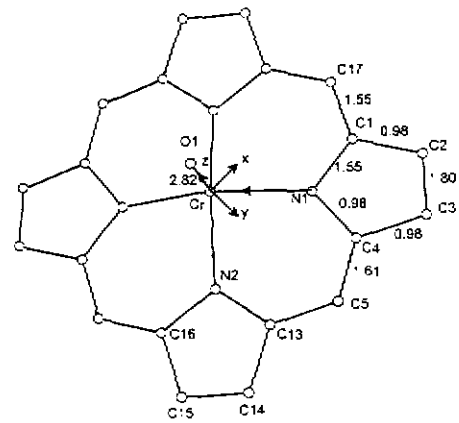

Fig. 2. Bond order and local coordinates of Cr of Cr(O)(por).

Table 2. Fractional Atomic Coordinates and Equivalent Thermal Parameters (Å^2) of Cr(O)(TMP)·toluene, Beq = 8/3 $\pi^2\Sigma_i\Sigma_j U_{ij}a_i^*a_j^*a_{ij}\cdot a_j$

	X	Y	Z	Beq
Cr	0	0.00000	0	3.07(4)
O1	0	-0.1628(4)	0	3.5(2)
N1	-0.0186(2)	0.0493(4)	0.1213(2)	3.0(1)
N2	0.1348(2)	0.0400(4)	0.0425(2)	2.8(2)
C1	-0.1011(3)	0.0544(4)	0.1504(2)	3.1(2)
C2	-0.0851(3)	0.0628(6)	0.2442(2)	3.9(2)
C3	0.0051(3)	0.0630(5)	0.2721(2)	4.1(2)
C4	0.0475(3)	0.0536(5)	0.1970(2)	3.3(2)
C5	0.1410(3)	0.0450(4)	0.2012(2)	3.0(2)
C6	0.2015(3)	0.0392(5)	0.2898(2)	3.1(2)
C7	0.2249(3)	0.1583(5)	0.3394(3)	3.9(2)
C8	0.2830(4)	0.1496(5)	0.4206(3)	4.6(2)
C9	0.3154(3)	0.0244(5)	0.4520(2)	4.0(2)
C10	0.2924(4)	-0.0919(6)	0.4055(3)	5.0(3)
C11	0.2345(3)	-0.0829(5)	0.3234(3)	4.5(2)
O2	0.3721(2)	0.0274(5)	0.5331(2)	6.5(2)
C12	0.4052(4)	-0.1004(8)	0.5711(3)	10.4(5)
C13	0.1809(2)	0.0385(5)	0.1281(2)	3.1(2)
C14	0.2767(3)	0.0370(5)	0.1306(2)	3.6(2)
C15	0.2902(2)	0.0389(5)	0.0478(2)	3.7(2)
C16	0.2023(2)	0.0418(5)	-0.0072(2)	3.3(2)
C17	-0.1868(3)	0.0496(4)	0.0978(2)	3.2(2)
C18	-0.2687(3)	0.0564(5)	0.1409(2)	3.2(2)
C19	-0.3238(3)	-0.0533(5)	0.1427(3)	4.8(2)
C20	-0.4004(3)	-0.0442(5)	0.1807(3)	5.0(2)
C21	-0.4205(3)	0.0758(6)	0.2175(3)	4.2(2)
C22	-0.3650(3)	0.1874(6)	0.2200(3)	4.9(3)
C23	-0.2887(3)	0.1763(5)	0.1804(3)	4.6(2)
O3	-0.4994(2)	0.0734(4)	0.2528(2)	5.2(2)
C24	-0.5170(3)	0.1913(7)	0.3006(3)	7.4(3)
C25	1/2	0.689(2)	0	11(1)
C26	0.5783(7)	0.621(1)	0.0160(5)	9.9(7)
C27	0.5796(4)	0.482(1)	0.0155(4)	7.4(4)
C28	1/2	0.408(1)	0	7.0(6)
C29	1/2	0.249(1)	0	13.4(9)

N atom of porphyrin ligand, this demonstrates the σ-donor character of the porphyrin ligand through the nitrogen atoms. In other words, it is essentially a dative bond from the $N_{pyrrole}$ to Cr. The electron density distribution of Cr-O bond is described in Fig. 3b and Fig. 4b, where a depletion of electron density near Cr along Cr-O is observed. The feature near the O atom is very similar to the feature near the N atom of the nitrido complex[11] in HF calculation.

Net Atomic Charge and d-Orbital Population

Net atomic charges from both calculations are reported in Table 3. The difference in values between various partitions in HF and DFT calculations is detected; however, the sign is consistent. O_{oxo} and $N_{pyrrole}$ are negatively charged, and four neighboring carbon atoms, C1, C4, C13 and C16 are positively charged. The atomic charge of Cr is positive, but by no means near the formal charge of +4. The same is true for O_{oxo}; it is negative, but much less than the expected -2. The porphyrin ligand is roughly -1 with a dominate charge allocated at the N atom, which fits in nicely with the feature shown in the deformation density. The charges obtained via Hirshfeld partition[31] are normally[11,32] much less than those via MPA or NPA partition.

The five-coordinated complex may have been a consequence of the large σ-trans effect[10,33] of the O^{2-} group. The Cr(IV) ion should be in d^2 configuration. d-Orbital populations of Cr can be derived directly from both calculations; they are listed in Table 4. d-Orbitals electrons are distributed such that the in-plane $d_\sigma(d_{xy})$ being the least populated and in-plane $d_\pi(d_{x^2-y^2})$ being the most populated. The d_{xy} or-

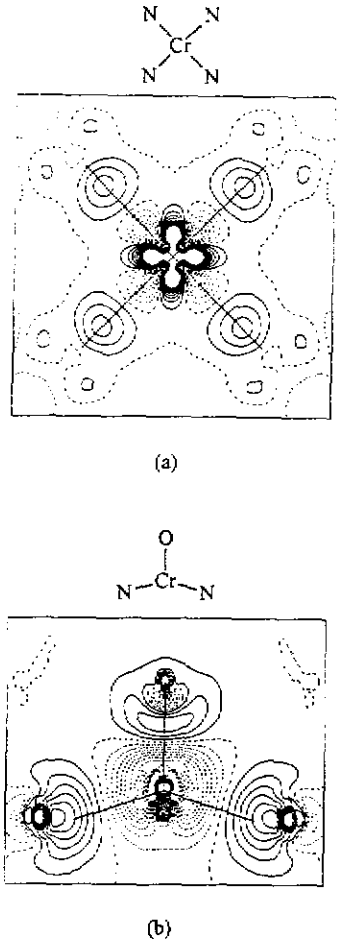

Fig. 3. $\Delta\rho_{HF}$, Deformation electron density obtained from HF calculation (a) plane of porphyrin at Cr atom (b) plane of O-Cr-N. Contour interval is 0.1e Å^{-3} within ± 1e Å^{-3} solid line positive, dotted negative.

bital is at the direction of four Cr-$N_{pyrrole}$ bonds and therefore most destabilized. Though the d_{z^2} orbital is also at the σ-direction of oxo ligand, the trans position is empty, thus the d_{z^2} orbital is not so destabilized as d_{xy} orbital. d_{xz} and d_{yz} Orbitals are degenerate and are responsible for d-p π interaction at the axial direction. According to the d-orbital population, the orbital energies are in the order: $E(d_{x^2-y^2}) < E(d_{z^2}) < E(d_{xz}, d_{yz}) < E(d_{xy})$.

Bond Characterization

After applying the NBO analysis, the hybrid orbitals for each atom are presented in Table 5 together with three other Cr complexes which all contain a Cr-ligand multiple bond. The bond order of each chemical bond of this complex is shown in Fig. 2. The Cr-$N_{pyrrole}$ bond is essentially a dative bond formed by the lone pair electrons at $N_{pyrrole}$ indicated as an arrow in Fig. 2. Bond orders of C-N and C-C bonds in the porphyrin ligand are alternate single, double

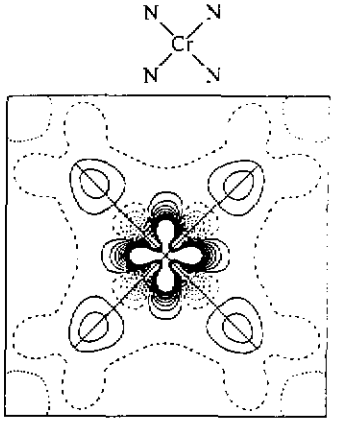

(a)

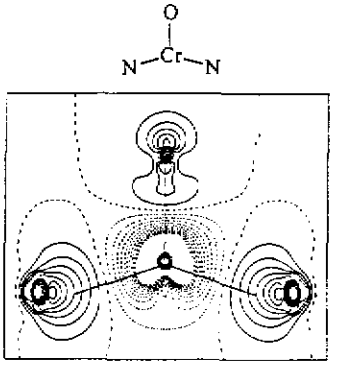

(b)

Fig. 4. $\Delta\rho_{DFT}$. Deformation electron density obtained from DFT calculation. Definitions of (a), (b) and contours are as in Fig. 3.

Table 3. Net Atomic Charges of Cr(O)(Por)

	HF		DFT	
	MPA	NPA	MPA	Hirshfeld
Cr	+1.84	+1.56	+1.23	+0.45
O	- 0.52	- 0.60	- 0.34	- 0.25
N1, N2	- 1.01	- 0.66	- 0.54	- 0.14
C1, C13	+0.37	+0.20	+0.13	+0.04
C2, C14	- 0.25	- 0.24	- 0.24	- 0.07
C3, C15	- 0.25	- 0.24	- 0.24	- 0.07
C4, C16	+0.36	+0.20	+0.14	+0.03
C5, C17	- 0.31	- 0.24	- 0.27	- 0.05
POR	- 1.32	- 0.96	- 0.89	- 0.20

bond as expected to be one of the resonance structures. The Cr-O_{oxo} bond is obviously a triple bond which consists of a σ-bond and two π bonds. The σ bond component is formed from a sd_{z^2} hybrid orbital of Cr and a sp_z hybrid orbital of O_{oxo} with major contribution (~73%) from O_{oxo}. Two π bonds are formed between the (d_{xz}, d_{yz}) orbitals of Cr and the (p_x, p_y) orbitals of O_{oxo} with major contribution (~78%) from O_{oxo}. Similar chromium-ligand (Cr-L) multiple bond of chromium-nitrido,[11] -imido[34] and -carbyne[34,35] are also analyzed by NBO analysis on the basis of calculation at the same level. The Cr-L multiple bond of all four compounds are essentially a triple bond with bond order 2.82, 2.63, 2.57 and 2.56 for Cr-O_{oxo}, Cr-$N_{nitrido}$, Cr-N_{imido} and Cr-$C_{carbyne}$ bond, respectively. The σ bond of Cr-O_{oxo}, Cr-$N_{nitrido}$ and Cr-$C_{carbyne}$ is the same with ~70% contribution from the ligand. In the case of the imido complex, this σ bond is completely contributed from the ligand (100%). However, the π bond character are significantly different: Both π bonds in the oxo-complex are predominately contributed (80%) from the p_π orbitals of oxygen; only 20% are contributed from the d_{xz} or d_{yz} orbital of Cr. In the case of the nitrido complex, both π bonds are formed with equal contribution from p_π orbitals of N and d_{xz}/d_{yz} orbital of Cr. Whereas in the imido case, one π bond is the same as the nitrido complex with

Table 4. d-Orbital Population of Cr Atom in Cr(O)(por)

	HF-SCF		DFT
	MPA	NPA	MPA
$d_{x^2-y^2}$	1.942(49.0%)	1.976(47.6%)	1.952(42.6%)
d_{z^2}	0.759(19.1%)	0.696(16.8%)	0.742(16.2%)
d_{yz}	0.496(12.5%)	0.522(12.6%)	0.639(14.0%)
d_{xz}	0.496(12.5%)	0.522(12.6%)	0.639(14.0%)
d_{xy}	0.272(6.9%)	0.434(10.5%)	0.605(13.2%)
total	3.965	4.150	4.577

Table 5. Comparisons of Atomic Hybrid Orbital and the Bond Occupancies of Cr-O_{oxo}, Cr-$N_{nitrido}$, Cr-N_{imido} and Cr-$C_{carbyne}$ Complexes

	(por)CrO			(bpb)CrN			$(CO)_4$(Cl)CrCPh			(bpb)(Cl)CrNBu^t		
Bond/Bond length (Å)	Cr-$O_{(oxo)}$/1.582(4)			Cr-$N_{(nitrido)}$/1.555(2)			Cr-$C_{(carbyne)}$/1.725(4)			Cr-$N_{(imido)}$/1.63(1)		
Bond Type	Center	NHO	Occ.	Center	NHO	Occ.	Center	NHO	Occ.	Center	NHO	Occ.
σ		sd_{z^2}(27%)	2.00	Cr	sd_{z^2}(30%)	1.79	Cr	sd_{z^2}(30%)	1.96	N	sp_z(100%)	1.68
		sp_z(73%)		N10	sp_z(70%)		C	sp_z(70%)				
π_1	Cr	d_{xz}(22%)	1.99	Cr	d_{xz}(48%)	1.92	Cr	d_{xz}(66%)	1.90	Cr	d_{xz}(49%)	1.91
	O	p_x(78%)		N10	p_x(52%)		O	p_x(34%)		N10	p_x(51%)	
π_2	Cr	d_{yz}(22%)	1.99	Cr	d_{yz}(48%)	1.82	Cr	d_{yz}(72%)	1.88	Cr	d_{yz}(38%)	1.93
	O	p_y(78%)		N10	p_y(52%)		O	p_y(28%)		N10	py(62%)	
				Cr-N1, Cr-$N2_{(amido)}$						Cr-N1, Cr-$N2_{(amido)}$		
σ				Cr	$sd_{xy}d_{z^2}$(5%)	1.65				Cr	$sd_{xy}d_{z^2}$(7%)	1.62
				N1	sp_xp_z(95%)					N1	sp_xp_z(93%)	
	Cr-N1, Cr-$N2_{(pyrrole)}$			Cr-N3, Cr-$N4_{(pyridine)}$			Cr-$C_{(carbonyl)}$			Cr-N3, Cr-$N4_{(pyridine)}$		
n	N	sp_y	1.78	N3	$sp_xp_yp_z$	1.80	C	sp_xp_y	1.62	N3	$sp_xp_yp_z$	1.69

n: lone pair

equal contribution from Cr and N, but the other is formed with 60% from p_π orbital of N and 40% from d_{yz} of Cr. However, in the case of carbyne complex, both π bonds are formed with major contribution (70%) from d_{xz}, d_{yz} orbital of Cr. Based on such bond characterization, we can assume that the orbital energies of p_π orbitals of the axial ligand are as follows:

$$p_\pi(O_{oxo}) < p_\pi(N_{imido}, N_{nitrido}) \cong d_{xz,yz}(Cr) < p_\pi(carbyne)$$

This order is very much in accord with the relative atomic electronegativity.

CONCLUSION

Bond characterization of the metal-O_{oxo} triple bond is assessed from quantum chemical calculation. Density distribution from both HF and DFT calculations dipicts the important feature of bonding. The metal d-orbital populations derived from both calculations are essentially the same; the orbital energy is such that $E(d_{x^2-y^2}) < E(d_{z^2}) < E(d_{xz},d_{yz}) < E(d_{xy})$. The NBO analysis provides a detailed description of hybrid orbitals and bond orders. The triple bond character (σ, 2π) of Cr-O_{oxo} and the dative bonds character of Cr-$N_{pyrrole}$ are well illustrated. The comparison of such triple bond in chromiumm-oxo, nitrido, imido and -carbyne leads to a comprehensive undersatnding of metal ligand multiple bonds.

ACKNOWLEDGEMENT

Financial support of this work from the National Science Council of the R.O.C. is highly appreciated. Thanks are due to the National Center for High Performance Computing for providing computing facilities and software packages.

Received December 29, 1998.

Key Words

Electron density; Cr-O_{oxo} bond; Crystal structure.

REFERENCES

1. Nugent, W. A.; Mayer, J. M. Metal-Ligand Multiple Bonds; Wiley: New York, **1988**.
2. Cundari, T. R.; Gordon, M. S. *J. Am. Chem. Soc.* **1991**, *113*, 5231.
3. Cundari, T. R.; Drago, R. S.; Groves, J. R. *Inorg. Chem.* **1990**, *29*, 2303.
4. Watanabe, Y.; Groves, J. R. The Enzymes; Sigman, D. S., Ed.; Academic Press: San Diego, CA, **1992**; Vol. 20, pp 450-452.
5. Cytochrome p-450; Structure, Mechanism and Biochemistry; Ortiz de Montellano, P. R, Ed.; Plenum: New York, **1986**.

6. (a) Groves, J. R.; Haushalter, R. C.; Nakamura, M.; Nemo, T. E.; Evans, B. J. *J. Am. Chem. Soc.* **1981**, *103*, 2884. (b) Balch, A. L.; Latos-Grazynski, L.; Renner, M. W. *J. Am. Chem. Soc.* **1985**, *107*, 2983. (c) Fujii, H. *J. Am. Chem. Soc.* **1993**, *115*, 4641.
7. (a) Groves, J. T.; Stren, M. K. *J. Am. Chem. Soc.* **1988**, *110*, 8628. (b) Rodger, K. R.; Goff, H. M. *J. Am. Chem. Soc.* **1988**, *110*, 7049.
8. Sharpless, K. B.; Flood, T. C. *J. Am. Chem. Soc.* **1971**, *93*, 2316.
9. Dehnicke, K.; Strahle, J. *Angew. Chem.* **1981**, *93*, 451; *Angew. Chem. Int. Ed. Engl.* **1981**, *20*, 413.
10. Dehnicke, K.; Strahle, J. *Angew. Chem.* **1992**, *104*, 978; *Angew. Chem. Int. Ed. Engl.* **1992**, *31*, 955.
11. Wang, C.-C.; Wang, Y.; Che, C. M.; Chou, L.-K.; Che, C.-M. *J. Phys. Chem.* **1995**, *99*, 13899.
12. Saltzman, H.; Sharefkin, J. G. Organic Syntheses; Baumgarten, H. E., Ed.; Wiley: New York, **1973**; Cillect. Vol. 5; 658.
13. Lindsey, J.; Wagner, R. *J. Org. Chem.* **1989**, *54*, 848.
14. Cheung, S. K.; Grimes, C. J.; Wang, J.; Reed, C. A. *J. Am. Chem. Soc.* **1976**, *98*, 5028.
15. Groves, J. T.; Kruper, W. J.; Haushalter, R. C.; Butler, W. M. *Inorg. Chem.* **1982**, *21*, 1363.
16. Creager, S. E.; Murray, R. *Inorg. Chem.* **1985**, *24*, 3824.
17. Gabe, E. J.; LePage, Y.; Charland, J.-P.; Lee, F. L.; White, P. S. *J. Appl. Crystallogr.* **1989**, *22*, 384.
18. Rappe, A. K.; Smedley, T. A.; Goddard, W. A. III. *J. Phys. Chem.* **1981**, *85*, 2607.
19. Wachter, A. J. H. *J. Chem. Phys.* **1970**, *52*, 1033.
20. (a) von Barth, U.; Hedin, L. *J. Phys. C.* **1972**, *5*, 1629. (b) Vers. ..is, L.; Ziegler, T. *J. Chem. Phys.* **1988**, *88*, 3322.
21. Vosko, S. J.; Wilk, L.; Nusair, M. *Can. J. Phys.* **1980**, *58*, 1200.
22. Reed, A. E.; Weinhold, F. *J. Chem. Phys.* **1985**, *83*, 1736.
23. Foster, J. P.; Weinhold, F. *J. Am. Chem. Soc.* **1980**, *102*, 7211.
24. Reed, A. E.; Weistock, R. B.; Weinhold, F. *J. Chem. Phys.* **1985**, *83*, 735.
25. Reed, A. E.; Curtiss, L. A.; Weinhold, F. *Chem. Rev.* **1988**, *88*, 899.
26. Löwdin, P. O. *Phys. Rev.* **1955**, *97*, 1474-1489.
27. (a) Pauling, L. *J. Am. Chem. Soc.* **1931**, *53*, 1367. (b) Coulson, C. A. Valence, 2nd Ed.; Oxford University Press: London, **1952**.
28. Frisch, M. J.; Trucks, G. W.; Head-Gordon, M.; Foresman, J. B.; Gill, M. W.; Wong, J. B.; Foresman, B. G.; Johnson, H. B.; Schlegel. H. B.; Robb, M. A.; Replogle, E. S.; Gomperts, R.; Andres, J. L.; Raghavachari, K.; Binkley, J. S.; Gonzlez, C.; Martin, R. L.; Defrees, D. J.; Fox, D. J.; Whireside, R. A.; Seeger, R.; Melius, C. F.; Baker, J.; Stewart, J. J. P.; Pople, J. A. Gaussian92, Revision A; Gaussian Inc.: Pittsburgh, PA, **1992**.
29. Delley, B. *J. Chem. Phys.* **1990**, *92*, 508.
30. Lichtenberger, D. L.; Fenske, R. F. MOPLOT. *QCPE* **1975**.
31. Hirshfeld, F. L. *Isr. J. Chem.* **1977**, *16*, 226.
32. Lee, C. S.; Hwang, T. S.; Wang, Y.; Peng S. M.; Hwang, C. S. *J. Phys. Chem.* **1996**, *100*, 2934-2941.
33. Herrmann, W. A. *Angew. Chem. Int. Ed. Engl.* **1986**, *25*, 56.
34. Lin, H. M.; Wang, C. C.; Wang, Y.; Che, C. M. unpublished data.
35. Bire, A. S.; Dao, N. Q.; Fischer, E. O.; Hansen, N. K. *Inorg. Chem.* **1993**, *32*, 5354.

X-ray Absorption Spectroscopic Studies on Light-Induced Excited Spin State Trapping of an Fe(II) Complex

Jey-Jau Lee, Hwo-shuenn Sheu, Chi-Rung Lee, Jin-Ming Chen, Jyh-Fu Lee, Chih-Chieh Wang, Chun-Hsun Huang, and Yu Wang

Contribution from the Department of Chemistry, National Taiwan University, Taipei, Taiwan, R.O.C., and the Synchrotron Radiation Research Center, Hsin Chu, Taiwan, R.O.C.

JOURNAL OF THE AMERICAN CHEMICAL SOCIETY®

Reprinted from
Volume 122, Number 24, Pages 5742–5747

X-ray Absorption Spectroscopic Studies on Light-Induced Excited Spin State Trapping of an Fe(II) Complex

Jey-Jau Lee,[†] Hwo-shuenn Sheu,[‡] Chi-Rung Lee,[†] Jin-Ming Chen,[‡] Jyh-Fu Lee,[‡] Chih-Chieh Wang,[†] Chun-Hsun Huang,[†] and Yu Wang*[,†,‡]

Contribution from the Department of Chemistry, National Taiwan University, Taipei, Taiwan, R.O.C., and the Synchrotron Radiation Research Center, Hsin Chu, Taiwan, R.O.C.

Received December 10, 1999

Abstract: Light-induced excited spin state trapping of $Fe(phen)_2(NCS)_2$ is studied by X-ray absorption spectroscopy using synchrotron radiation. The molecular structure of the excited high-spin state at 17 K is investigated by EXAFS. The relaxation of the light-induced high-spin state at various temperatures is monitored through the absorption spectra. The concurrent abrupt lattice change with the change in electronic configuration is observed through single crystal X-ray diffraction. The lattice cooperative effect is important in the relaxation behavior. The magnetic property and the relaxation behavior of two differently prepared samples are distinctly different.

Introduction

The interesting spin-crossover phenomenon, $^5T_2$, $S = 2$ (high spin, HS) ↔ $^1A_1$, $S = 0$ (low spin, LS) of the molecular complex, $Fe^{II}(phen)_2(NCS)_2$, has been extensively studied over the past 30 years by various techniques. Magnetic susceptibility clearly showed an abrupt spin transition at 176 K[1,2] and the molar heat capacity, C_p, yielded a big peak at 176 K[3] as well. Electronic spectral analysis in the region characteristic of the d−d transition indicated an increase in the ligand field parameter-(10 Dq) of 0.55 eV from a high-spin quintet state to a low-spin singlet state transition.[2] Single-crystal X-ray diffraction measurements at two temperatures (293,130 K)[4,5] showed a decrease in the Fe−N distance of 0.2 and 0.1 Å, respectively, for the $Fe-N_{phen}$ and $Fe-N_{NCS}$ bonds as well as changes in ∠N−Fe−N angles, leading to a more regular octahedral shape at low temperature. Such a contraction of the first coordination shell was also detected in EXAFS analysis.[6] Furthermore, the spin transition of Fe^{II} was carefully monitored by Mössbauer measurements,[7] and the X- ray absorption spectra of the iron K and $L_{II, III}$ edges of this complex show significant modifications during the spin transition.[6,8,9] A shift of 1.44 and 0.5 eV in L_{III} and L_{II} absorption edge toward high energies was detected on going from 300 (HS) to 77 K (LS).[8,9] Recent crystal field multiplet calculations[10] could actually well reproduce the experimental spectra.

Evidence of the light-induced excited spin state trapping (LIESST)[11−14] in this complex was found in Mössbauer spectroscopy[12,13] and in FTIR spectroscopy.[14] The trapping of the metastable HS state was detected at temperatures below 55 K after the sample was irradiated with a xenon lamp and appropriate filter[12] or He/Ne laser.[14]

The K-edge absorption at the near-edge range (XANES) is known to be sensitive to the coordination symmetry and the oxidation state of the target atom. The preedge peak was recently found[15] to be rich in information about the electron density distribution on 3d orbitals. The distinct change in K-edge absorption spectra of $Fe(phen)_2(NCS)_2$ during the spin transition was observed.[8,9] The L-edge absorption spectroscopy is very sensitive to the electronic changes of the target atom, especially the changes involving the modification on the 3d orbital populations such as the spin-crossover phenomenon. Therefore, the soft X-ray absorption spectroscopies (K- and L-edge) are ideal for the study of LIESST in this iron(II) complex. The earlier report of the HS/LS K- and $L_{II,III}$-edge absorption spectra[4,8,9] above and below the transition temperature gives a solid base for this investigation. This work presents the first example of applying the K-, L-edge absorption technique to examine the LIESST phenomenon. Although the K-edge absorption spectrum, is not as sensitive to the variation of 3d orbital population as the L-edge absorption spectrum, it does reflect the changes of the population of the antibonding orbital of Fe−N due to the spin transition of the Fe^{II} ion.

The mechanism of such discontinuous thermal- and light-induced spin transitions of Fe^{II} complexes has drawn wide attention, especially after the Mössbauer technique was intro-

[†] National Taiwan University.
[‡] Synchrotron Radiation Research Center.

(1) König, E.; Madeja, K. *Chem. Commun.* **1966**, *3*, 61.
(2) König, E.; Madeja, K. *Inorg. Chem.* **1967**, *6*, 48.
(3) Sorai, M.; Seki, S. *J. Phys. Chem. Solids* **1974**, *35*, 555.
(4) Gallois, B.; Real, J.-A.; Hauw, C.; Zarembowitch, J. *Inorg. Chem.* **1990**, *29*, 1152.
(5) Real, J.-A.; Gallois, B.; Granier, T.; Franz, S.-P.; Zarembowitch, J. *Inorg. Chem.* **1992**, *31*, 4972.
(6) Cartier, C.; Thuery, P.; Verdaguer, M.; Zarembowitch, J.; Michalowicz, A. *J. Phys. C8*, **1986**, *47*, 563.
(7) Goodwin, H. A. *Coord. Chem. Rev.* **1976**, *18*, 293.
(8) Cartier dit Moulin, C.; Sainctavit, P.; Briois, V. In *Proceedings of the Seventh International Conference on X-Ray Absorption Fine Structure*, Kobe, Japan, 1992. *Jpn. J. Appl. Phys.* **1993**, *32*, 38.
(9) Cartier dit Moulin, C.; Rudolf, P.; Flank, A.-M.; Chen, C. T. *J. Phys. Chem.* **1992**, *96*, 6196.
(10) Briois, V.; Cartier dit Moulin, C.; Sainctavit, P.; Brouder, C.; Flank, A.-M. *J. Am. Chem. Soc.* **1995**, *117*, 1019.
(11) Decurtins, S.; Gütlich, P.; Köhler, C. P.; Spiering, H. *Chem. Phys. Lett.* **1984**, *105*, 1.
(12) Decurtins, S.; Gütlich, P.; Köhler, C. P.; Spiering, H. *J. Chem. Soc., Chem. Commun.* **1985**, 340.
(13) Decurtins, S.; Gütlich, P.; Hasselbach, K. M.; Hauser, A.; Spiering, H. *Inorg. Chem.* **1985**, *24*, 2174.
(14) Herber, R.; Casson, L. M. *Inorg. Chem.* **1986**, *25*, 847.
(15) Westre, T.E.; Kennepohl, P.; DeWitt, J. G.; Hedman, B.; Hodgson, K. O.; Solomon, E. I. *J. Am. Chem. Soc.* **1997**, *119*, 6297.

10.1021/ja9943290 CCC: $19.00
Published on Web 06/01/2000

duced. A couple of excellent reviews[16,17] on this topic give a thorough discussion of all possible models. A pulse laser photolysis study on the relaxation of a polymer-doped high-spin Fe^{II} complex[18] indicates the relevance of a quantum mechanical tunneling mechanism at temperatures below 120 K. The LIESST phenomenon in the crystalline state is believed to be associated with the elastic interactions and lattice cooperativity.[16-19] The lattice defects and lattice anisotropy are also considered[19-21] for such a phenomenon. The HS−LS relaxation kinetics after laser excitation in a series of iron(II) complexes was carefully studied by Hauser et al.,[19,22-26] who proposed a thermally activated relaxation behavior or a nonadiabatic tunneling at elevated temperatures and a nearly temperature independent quantum mechanical tunneling mechanism at low temperatures (<100 K). The intersystem crossings between singlets, triplets, and quintets as well as the reverse-LIESST are well illustrated in the case of $[Fe(ptz)_6](BF_4)_2$.[17,22,27] A study on $[Fe_{0.35}Ni_{0.65}(mtz)_6](ClO_4)_2$ shows that there are two transition states (220, 120 K), each giving very different relaxation behavior.[28] The detailed mechanism for the spin transition and LIESST is still not completely clear and may be worth some more effort; the XAS should be a very useful tool for this purpose.

Experimental Section

The iron complex is prepared according to the literature.[4,29] $L_{II,III}$-edge absorption spectra are measured on the high-energy spherical grating monochromator (HSGM) beam line of SRRC. The spectra are recorded by the total electron yield mode using a microchannel plate (MCP) detector. The schematic experimental setup of the instrument is illustrated in Figure 1. The photon energy is calibrated using 708.5 eV for the peak of L_{III} line of α-Fe_2O_3; the entrance and exit slits are set at 30 × 30 um corresponding to an energy resolution of 0.25 eV at ~700 eV range. XANES and EXAFS spectra are measured on the 1.8T/25 pole wiggler beam line using fluorescence mode with a 6-μm metal mesh made out of Mn. The resolving power of $\Delta E/E$ is up to 1/7000 (operational energy of 1.5 GeV, 100−200 mA). The Si(111) double crystal is employed as the monochromator. The energy calibration is made on the basis of the E_0 of iron foil at 7112 eV. An APD unit is used to control the temperature; the sample is pressed on a In foil to ensure the good thermal conductivity. The pressure of the measuring chamber is at $\sim 10^{-9}$ and 10^{-3} Torr for L-edge and K-edge absorption, respectively.

Light-induced excitation is undertaken by a He/Ne laser or a Xe arc lamp with the proper filter. The excitation normally takes place in a few minutes. The light is then turned off before making the scan of the spectra.

The EXAFS oscillation function $k^3\chi(k)$ was obtained by a standard analysis procedure[30,31] using the UWXAFS code (including AUTOBK,[32-34] ATOMS,[35] FEEE,[36,37] and FEFFIT[32,38] programs): preedge baseline and postedge background subtractions are applied by a linear and by a spline function, respectively. The analysis of the first coordination shell of iron ($Fe-N_6$) is regarded as a single scattering path, and only the first shell contribution is considered in this work. The iron atom is at the C_2 symmetry site, and the starting point of Fe−N bond lengths is based on the single-crystal diffraction (XRD) data at room temperature[29] and at 20 K for HS-1 and LS-1, respectively.

Single-crystal diffraction data at 20 K is taken at the X3A1 beam line of NSLS at BNL, using a wavelength of 0.642 Å. A total of 7433 reflections are collected on IP. Intensity integration and scale are based on the DENZO and the SCALE programs of the HKL package;[39] for the data analyses and structure solution the NRCSDP program are used.[40]

FTIR spectra are taken on a Bomem spectrometer using KBr tablets; the sample temperature is controlled by an APD unit. The magnetic measurement is made on a SQUID magnetometer in the temperature range of 5−300 K.

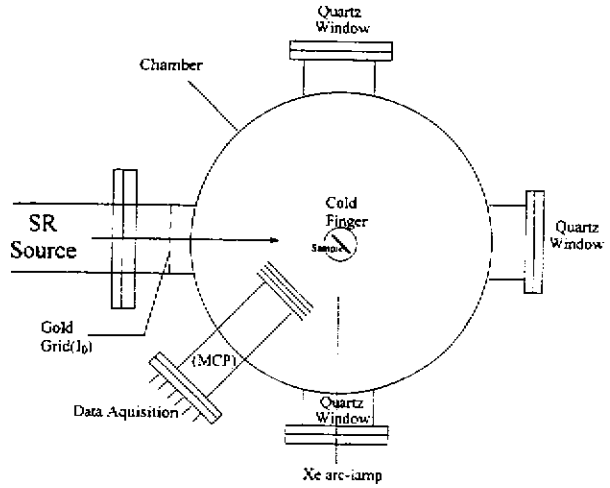

Figure 1. Schematic drawing of the experimental setup for L-edge absorption.

Results and Discussion

Thermally Induced Spin Transition. Variation of the magnetic moments, μ_{eff}, with temperature for the iron compound is shown in Figure 2, which reconfirms the abrupt spin crossover at 176 K. Figure 2 also confirms the previously observed[41] clear difference between the two samples prepared by high-temperature extraction[41,4] and by diffusion.[29] The extraction sample undergoes a complete spin transition from $^5T_2$ to $^1A_1$, while the diffusion sample displays some residual magnetic moment (~1.8 μ_B.) at temperatures below 176 K. However, the single crystal can only be obtained by the diffusion method. The spin-crossover phenomenon is not accompanied by a crystal structural phase change in this case. Both HS and LS state molecules are crystallized in the same space group, *Pbcn*; however, the lattice

(16) Gütlich, P.; Hauser, A.; Spiering, H. *Angew Chem., Int. Ed. Engl.* **1994**, *33*, 2024−2054.
(17) Gütlich, P.; Hauser, A. *Coord. Chem. Rev.* **1990**, *97*, 1.
(18) Xie, C.-L.; Hendrickson, D. N. *J. Am. Chem. Soc.* **1987**, *109*, 6981.
(19) Hauser, A.; Gütlich, P.; Spiering, H. *Inorg. Chem.* **1986**, *25*, 4245.
(20) Spiering, H.; Willenbacher, N. *J. Phys: Condens. Matter* **1989**, *1*, 10089.
(21) Granier, T.; Gallois, B.; Gaultier, J.; Real, J.-A.; Zarembowitch, J. *Inorg. Chem.* **1993**, *32*, 5305.
(22) Hauser, A. *Coord. Chem. Rev.* **1991**, *111*, 275.
(23) Hauser, A.; Vef, A.; Adler, P. *J. Chem. Phys.* **1991**, *95*, 8710.
(24) Hauser, A. *J. Chem. Phys.* **1991**, *94*, 2741.
(25) Hauser, A. *Chem. Phys. Lett.* **1992**, *192*, 65.
(26) Hauser, A.; Adler, J.; Gütlich, P. *Chem. Phys. Lett.* **1988**, *152*, 468.
(27) Hauser, A. *Chem. Phys. Lett.* **1986**, *124*, 543.
(28) Buchen, T.; Schollmeyer, D.; Gütlich, P. *Inorg. Chem.* **1996**, *35*, 155.
(29) Schilt, A. A.; Fritsch, K. *J. Inorg. Nucl. Chem.* **1966**, *28*, 2677.
(30) Sayers, D. E.; Bunker, B. *A. X-Ray Absorption: Principles, Applications, Techniques of EXAFS, SEXAFS and XANES*; Koningsberger, D. C., Prins, R., Eds.; John Wiley & Sons: NewYork, 1988; p 211.
(31) Asakura, A. *X-Ray Absorption Fine Structure for Catalysts and Surface*; Iwasawa, Y., Ed.; World Scientific: Singapore, 1996; p 34.
(32) Newville, M. Ph.D. Thesis, 1997.
(33) Newville, M.; Livins, P.; Yacoby, Y.; Rehr, J. J.; Stern, E. A. *Phys. Rev. B* **1993**, *47*, 14126.
(34) Newville, M. AUTOBK document, 1995.
(35) Ravel, B. ATOMS document, 1995.
(36) Zabinsky, S. I.; Rehr, J. J.; Ankudinov, A.; Albers, R. C.; Eller, M. *J. Phys. Rev. B* **1995**, *52*, 2995.
(37) Ankudinov, A. FEFF601 document, 1995.
(38) Newville, N. FEFFIT document, 1996.
(39) Otwinowsky, Z.; Minor, W. *Methods Enzymol.* **1997**, *276*, 307.
(40) Gabe, E. J.; Le Page, Y.; Charland, J.-P.; Lee, F. L.; White, P. S. *J. Appl. Crystallogr.* **1989**, *22*, 384.
(41) Ganguli, P.; Gütlich, P.; Müller, E. W. *J. Chem. Soc., Dalton Trans.* **1981**, 441.

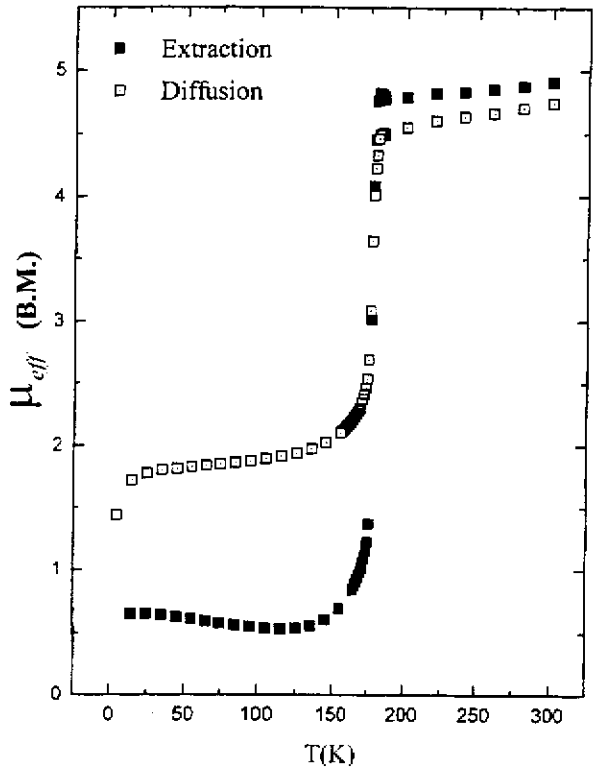

Figure 2. Temperature-dependent effective magnetic moment (μ_{eff}) measurement of $Fe(phen)_2(NCS)_2$ prepared by extraction (■) and diffusion (□)methods.

Table 1. Lattice Parameters and Fe−N Distances of the HS-1, LS-1, and HS-2 States Based on Single-Crystal Diffraction Data (XRD) and EXAFS Data

P bcn	HS-1 (300 K)		HS-2	LS-1 (20 K)	
lattice param (Å)					
a	13.146(2)			12.510(2)	
b	10.129(4)			9.959(3)	
c	17.453(6)			16.949(5)	
	XRD	EXAFS	EXAFS	XRD	EXAFS
T (*K*)	300	300	17	20	17
$Fe-N_{(phen)}$ (Å)	2.214(8)	2.190(5)	2.12(1)	1.967(3)	1.985(5)
$Fe-N_{(phen)}$ (Å)	2.194(8)	2.132(5)	2.06(1)	1.962(2)	1.979(5)
$Fe-N_{(NCS)}$ (Å)	2.070(9)	2.115(5)	2.04(1)	1.925(3)	1.943(5)

contracts anisotropically and the Fe−N bond shortens significantly from the HS to the LS state. The results are listed in Table 1. To investigate the change in structure near the transition temperature, a diffraction pattern out of a certain orientation is monitored through an image plate detector. A selected group of reflections out of one frame at various temperatures near 176 K is carefully studied; the observation of the drastic change in *d* spacing within a few kelvin implies that even the lattice change (diffraction pattern) during the spin transition is as abrupt as the change in magnetic moment. The lattice parameters determinated in the temperature range of 140−190 K based on the refinement of 150 reflections out of this frame indicate that the abrupt change in pattern is due mainly to the change in "a" dimension, which can be manifested by the distinct shift in diffraction position of high "h" reflections. The thermally induced spin transitions of both the extraction and the diffusion samples are reconfirmed by FTIR and K- and L- edge X-ray absorption spectra. The results for the extraction samples are shown in Figures 3a, 4a, and 5a, respectively. The ones from the diffusion sample are basically the same as those for the extraction sample, except in the case of the LS state of FTIR,

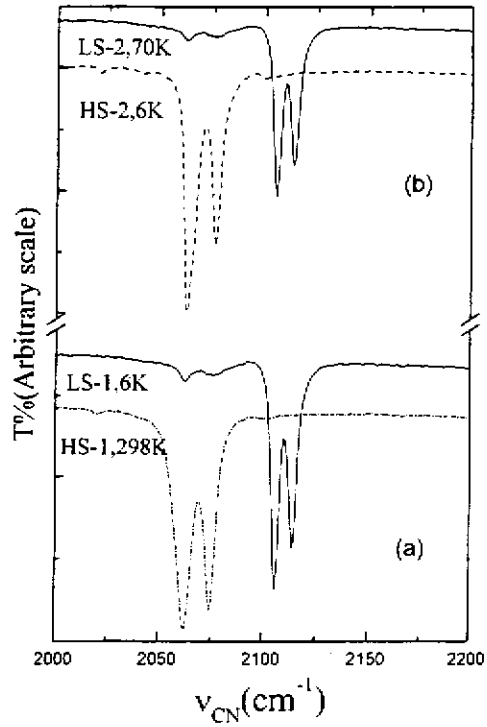

Figure 3. C−N streching frequency, ν_{C-N}, of (a) HS-1/LS-1 and (b) HS-2/LS-2 for the extraction sample.

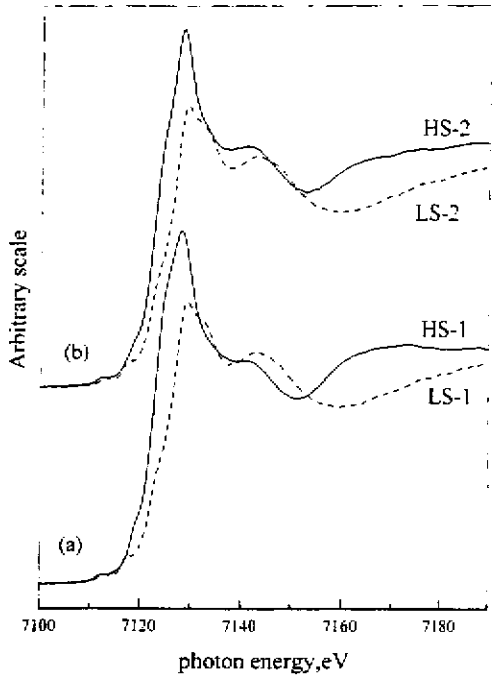

Figure 4. XANES spectra of (a) HS-1/LS-1 and (b) HS-2/LS-2 for the extraction sample.

where a small residual peaks of the HS state is observed. This is consistent with the magnetic measurement.

LIESST and Electronic Configuration of HS-2. LIESST in this Fe^{II} complex is investigated by FTIR at 6 K using a 5 mW He/Ne laser. The sample pressed in a KBr tablet is exposed to the light source for only a few minutes before complete excitation from the LS to the HS state has taken place. To differentiate this light-induced excited HS state from the thermally induced HS state, we designate the light-induced one HS-2 and the thermally induced one HS-1 after the convention in the literature.[14] This HS-2 state in the solid is stable for at

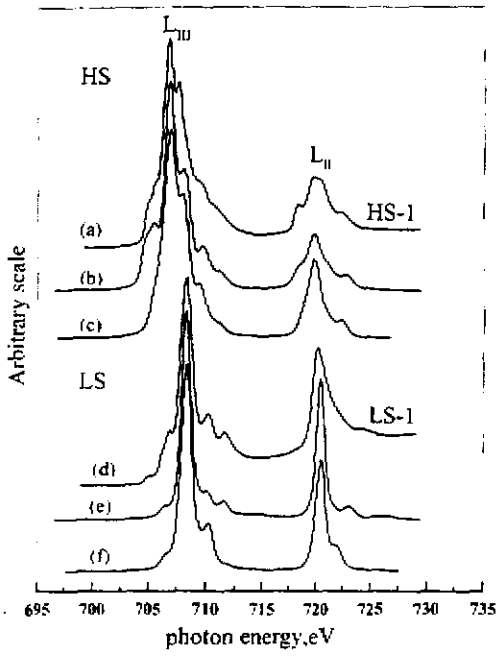

Figure 7. Experimental and calculated Fe $L_{II,III}$-edge absorption: measured spectra at (a) 298 and (d)17 K; (b, e) calculated spectra including MLCT; (c, f) calculated spectra without MLCT.

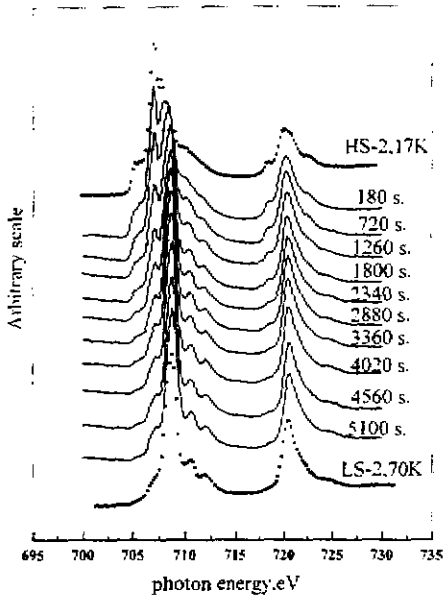

Figure 8. Thermal relaxation of HS-2 at 57 K based on the L-edge absorption spectra. Typical spectra of HS-2 at 17 K and of LS-2 at 70 K are included as dotted curves.

L-edge absorption spectra. There are two diagrams in Figure 9, for the extraction sample (a) and for the diffusion sample (b). It is quite clear that the relaxation rate of the diffusion sample is significantly faster than that of the extraction sample at the same temperature. For example, at 55 K, it takes ~42 min to be half-relaxed ($\gamma_{HS} = 0.5$) for the extraction sample, but only ~20 min for the diffusion sample. Similar observations are also obtained with K-edge absorption spectra. These observations of the differences in relaxation behavior and in the magnetic measurement from two differently prepared samples is in accord with the theory of elasticity, where the HS or LS molecules are considered to be defects in the crystal lattice.[24] Thus, the quality of the crystalline material does play a role in the relaxation process. These relaxation curves are sigmoidal, which means

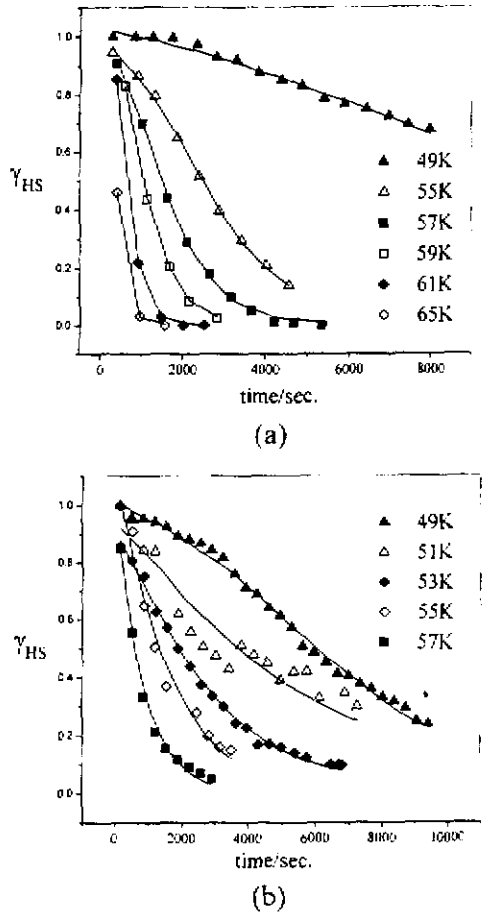

Figure 9. HS → LS relaxation curves at various temperatures based on the L-edge absorption spectra after irradiation on (a) the extraction sample and (b) the diffusion sample. Solid lines are from eq 2.

the relaxation behavior for the complex is not that of an isolated molecule; some cooperative interactions must be included. The model was established for a pure, nondoped $[Fe(ptz)_6](BF_4)_2$ spin-crossover complex.[25] It has been shown that the acceleration in relaxation is due to the buildup of an internal pressure ("lattice pressure") with increasing LS fraction, γ_{LS}. Hauser[25] showed that the relaxation rate is a function of this lattice pressure and thus is a function of the LS fraction, γ_{LS}. The relaxation curve can be fitted according to the following equations,[22,24-27,43]

$$d\gamma_{LS}/dt = k_{HL}(\gamma_{LS},T)(1 - \gamma_{LS}) \quad (1)$$

$$k_{HL}(\gamma_{LS},T) = k_{HL}(T)\exp[\alpha(T)\gamma_{LS}] \quad (2)$$

$$k_{HL}(T) = a_{HL}\exp(-E_a/k_BT) \quad (3)$$

where $k_{HL}(\gamma_{LS},T)$ is a rate constant for HS → LS conversion, which is not only a function of temperature, T, but also a function of the LS fraction, γ_{LS}. $k_{HL}(\gamma_{LS},T)$ represents a self-acceleration of HS → LS relaxation with increasing γ_{LS} (cooperative effect) as indicated in eq 2, E_a is the activation energy associated with the HS → LS relaxation, and a_{HL} is the preexponential factor. In the temperature range studied, the relaxation behavior can be analyzed using eqs 1 and 2. The fitting parameters based on the Fe L-edge absorption experiment are summarized in Table 2. The fitted curves are shown in

(43) Létard, J.-F.; Guionneau, P.; Rabardel, L.; Howard, J. A. K.; Goeta, A. E.; Chasseau, D.; Kahn, O. *Inorg. Chem.* **1998**, *37*, 4432.

Table 2. Kinetics Relaxation Model Fitting Parameters from L-Edge Measurements for (a) Extraction and (b) Diffusion Sample

T (K)	$k_{HL}(T)$	$1/T$	$\ln k_{HL}(T)$	$\alpha(T)$
	(a) Extraction Sample			
49	3.38×10^{-5}	0.020 41	−10.30	1.53
55	1.47×10^{-4}	0.018 18	−8.83	1.27
57	2.72×10^{-4}	0.017 54	−8.21	1.14
59	5.50×10^{-4}	0.016 95	−7.51	0.86
61	6.00×10^{-4}	0.016 39	−7.42	1.40
65	9.87×10^{-4}	0.015 38	−6.92	1.34
	(b) Diffusion Sample			
49	6.16×10^{-5}	0.020 41	−9.69	1.26
51	1.31×10^{-4}	0.019 61	−8.94	0.50
53	2.68×10^{-4}	0.018 87	−8.23	0.35
55	5.65×10^{-4}	0.018 18	−7.48	0.15
57	1.62×10^{-3}	0.017 54	−6.42	−0.30

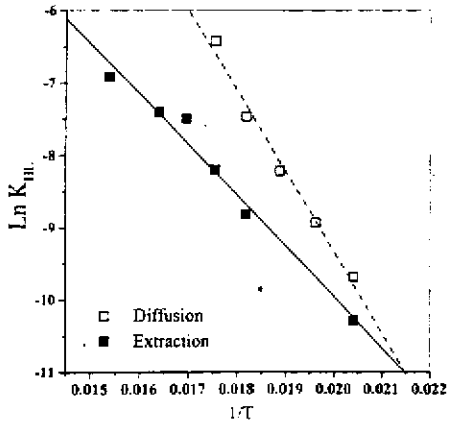

Figure 10. Arrhenius plot of the HS → LS relaxation.

Figure 9 as solid lines. Thus, the data of this complex can be understood in terms of a γ_{LS}-dependent, self-acceleration process.

According to the theory of nonadiabatic multiphonon relaxation, the temperature independent tunneling rate constant, k^0_{HL}, is a function of the Huang−Rhys factor S and the reduced energy gap p. S is related to the equilibrium internuclear displacement ΔQ of the HS and LS states,

$$S = \frac{1}{2}\frac{\Delta Q^2}{\hbar\omega} \qquad \text{where} \qquad \Delta Q = \sqrt{6}\Delta r_{HL} \qquad (4)$$

p is related to the energy gap, ΔE^0_{HL},between the lowest vibronic levels of the HS and the LS states according to

$$p = \Delta E^0_{HL}/\hbar\omega \qquad (5)$$

where ω is the frequency of the breathing vibration of the FeN_6 core, Δr_{HL} is the difference in Fe−N bond length between the HS state and the LS state, and f is the force constant of the Fe−N bond.

Two curves of $\ln K_{HL}$ vs T^{-1} are shown in Figure 10 for the extraction and the diffusion samples, respectively. Both represent linear progression in the temperature range studied (49−65 K). From these linear plots, one can obtain thermal activation energies, E_a, of 487 ± 34 and 773 ± 52 cm^{-1} and the preexponential factor a_{HL} of 5.74×10^1 and 3.88×10^5 for the extraction and diffusion samples, respectively. It is obvious that the relaxation rate K_{HL} is primarily controlled by a_{HL} in the temperature range studied. Thus K_{HL} is larger for the diffusion sample than for the extraction sample.

Assuming that, at temperatures below 50 K, the relaxation behavior is temperature independent, then one gets an S value of ~45 cm^{-1} and p value of 1−2,[22,24−27] Thus, the zero point energy difference of the HS and the LS states, ΔE^0_{HL}, is 250−500 cm^{-1}. The observed low-temperature tunneling rate, K^0_{HL} (at $T \rightarrow 0$), is $\sim 10^{-10}$, when plotted against the transition temperature (176 K), which agreees with the literature values for such spin-crossover systems.[16,22] Unfortunately we cannot afford the lengthy beam time required for study of the relaxation behavior at very low temperature (<49 K). Neverthless, comparing our work with the relaxation behavior of other spin-crossover systems,[16,22] we believe that the relaxation mechanism does have a temperature-dependent part at somewhat elevated temperatures and a temperature-independent tunneling part at temperatures below 50 K.

Conclusion

Metal K- and L-edge absorption spectroscopy appears to be a very powerful technique to investigate the spin-crossover system. The abrupt change in diffraction pattern near the transition temperature is firmly observed. LIESST and the relaxation behavior are successfully monitored by X-ray absorption spectroscopy. The model of a self-acceleration of HS to LS relaxation with increasing fraction of LS species is consistent with the experimental observations. The molecular structure of the excited high-spin state (HS-2) at low temperature is believed to be slightly different from that of the normal high-spin state (HS-1). Two differently prepared samples give the same FTIR and XAS spectra, but show significantly different behavior in magnetic measurement and the thermal relaxation behavior of the HS-2 state.

Acknowledgment. We give special thanks to Prof. Y. P. Lee and Miss L. H. Lai of National Tsing-Hwa University for their assistance with the VTFTIR measurement. Thanks are due to Dr. de Groot for supplying the software on crystal field multiplet calculation and to Dr. Otwinowsky, for supplying and kindly helping with the HKL packages. We also o express our thanks to the instrumentation center at National Taiwan University for magnetic measurement and the X3A1 beam line staff for their assistance with the XRD measurement. Financial support from NSC and SRRC are highly appreciated.

Supporting Information Available: HS → LS relaxation curves at various temperatures based on the Fe K-edge absorption spectra after irradiation on extraction sample and diffusion sample; tables of crystal data, structure solution and refinement, atomic coordinates, and anisotropic thermal parameters for Fe(phen)$_2$(NCS)$_2$ at 20 K; an Ortep drawing of Fe(phen)$_2$(NCS)$_2$ at 20 K; and Fourier-filtered EXAFS data for the first coordinated shell for HS-1, LS-1, andHS-2. See any current masthead page for ordering information and Web access instructions.

JA9943290